1985

Analytical electron microscopy studies in the yttrium oxide lanthanum oxide (Yb2sOb3s-Lab2sOb3s) system /

Stephen Francis Horvath
Lehigh University

ANALYTICAL ELECTRON MICROSCOPY STUDIES IN THE YTTRIUM OXIDE-LANTHANUM OXIDE (Y_2O_3-La_2O_3) SYSTEM

by

Stephen Francis Horvath

A Thesis

Presented to the Graduate Committee

of Lehigh University

in Candidacy for the Degree of

Master of Science

in

Metallurgy and Materials Engineering

Lehigh University

1985

CERTIFICATE OF APPROVAL

This thesis is accepted and approved in partial fulfillment of the requirements for the degree of Master of Science.

Sept. 25, 1985

(Date)

Martin P. Harvilet

Professor in Charge

David A. Thomas

Department Chairperson

ACKNOWLEDGEMENTS

I would like to thank all who have contributed their help and/or time in some form or another to my graduate study at Lehigh these past two years. In particular, I would like to thank my thesis advisor, Dr. Martin P. Harmer and also Drs. Michael R. Notis and David B. Williams for their guidance and encouragement provided during the course of this work. Thanks are also extended to Dr. W. H. Rhodes of GTE Laboratories for supplying many of the samples used in this study as well as for helpful discussions concerning this system, Dr. G. C. Wei for his useful contributions concerning the electron microscopy of this system, and Dr. Helen Chan for her patience and help in answering my many questions concerning events occurring in the microscope.

I would also like to acknowledge Dave Calvert and Jim Kerner for their help with the use of the analytical electron microscopy equipment, Steve Bennison for his help with the laboratory equipment setup as well as the many enlightening discussions on ceramics in general, Betty Zdinak for her patience in typing this manuscript, my fellow graduate students and in particular, Janis Kowalik.

Finally, thanks are extended to my Mom and Dad, my sister Jeanne, and brother Mike for their constant support and encouragement.

The support of the Department of Energy and the Metallurgy and Materials Engineering Department is also gratefully acknowledged.

TABLE OF CONTENTS

LIST OF FIGURES

LIST OF TABLES

ABSTRACT

The primary focus of this work concerns the investigation of the hexagonal phase precipitation phenomenon in the cubic matrix at high temperatures in the Y_2O_3-La_2O_3 system by analytical electron microscopy techniques. Sintered 9 mol% La_2O_3/Y_2O_3 samples upquenched from the single phase cubic region into the two phase cubic and hexagonal field were held at two different temperatures in this region for times ranging from one to three hundred minutes before being quenched to room temperature.

Intergranular precipitation predominates in samples annealed at 2100°C just inside the two phase field as small La_2O_3 rich second phases form on the boundaries within the first ten minutes and develop into strained, facetted precipitates with twinned substructures after 300 minutes. Intergranular and intragranular precipitation occurs for annealing temperatures further into the two phase field (2200°C) the dominant morphology for long times at temperature being strained, lath-like, La_2O_3 rich, twinned precipitates exhibiting a preferred orientation in the matrix.

Chemical microanalysis of the strained structures obtained after 300 minutes reveals La_2O_3 matrix concentrations in agreement with phase diagram predictions, while second phase La_2O_3 concentrations exceed the cubic/cubic and hexagonal solvus. Either the phase diagram is in error, or the strained nature of the second phase induced by coherency effects subjects the system to a state of coherent equilibrium, in which case the phase rule governing the two coexisting phases becomes invalid.

X-ray powder diffraction results from 30 mol% La_2O_3 samples quenched from the single phase hexagonal field revealed retention of the hexagonal phase. However, selected area diffraction studies on banded regions and areas exhibiting dislocations yield patterns of monoclinic symmetry. The bands may either be twins resulting from the hexagonal to monoclinic displacive transformation or alternate bands of the monoclinic structure which form epitaxially within the hexagonal phase. Composition invariance across the bands lends credence to the displacive nature of the transition. Finally, a brief demonstration of the fluorescence phenomenon in laser Raman spectroscopy is included to indicate the potential problems involved in analyzing rare earth oxides by this light scattering technique.

INTRODUCTION

Current investigations on yttrium oxide, the most abundant rare earth oxide have been focusing on the unique optical properties of this ceramic.[1-3] Y_2O_3 exhibits great potential as an optical material due to its isotropic (cubic) structure, chemical stability and excellent light transmittance capabilities which extend further into the infrared region than most other oxides.[4] The relative ease of fabricating Y_2O_3 makes it competitive with other infrared materials presently being used such as MgO and Al_2O_3 and may justify its use in such applications as lamp envelopes for high pressure sodium arc lamps, windows and nosecones for infrared heat seeking missiles and other infrared devices, as well as various laser system utilizations.

Over the years, sintering methods have been developed to yield highly dense, highly transparent yttrium oxide. Recently, Rhodes and coworkers[5] have developed a transient second phase sintering technique based upon the Y_2O_3-La_2O_3 binary that results in transparent, stochiometric polycrystalline Y_2O_3 solid solution material without the toxicity problems previously encountered with BeO solute additions or the chemical instability observed in ThO_2-Y_2O_3 ceramics.[6] The technique consists of sintering Y_2O_3 doped with 8-14 mol% La_2O_3 in the two phase cubic and hexagonal field region very close to the cubic/cubic and hexagonal solvus. The hexagonal phase precipitates which heterogeneously nucleate on the grain boundaries pin their motion, preventing pore-boundary breakaway and thus help facilitate pore annihilation by diffusion along the boundary. A lower temperature anneal in the single phase cubic region dissolves the second

phase, yielding a fully dense, highly transparent, homogeneous polycrystalline Y_2O_3 ceramic.

Though the unique features of the Y_2O_3/La_2O_3 phase diagram have been successfully utilized in the fabrication of dense polycrystalline Y_2O_3, recent interest has developed over the nature of the phase transition involved in the sintering technique and in the Y_2O_3-rich portion of the binary system in general. Preliminary investigations by GTE[1,2] on 8-14 mol% La_2O_3 samples quenched from the two phase cubic and hexagonal field revealed that the hexagonal phase rapidly transforms to the lower symmetry monoclinic form. Twinning and slip accompany the transformation, yielding microstructures very similar to those obtained for the tetragonal to monoclinic martensitic transformation in ZrO_2.

The tetragonal to monoclinic transition in ZrO_2 has long been known to occur by a diffusionless shear type mechanism.[7-11] This reaction can be exploited in the transformation toughening of the ceramic because the resultant volume expansion from the transformation of tetragonal particles in the matrix subjects the matrix to a compressive strain which then acts to blunt advancing crack tips, requiring higher energies for their propagation.[12] If the hexagonal to monoclinic transformation of the Y_2O_3-La_2O_3 system can be proven to be martensitic, then the Y_2O_3-La_2O_3 system may offer potential for transformation toughening at temperatures far in excess of those presently attainable in ZrO_2.

Comparison of ZrO_2 with the Y_2O_3-La_2O_3 system yields other similarities as well. Both crystallize in a cubic structure that is

based on the fluorite lattice (FCC cations with anions in all tetrahedral sites). However, the cubic phase of Y_2O_3 occurs as the low temperature form and as a defect structure (oxygen vacancies) whereas the cubic phase of ZrO_2 is only stable at high temperature. The transformation of interest in both systems occurs from a high symmetry structure (tetragonal in ZrO_2, hexagonal in Y_2O_3) to a low symmetry structure (monoclinic in both cases) and proceeds extremely rapidly. Twinning and dislocations accompany the transitions in both cases as does a volume expansion (~4.5% in ZrO_2, approximately 1-2% in Y_2O_3-La_2O_3).

Unlike the ZrO_2 system and other rare earth oxide systems, the precipitation events in the Y_2O_3-La_2O_3 binary have not been extensively studied. Most of the major work on Y_2O_3-La_2O_3 has focused on the phase diagram determination by high temperature x-ray diffraction[13,14] and limited electron microscopy studies on specific regions of the diagram by GTE Laboratories.

The major portion of this work concerns the application of analytical electron microscopy techniques to the investigation of precipitation phenomena in the Y_2O_3 rich portion of the Y_2O_3-La_2O_3 system. In particular, the nature of the precipitation of the hexagonal phase in the cubic matrix will be addressed as will its behavior as a function of time and temperature. Analytical results will be compared to present phase diagram predictions. The stability and transformation characteristics of the hexagonal phase and x-ray diffraction and TEM/STEM results of samples quenched from the single phase hexagonal field are also included.

Finally, as Raman spectroscopy has recently proven itself to be a useful analytical tool in the ceramics field, a demonstration of the technique on a pure Y_2O_3 sample as well as a brief review of some of the current pertinent literature on the theory and application of Raman scattering are also presented.

BACKGROUND

Phase Diagram

Figure 1 shows the Y_2O_3-rich high temperature portion of the Y_2O_3-La_2O_3 system. It consists primarily of a two-phase cubic and hexagonal field above a single phase cubic region for La_2O_3 concentrations up to approximately 20 mol percent and a eutectoid reaction near 1950°C for 30 mol percent La_2O_3 compositions involving a hexagonal to the cubic + monoclinic phase transition. This diagram, taken from high temperature x-ray diffraction data by Mizuno, et al.[13] and Coutures and Foex[14] exhibits some uncertainty in the limits of the two-phase cubic and monoclinic field as well as the eutectoid temperature although the cubic and hexagonal phase field appears well defined. Previous work done by GTE on 8-14 mol percent samples quenched from the two phase cubic and hexagonal field revealed cubic and monoclinic structures, possibly indicating that the limit of La_2O_3 concentrations in Y_2O_3 below approximately 1950°C may actually be less than shown on the diagram. The circles in the cubic and hexagonal region are data points obtained by GTE by microprobe analyses on large individual abnormal grains of a 12-14 mol percent Y_2O_3 sample sintered at 2070°C to 2270°C and quenched to 1400°C in 1 minute. These show excellent agreement with the cubic and hexagonal/hexagonal solvus, but exhibit some anomalies when compared with the published cubic and hexagonal/cubic solvus boundary.

Crystallography

The rare earth oxides exist in three polymorphic forms: cubic (C), monoclinic (B) and hexagonal (A). All can be described in terms

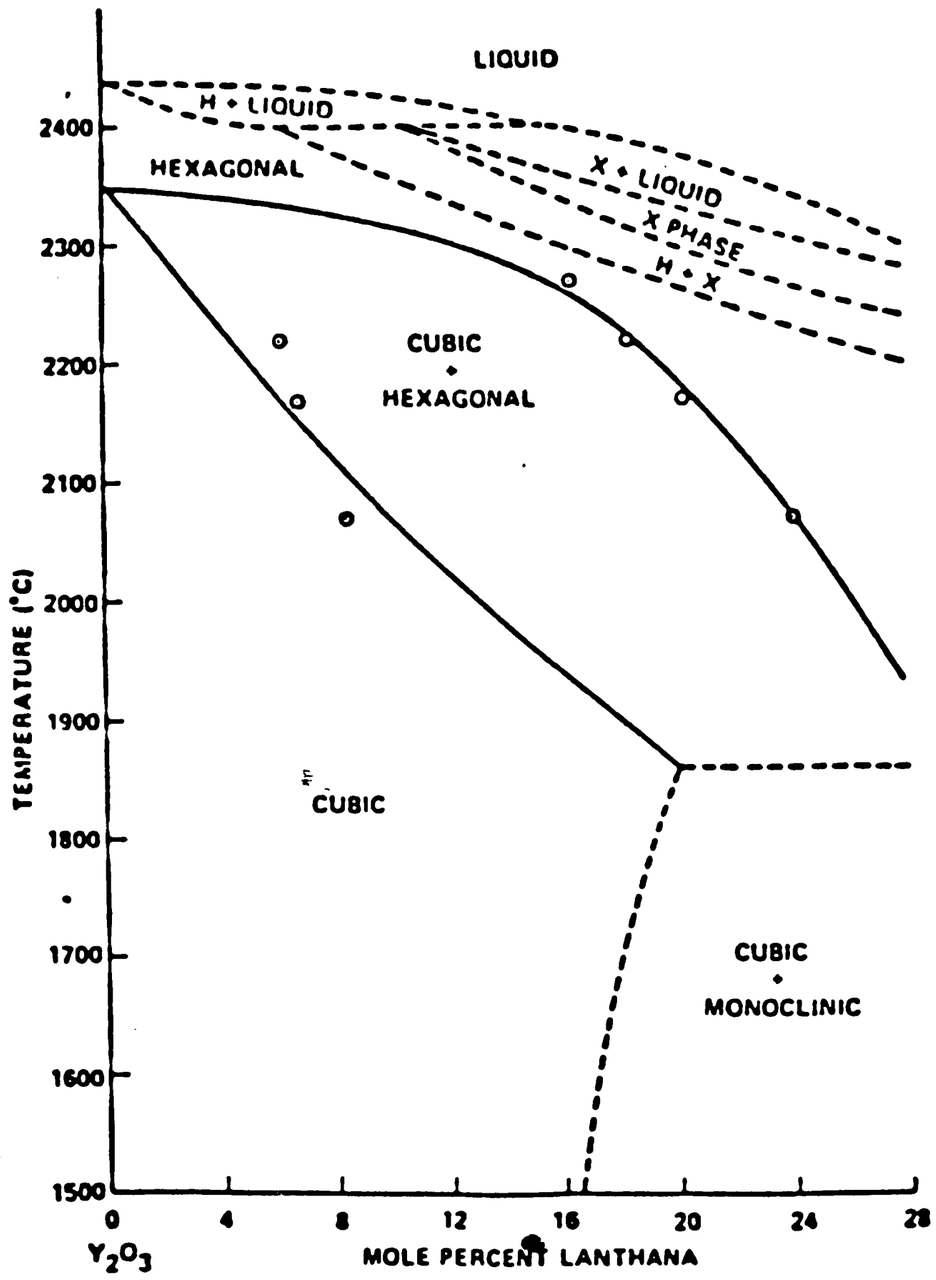

Figure 1. High temperature portion of Y_2O_3 rich region of the Y_2O_3 - La_2O_3 phase diagram (After Coutures and Foex[14], Mizuno, et al [13])

of the oxygen anion coordination.

The C type structure, the dominant form of the rare earth sesquioxides at lower temperatures, has been characterized as a defect fluorite structure in which one-fourth of the tetrahedral anion sites are vacant. Eight of these fluorite cells comprise the entire unit cell, yielding a total 16 Y_2O_3 units per cell with a lattice parameter of 10.604Å. Zachariasen's[15] early x-ray work on Y_2O_3 cubic polymorphs revealed allowed reflections for $h^2 + k^2 + \ell^2 = 2n$, indicating a BCC sublattice and so the C type polymorphs of the rare earth oxides belong to the Ia3 space group. Paton and Maslen[16] and later Caro[17] refined the structure of the cubic polymorph. The investigators confirmed the T_h^7 symmetry group*, and determined that the structure consists of a three-dimensional framework of edge-linked OLn_4 tetrahedra (Ln = rare earth metal). Each shares only four out of six edges with other tetrahedra and has each of the metal atoms common to six rather than eight tetrahedra (Figure 2a).

Within the unit cell, two sites exist for the metal ion: eight of the thirty-two metal ions occupy ¼, ¼, ¼, positions lying on the body diagonal and therefore having a three-fold cyclic rotational site symmetry (C_3), and twenty-four metal ions lie in general u, o, ¼ positions, occupying sites with C_2 symmetry which lie parallel to [100], [010], and [001]. The forty-eight oxygen ions form a distorted octahedra around the metal ions and they can be considered to be at six of the corners of a slightly distorted cube (Figure 2b). Two

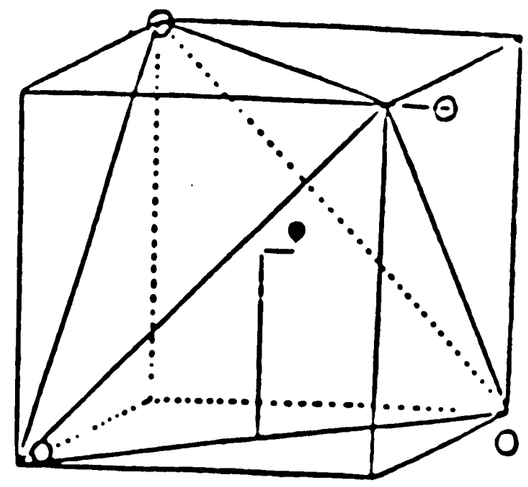

Figure 2a. Tetrahedral arrangement of rare earth metal atoms around an oxygen atom (After Zachariasen[15])

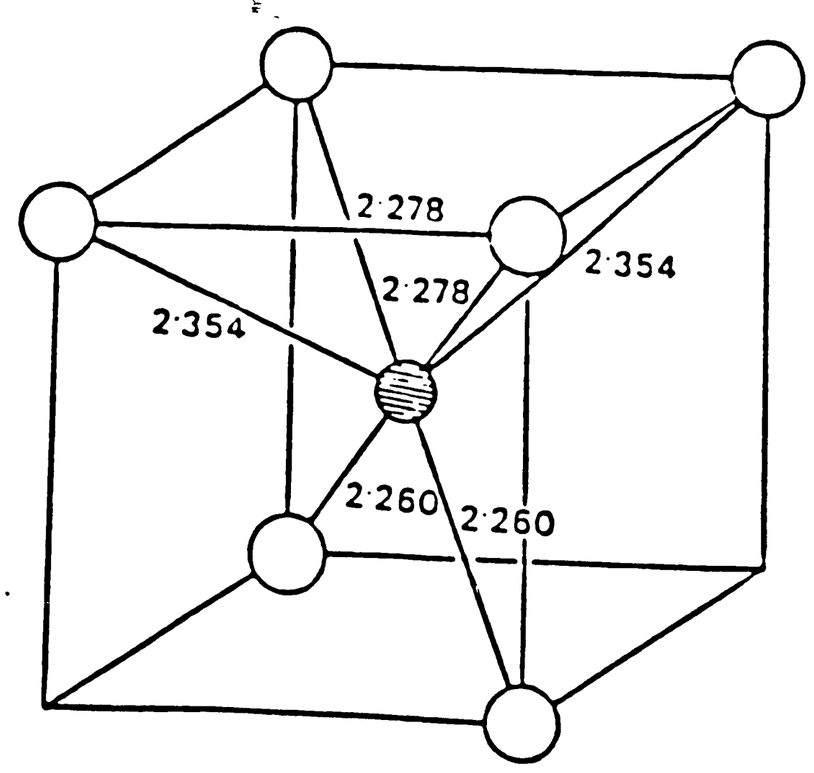

Figure 2b. Oxygen ions at the corners of a slightly distorted cube showing the six fold coordination of the rare earth ion in the general position (u,0,1/4). Oxygen - metal distances are indicated.(After Paton and Maslen[16])

configurations of these octahedra or distorted cubes are allowed: one where the missing oxygen atoms are situated on the body diagonal (0 octahedrally surrounding the ¼, ¼, ¼ cations) and another where they are situated across a face diagonal (0 octahedrally surrounding the general u, 0, ¼ positions). A diagram by Schaack and Koningstein[18] showing the atomic configurations in the cubic unit cell is shown in Figure 2c.

The hexagonal polymorph of the rare earth oxides conforms to the $P\bar{3}m1$ space group.** One Y_2O_3 molecule comprises the unit cell for a total of 5 atoms per cell. Each trivalent cation binds to 7 oxygen atoms with 3 long bonds and 4 short ones, while the oxygen atoms occupy two different sites: one binds to 5 and the other to 4 metal atoms, respectively.[18] The A-polymorph is essentially a close packed structure of MO_7 coordination of the metal atoms and the ion arrangement is very similar to the fluorite lattice of rare earth dioxides.[19] The metal atoms sharing the short bonds with the oxygen ions form a tetrahedra around the oxygens (O_{II}) while the oxygens of the longer bonds (O_I) have 6 octahedral metal neighbors. The structure has been described as sheets of edge linked OLn_4 tetrahedra with the remote oxygen atoms between the sheets ($(LnO)_2O$). Each sheet

---

*T_h^7 refers to the Schoenflies notation indicating tetrahedral coordination of the oxygen with a three-fold axis in each vertex and a two-fold passing through centers of opposite sides; the h indicates a reflecting plane perpendicular to the high symmetry axis.

**Primitive hexagonal cell with a reflection plane perpendicular to the three-fold axis of rotation, a mirror plane parallel to the face diagonal, and a monad rotation around axis perpendicular to the c-axis.

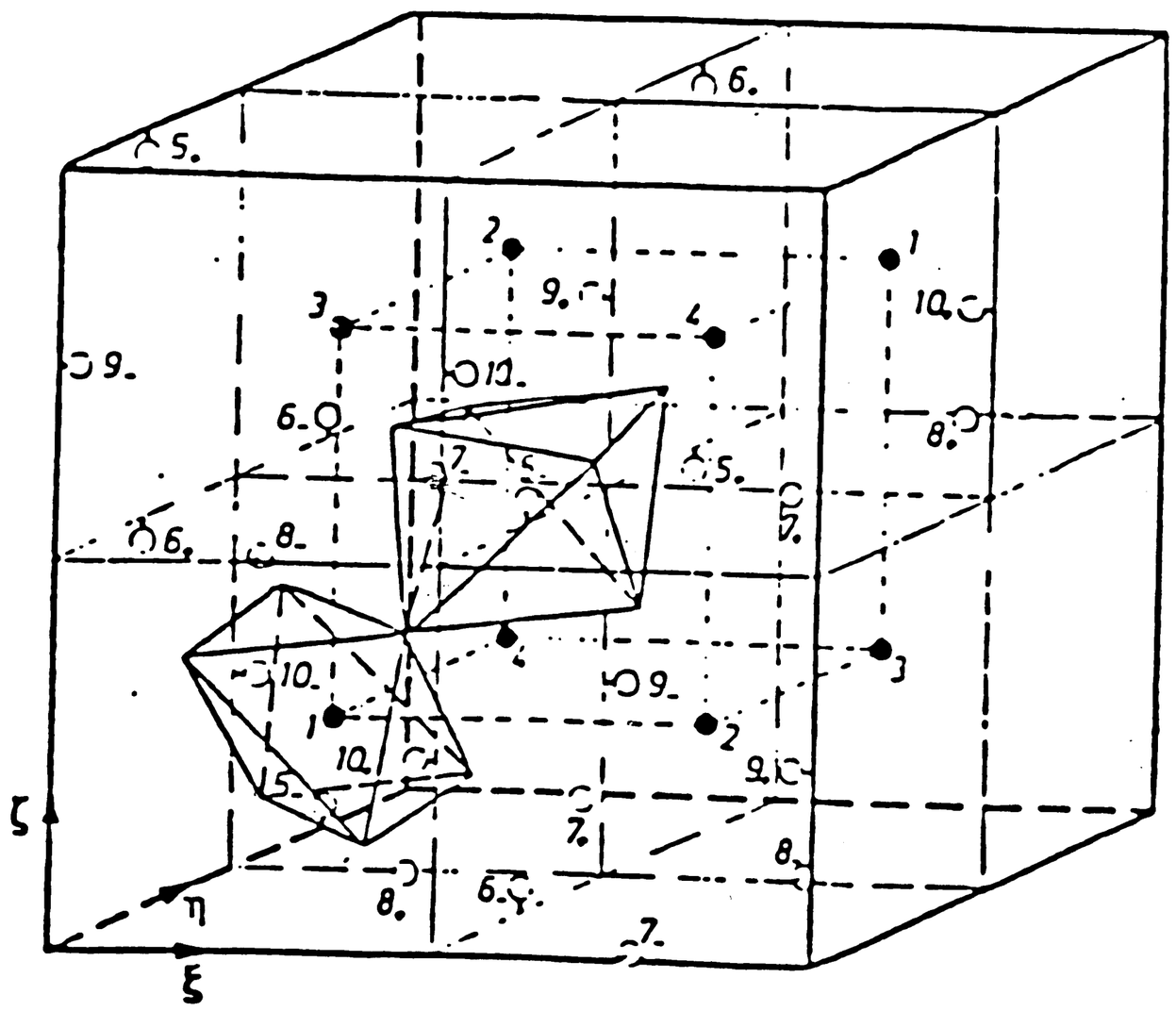

Figure 2c. Unit cell of the rare earth oxide cubic polymorph. Full circles: eight rare earth ions occupying (1/4, 1/4, 1/4) positions lying on body diagonal. Others: twenty four rare earth ions in general (u,0, 1/4) positions. The two oxygen configurations are denoted by the distorted octahedra shown. (after Schaack and Koningstein [18])

forms by tetrahedra sharing 3 edges as each corner is common to 4 tetrahedra (Figure 3a).[17]

Slight displacements of the $(LnO)_n^{n+}$ layers with respect to each other in the A-type polymorph along the <1100> directions yields the B-type monoclinic structure. The unit cell for this polymorph may be considered to consist of six distorted trigonal units (or three primitive hexagonal units). It belongs to the space group C2/m indicating a base centered monoclinic cell with a two-fold axis of rotation (along the [010] direction) and a mirror plane of reflection perpendicular to the [010] axis. Six molecular formula units comprise the monoclinic unit cell, and like the hexagonal cell, it shares a seven-fold coordination of the metal ion.

Gouteron et al.[21] demonstrated the similarities between the two structures showing that the cell parameters for the A and B polymorphs relate to each other by the following equations:

$$a_B = a_A - b_A + 2c_A$$

$$b_B = -a_A - b_A$$

$$c_B = a_A - b_A - c_A$$

The authors further show that the two oxygen sites of the hexagonal or trigonal phase become five different sites in the monoclinic structure as the tetrahedrally coordinated oxygen of the hexagonal phase become three different distorted tetrahedra around oxygen atoms in the B-type polymorph. The octahedral O_I positions split into different groups as well. In all, the environs of three of the five groups of oxygen retain similar environs in the B polymorph as they had in the A-form.

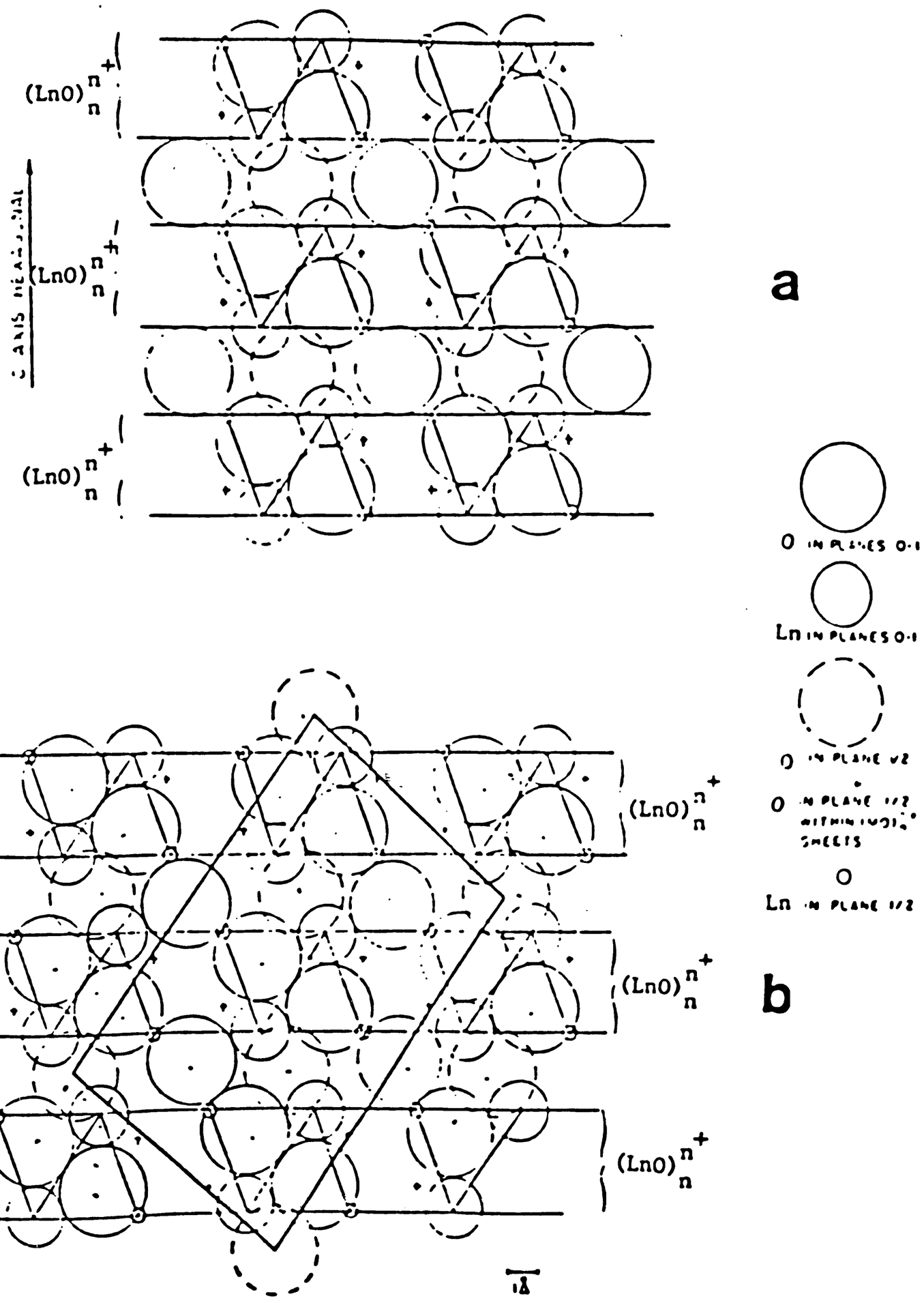

Figure 3. Stacking sheets of $(LnO)_n^{n+}$ layers with oxygen atoms in between. a.) Hexagonal Ln_2O_3 structure with plane of paper parallel to (110). b.) Monoclinic structure with plane of paper perpendicular to the b [010] monoclinic axis. Unit cell projection is outlined (After Caro[17])

Three different cation sites exist with five different anion sites whose anions bind to 4, 5 or 6 metal ions.[20] In terms of tetrahedral arrangements, the structure doesn't deviate significantly from the A-form, possessing the same kind of $(LnO)_n^{n+}$ sheets except that the succession of sheets are not as regular along what was the C-axis of the hexagonal cell A-structure. This is a direct result of the oxygen atoms between the sheets not being as far from the rare earth atoms (Figure 3b).

Roth and Schneider[22] have developed a phase diagram exhibiting the relative stability of the various polymorphs as a function of temperature and cation radius (Figure 4). As indicated, the oxides of the largest ions (lanthanum) most commonly exhibit the hexagonal A-structure while the smaller ions crystallize in the cubic form. The ionic size determines the behavior of any mixture of the rare earth oxides at elevated temperature. Small differences in radii as expected infer an extensive solid solubility whereas compound formation can be predicted for large cationic differences as in the perovskite $LaYO_3$ (La^{+3}=1.14A, Y^{+3}=0.91A).

A comparison of molar volumes of the three structure types suggest that increasing pressure should favor the monoclinic over the cubic forms and the hexagonal over both the cubic and monoclinic, the former transition requiring a shift from the 6:4 coordination with oxygen vacancies to the 7:(4,5,6) coordination of the monoclinic structure. Figure 5 shows the similar volumes resulting from the nearly identical lanthanide contractions for the hexagonal and monoclinic phases and the greater values achieved in molar volume for

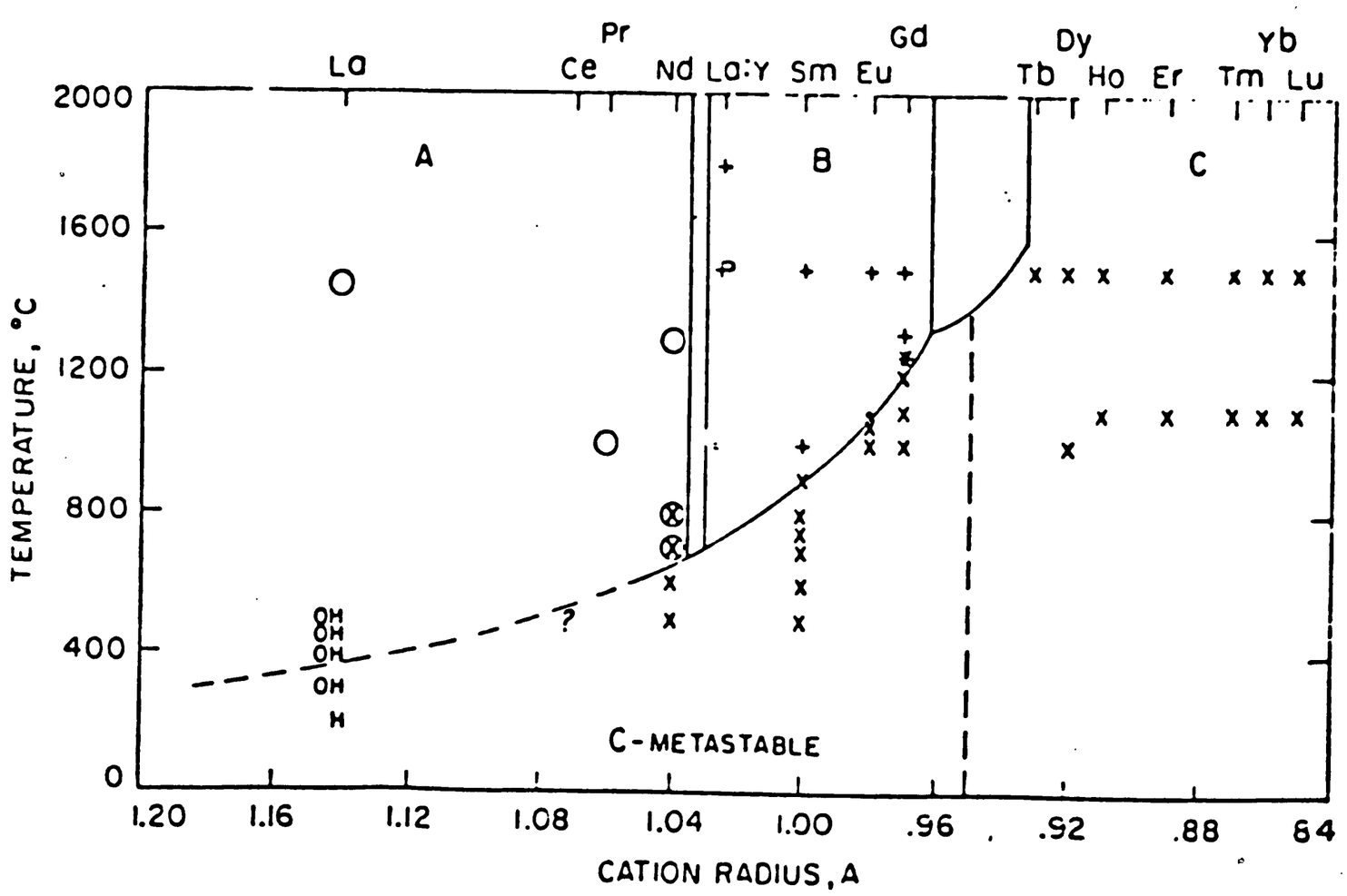

Figure 4. Stability relations of the A - hexagonal (O), B - monoclinic (+), and C - cubic (X) forms of the rare earth sesquioxides (After Roth and Schneider[21])

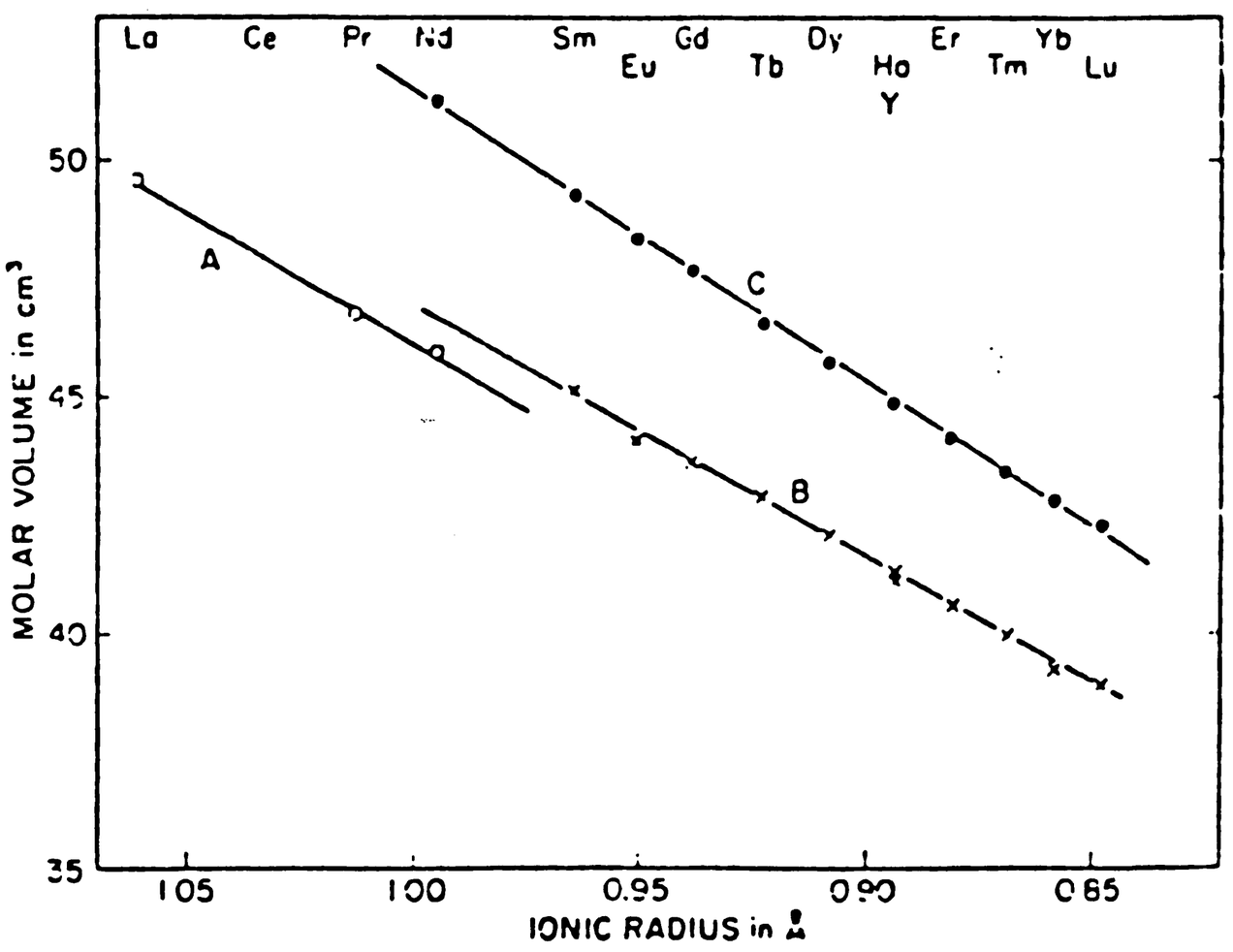

Figure 5. Comparison of molar volumes for the A - hexagonal, B - monoclinic, and C - cubic forms of the rare earth sesquioxides. (After Hoekstra[20])

the cubic phase. The hexagonal to cubic phase transformation yields a substantial 8% volume increase while the hexagonal to monoclinic transition only produces a 1% expansion. Hoekstra[20] successfully stabilized the monoclinic form of Y_2O_3 with high temperatures and pressures and measured the following lattice parameters for the B-cell:

$a = 13.91 \pm 0.1$ A $b = 3.483 \pm .003$ A $c = 8.593 \pm .005$ A

$\delta = 90°$ $\beta = 100.15 \pm .05°$ $\gamma = 90°$

When compared to the lattice parameters of other rare earth oxide monoclinic cells, very close agreement can be found, especially for the stable monoclinic Gd_2O_3 structure ($a = 14.061$, $b = 3.566$, $c = 8.760$, $\beta = 100.1$) whose x-ray diffraction data has been fully characterized by Guentert and Mozzi.[23]

Phase Transformations in Rare Earth Oxides

Previous studies on phase transitions involving the cubic polymorph of the rare earth oxides revealed an increasing activation energy and transformation temperature with decreasing cation size. This suggests that the rearrangement and diffusion of the larger oxygen ions control the rate in these reconstructive transformations involving a change in the primary coordination.

The monoclinic to cubic transformation has been shown to be a reversible one while the cubic to hexagonal transformation has not been proven reversible. The interlayer planes of oxygen atoms in the B-form can more easily move into the tetrahedral coordination present in the low temperature cubic form as it only requires a slight

displacement of the $(LnO)_n^{n+}$ sheets in B Ln_2O_3 with respect to one another by ½[010] coupled with a slight increase in their separation.[17]

TEM Studies of Phase Transformations in Rare Earth Oxides

The transformation of the rare earth hexagonal and monoclinic polymorphs to the cubic structure is believed to be a reconstructive type involving broken and reformulated bonds. The hexagonal and monoclinic phases are closely related layered structures of $(LnO)_n^{n+}$ with $O^{=}$ ions separating the layers which are stacked parallel to the (00·1) basal plane of the hexagonal cell and to the $(20\bar{1})$ plane of the monoclinic cell. The crystallographic relationship has been verified by Boulesteix et al.[24,25] through in-situ oxidation and heating TEM studies of the hexagonal to monoclinic phase transitions in Nd_2O_3 and Sm_2O_3.

The B-type phase forms epitaxially as bands in the hexagonal matrix upon rapid cooling and being unstable, disappears within minutes after formation. Electron diffraction data obtained from similar studies on Pr_2O_3 by the same investigators yielded the following epitaxial relationship between the hexagonal and monoclinic polymorphs:[26]

$$(100)^{A}_{Pr_2O_3} \,||\, (111)^{B}_{Pr_2O_3}$$

$$(100)^{A}_{Pr_2O_3} \,||\, (313)^{B}_{Pr_2O_3}$$

The hexagonal to monoclinic transformation was shown to be of a cooperative or diffusionless nature and the identical compositions of

the epitaxially related bands of the hexagonal and monoclinic phases lent further credence to a martensitic character for the transformation.

High resolution electron microscopy studies by Salem, Dobie, and Yangui[25] revealed that the actual transformation proceeds by the epitaxial growth of the monoclinic bands into the hexagonal phase in a manner which results in constraint at the interface. Any monoclinic phases which develop with orientations that do not yield a strained interface do not grow, indicating that strain energy drives the reaction as in martensitic transformations. Similar studies of Pr_2O_3 exhibited the instability of the monoclinic "microdomains" when elastic stresses are released as by incoherency.

The martensitic characteristics of the transformation become evident when considering the relationship between the two polymorphs. The monoclinic cell derives from the hexagonal structure by a slight deformation of the hexagonal basal plane and a 3.2° tilt of the C-axis (hexagonal). The $(LnO)_n^{n+}$ layers slide along the three equivalent directions $[01\bar{1}0]$, $[10\bar{1}0]$, $[1\bar{1}00]$ of the hexagonal cell (perpendicular to the C-axis) as the epitaxial relationship maintains continuity between the $(LnO)_n^{n+}$ complex groups of the two phases. (The 00·1) basal plane of the hexagonal polymorph becomes parallel to the $(20\bar{1})$ plane of the monoclinic cell and the hexagonal lattice C-axis inclines to become the $[10\bar{1}]$ direction of the B-polymorph which is nearly perpendicular to the $(LnO)_n^{n+}$ layers. The {110} planes and the axes perpendicular to them become 2 {313} planes and 1 {020} plane of the monoclinic cell. Twinning of the crystal has been reported along

planes containing the [10$\bar{1}$] direction as well as the {313} and {111} planes of the monoclinic phase.[28,29]

The HREM studies by Salem, et al. revealed a potential ferroelastic character to the hexagonal to monoclinic phase transition. The term ferroelastic refers to a transformation in which different orientation domains of the ferroelastic structure (monoclinic phase) occurring during the phase change can be transformed into each other by strain. It can occur between a high temperature high symmetry structure and the low symmetry low temperature structure providing the point group of the low temperature phase is a subgroup of the high temperature phase and when each belongs to a different crystal system.

As mentioned previously, the monoclinic structure can be derived from the hexagonal polymorph. As the volume of the monoclinic primitive cell exceeds that of the hexagonal primitive cell by a factor of three, three neighboring unit cells of the hexagonal polymorph deform in three slightly different ways to yield one primitive unit cell of the monoclinic phase. (Actually, since the monoclinic cell is base centered, its volume equals twice that of the primitive B cell and therefore six times the volume of the hexagonal unit cell. Thus, six cells of the hexagonal phase can deform to form one monoclinic cell as shown in Figure 6.) The deformation of the hexagonal phase in three different ways gives rise to different orientation domains or variants of the monoclinic phase, the number of which depend upon the space groups involved.

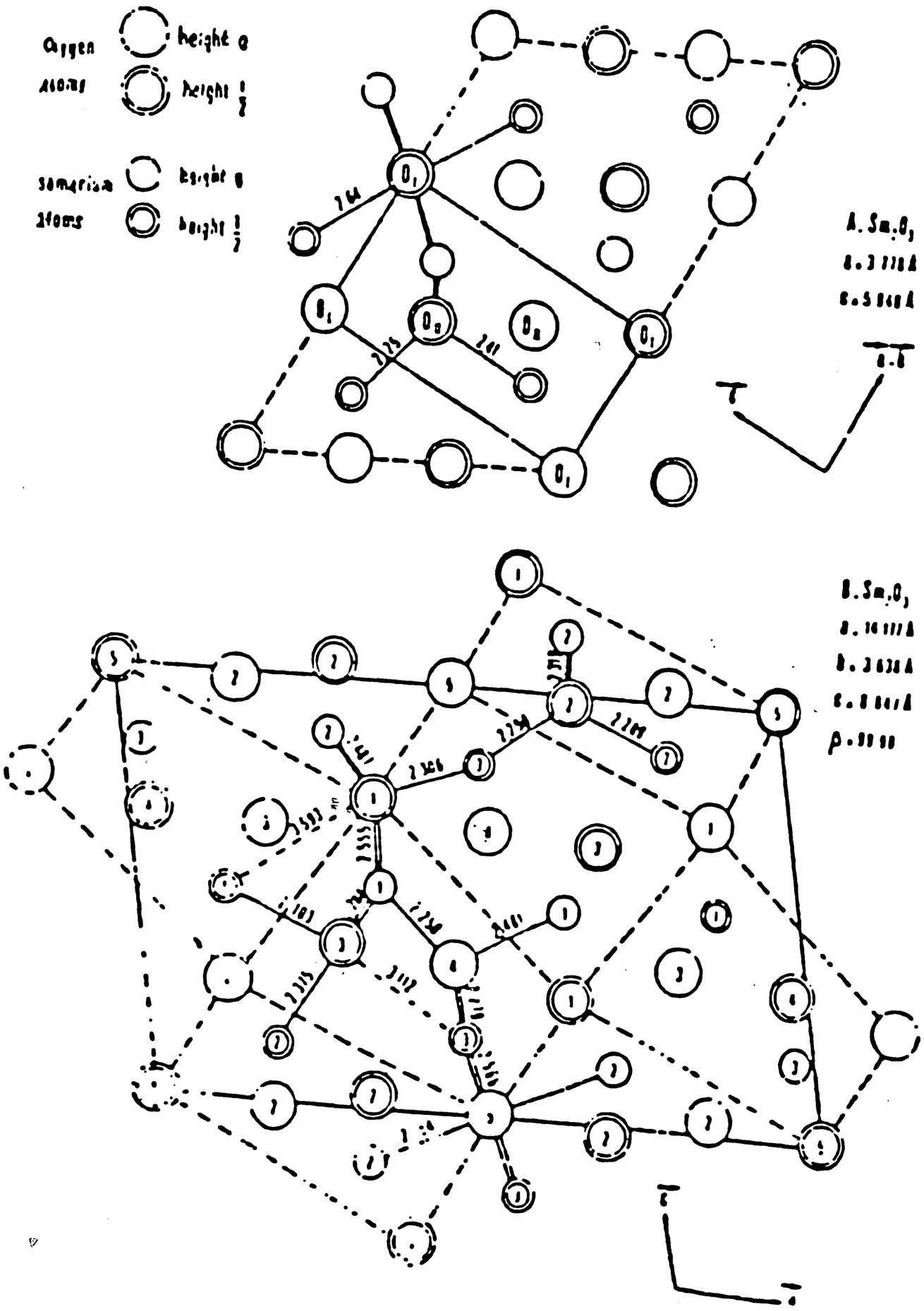

Figure 6. Projection in the (010) plane of the monoclinic B-Sm_2O_3 structure , showing the individual hexagonal cells that deform to produce the monoclinic polymorph. (After Gouteron et al [21])

The symmetry elements of the monoclinic phase are a two-fold axis along [010], the b axis of the cell, a mirror plane parallel to the (010) plane, and an inversion center located at the origin and at the base center points (½, ½, 0). The hexagonal cell possesses the same symmetry elements in addition to $2\pi/3$ and $4\pi/3$ rotations about the three-fold axis. During the transition, the three-fold axis, the two-fold axis and the two symmetry planes are lost, as the latter two give rise to four (mechanical) twins in the B phase which relate the different orientation domains to each other. Yangui and Boulesteix[30,31] have determined the orientations of these domains and found that as a result of this mechanical twinning phenomenon which relates the different domains to each other, mechanical straining can transform one orientation domain of the B phase into another. As the hexagonal point group is $\bar{3}m$ and that of the monoclinic cell is 2/m, a subgroup of $\bar{3}m$, and since both structures belong to different crystal systems, the phase transformation can be considered ferroelastic. Figure 7 shows an example of the various orientations of the domains.

Martensitic Phase Transformations and Toughening

Probably the most comprehensive definition of a martensitic transformation that differentiates it from other displacive transformations is proposed by Cohen, Olsen and Clapp.[32] According to the authors, a martensitic transformation infers a "lattice distortive, virtually diffusionless structural change having a dominant deviatoric component and associated shape change such that the strain energy dominates the kinetics and morphology during the transition."

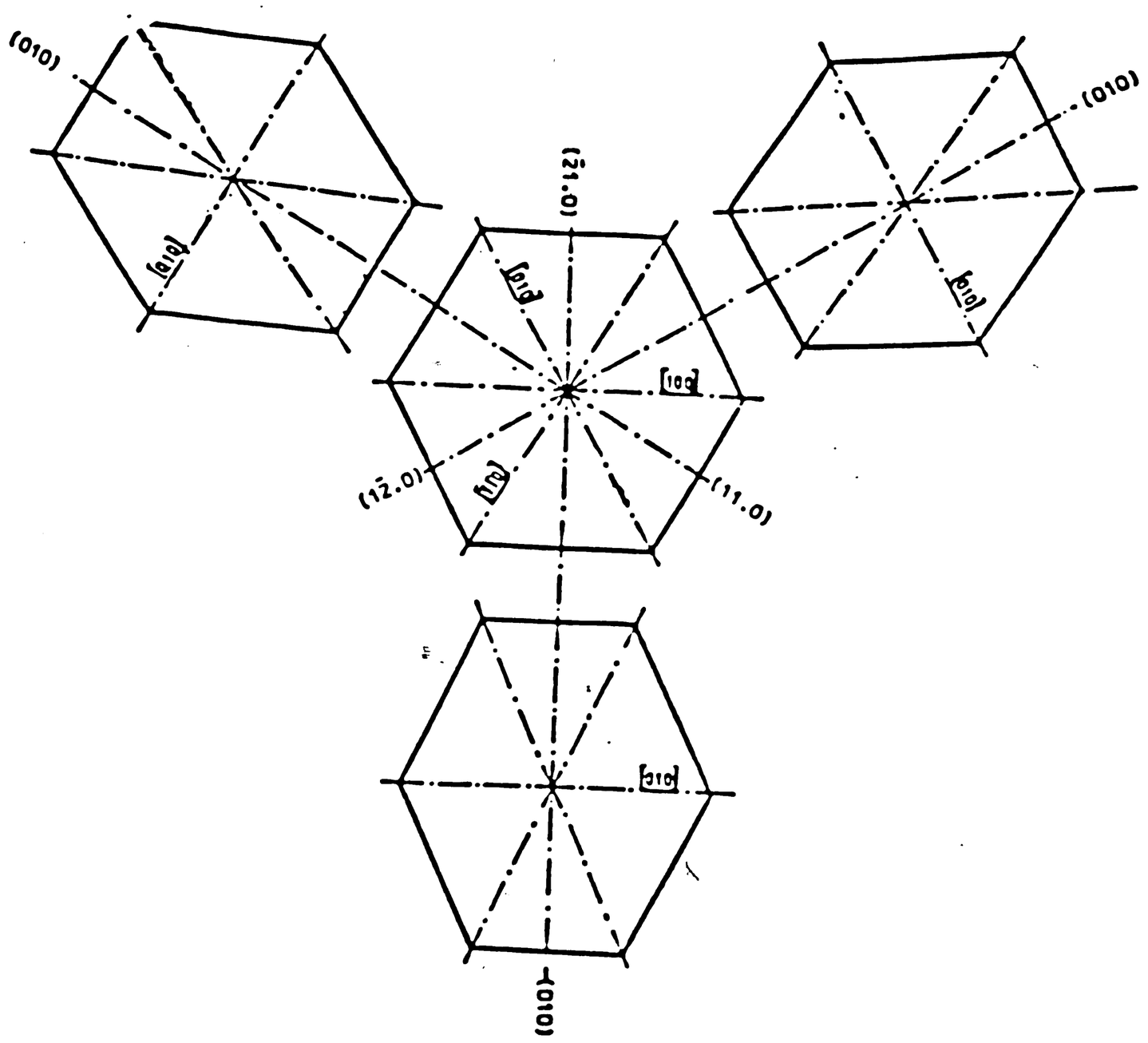

Figure 7. Relative position of the three different orientation domains of the monoclinic phase related to the hexagonal structure. (after Salem et..al. [27])

Lattice distortive refers to a homogeneous strain which converts one Bravais lattice into another[32,33] by a shear-type mechanism that maintains coherency between the parent and product phases across a common undistorted, unrotated habit plane, along which the plates of martensite lie. The Bain deformation provides the lattice distortion but cannot account for the undistorted unrotated habit plane. Therefore, a lattice invariant shear involving atom shuffles is required to maintain lattice symmetry and crystallography, while yielding an undistorted plane. This latter mechanism produces an elastic strain energy which provides the driving force for the reaction and dominates the kinetics and morphology.

Finally, because the undistorted plane derived from the combined Bain strain and lattice invariant shear differs in orientation in the parent and product phases, rotation of the parent structure is necessary to yield the undistorted unrotated habit plane. According to Cohen, et al. this undistorted plane, usually of irrational indices and whose purpose it is to transfer atoms in proper orientations from the parent to product phase results from the dominance of the deviatoric (shear) component parallel to it as opposed to the dilational (tensile) component perpendicular to the interface which will cause distortion.

Twinning and slip accompany the transformation to accommodate the lattice deformation since the atom displacements only occur over very small distances less than one atomic spacing. It is this coordinated, orderly movement of atoms that yields the same atomic neighbors in both the parent and product phase, yielding composition invariance,

and thus providing the diffusionless nature to the transformation. Though not essential for the definition of martensitic reactions, most of these transformations require further cooling to promote continued transformation.[33,34] Continued cooling aids in overcoming strains induced by the change in crystal structure that act to oppose the driving force for the transformation since the nature of the process is diffusionless.

Presently, the ZrO_2 (and the HfO_2) systems exhibit phase transformations of a martensitic character.[35] The tetragonal polymorph transforms in a diffusionless manner to the monoclinic form consisting of layers of triangularly coordinated oxygen polyhedra OZr_3 and distorted tetrahedra of OZr_4. The reaction proceeds with less than one interatomic distance displacement of oxygen atoms in tetrahedral coordination to triangular coordination in the (100) plane of the monoclinic phase.

The tetragonal phase can be stabilized within the matrix if coherency is maintained across the interface. Once incoherency results, spontaneous transformation to the monoclinic symmetry yields a three to four percent volume expansion which subjects the surrounding matrix to a compressive strain. The interaction of a crack tip with a tetragonal particle originally coherent with the matrix results in a loss of coherency and an associated loss of constraint on the particle by the matrix. This stress induced transformation and resultant strain induced by the volume expansion acts against the tensile forces of the crack tip to blunt it, requiring higher energies for crack propagation. The closer the particles are to the

transformation condition, the larger will be the transformation zone size in the crack tip vicinity and therefore the greater the toughness. This is the underlying principle of transformation toughening.

Co-precipitation of Ceramic Powders

Of the many methods available to produce mixtures of ceramic powders, the co-precipitation technique has gained prominence due to its ability to mix components intimately on an atomic scale. Every material has its own co-precipitating recipe therefore the conditions of precipitation vary with the system and must be well controlled to attain the desired particle size, shape and distribution as well as the chemical homogeneity all of which greatly influence the microstructure of the sintered compact. Parameters which require careful monitoring include the pH of the precipitation solution, time in the solution, rate of precipitation, and the temperature.[36] Other considerations involve yields, decomposition rates and reactions, type of precipitate (single compound, solid solution, or mixture of compounds), reactivity and sinterability, and residual cations and anions. Impurities introduced during the precipitation procedure can grossly affect sintering behavior. For example, O'Bryan, Gallagher, Monforte and Schrey[37] showed that the retained Cl^- ions from the co-precipitation of $Ni(NO)_3$ and $FeCl_2$ yields a regression in the sinterability of nickel ferrous ferrite as gaseous ferrous chloride ($FeCl_2$) fills and expands pores causing sample cavitation.

Segregation of the components by agglomeration must also be avoided in order to attain fine thoroughly blended powders and prevent pore entrapment in the sintered body. Dragoo and Domingues[38] found

that precipitate agglomerates occur when the concentrated solutions of reactants are mixed in such a way that the reaction doesn't take place uniformly.

The temperature of precipitation and subsequent calcination to the oxide can affect powder size and sinterability. Investigations on ThO_2-Y_2O_3 co-precipitation by the oxalate process show an increase in crystal size with increasing precipitation temperature and calcining temperature with no dependence of sintered densities on the temperature of calcination.[39] However, Overs and Riess[40] in their production of Gd_2O_3 doped CeO_2 by the oxalate process show a very weak dependence of precipitating temperature on precipitate size, as large particles form for high temperatures (44°C) and smaller particles for temperatures near 7°C. However, the BET analysis attains a maximum for calcination temperatures near 350°C and decreases with increasing calcining temperatures up to 1000°C.

For the co-precipitation of rare earth oxides, the oxalate and sulfate processes are most common.[41,42,1] The oxalate process however yields fairly easily removable hydrocarbon impurities as opposed to the sulfur impurities of the latter technique which segregate to grain boundaries during sintering to form a wetting grain boundary phase. Therefore, the "cleaner" oxalate process was used in this work.

Analytical Electron Microscopy

k-Factor Determination

The application of analytical electron microscopy studies to the Y_2O_3-La_2O_3 binary requires measurement of the Cliff-Lorimer

k-factor for this system. Accurate quantitative analyses depend upon this constant of proportionality which relates elemental characteristic x-ray peak intensities (I_Y,I_{La}) to their respective concentrations (C_Y,C_{La}). The k-factor is independent of composition and foil thickness if the intensities of the two desired elements are measured simultaneously and the thin film criterion is obeyed. However, it has been shown to be function of the operating voltage.[43] Absorption by the beryllium window, gold surface layer, or silicon dead layer of the x-ray detector must be considered especially in the case of light element analysis where beryllium window absorption can become significant. This holds special importance in this study as the yttrium L lines used for microanalysis are of a very low energy (1.92 keV) almost comparable to the K lines of the lighter elements. The k-factor can vary with the instrument on which it is measured due to detector geometry and efficiency. Therefore, microanalyses should always be performed under the same conditions as which the k-factor is measured. Measurement only requires a thin foil containing the elements of interest, whose compositions are known, and which is stable under the beam at the operating voltage.[44]

Thin Film Criterion

Absorption of characteristic x-rays by the sample depends upon the sample composition and foil thickness and may affect the final outcome of the microanalysis.[45] If the foil thickness exceeds a critical value, usually taken to be the limit where upon a 10% error is involved in the composition obtained, a thickness correction must be applied to the Cliff-Lorimer equation. Goldstein et al.[43] gave

an expression for the Cliff-Lorimer equation which accounts for the absorption effects:

$$\frac{C_B}{C_A} = k_{AB} \frac{I_A}{I_B} \exp(-D)$$

When D exceeds 0.1, absorption is considered significant. The value D which defines the thin film criterion is related to the foil thickness t by the expression $D = [(\rho t/2)(\chi_B - \chi_A)]$ where ρ represents the specimen density, t the thickness, and χ_B, χ_A the products of the mass absorption coefficient for the characteristic x-ray of element A (or B) in the specimen and the cosecant of the x-ray take-off angle α (20° in the Philips EM400T). Values of the mass absorption coefficients are tabulated in the literature.[46]

Thin Foil Spatial Resolution

Interaction of the electron beam with the sample as it passes through the foil results in an increase in the beam diameter with depth into the foil. The amount b that the size of the beam exceeds the initial probe diameter d depends on foil thickness and helps define the minimum distance between which two microanalysis readings can be taken in the foil before one reading overlaps the other. Reed's[43] model of electron scattering in a thin foil yields the following expression for b:

$$b = 625 \cdot \frac{\rho}{A}^{\frac{1}{2}} \frac{Z}{E} t^{3/2}$$

where again ρ represents the density (g/cm^3), A the molecular weight or atomic weight, Z the atomic number, E the excitation voltage (kV) and t the thickness (cm). Thus, knowledge of this beam spread parameter imposes resolution restrictions on the microanalysis.

Specimen Thickness Measurements

Accurate foil thickness measurements can be obtained by tilting a convergent beam electron diffraction pattern into a two-beam condition and adjusting the objective lens to form the probe at the specimen plane. The resulting intensity minima or fringe patterns which occur symmetrically within the diffracted disc contain the information on foil thickness in the region from which the pattern was obtained.

The deviation parameter Si for each of the fringes (i) is defined as follows:

$$Si = \frac{\lambda}{d_{hkl}} \frac{\Delta\theta_i}{2\theta_B}$$

where λ = wavelength (A°)

d_{hkl} = interplanar spacing for diffracted excited disc

$\Delta\theta_i$ = distance of intensity minima from center of diffracted disc

θ_B = Bragg angle or half the distance between transmitted and diffracted beam.

Values for the thickness are obtained from straight line plots of $(Si^2 + 1/\zeta_g{}^2)t^2 = n_i{}^2$ where ζ_g is the extinction distance, t the thickness,

and n_i represents arbitrarily assigned integers which yield the best fits to a straight line for the various values of Si. The interception of the $1/n_i^2$ versus $(Si/n_i)^2$ plots with the $(Si/n_i)^2$ axis yields $1/t^2$.[43]

Raman Spectroscopy

Raman spectroscopy has recently gained popularity in the ceramics field for phase identification and studies of crystal symmetry, especially now that improved laser optics have reduced analyses volumes to less than 6 cubic microns and detection limitations of second phases to greater than five volume percent.[47] Phillipi and Mazdiyazni[48] have successfully characterized various phases in ZrO_2 by Raman scattering and found the technique to be more sensitive than x-ray diffraction to small changes in the crystal lattices. X-ray diffraction requires a periodicity in the sample over a length of at least 50 Å which renders it useless in cases where changes occur before such long range order is achieved as in the onset of crystallization and phase transformations.[49] Clark and Adar[50] have measured the size of transformation zones surrounding crack tips involving the martensitic tetragonal to monoclinic transition in transformation toughened ZrO_2 alloys using the Raman technique.

Besides the sensitivity of the phenomena to slight changes in lattice structure, Raman spectroscopy offers other advantages including:[51]

a) Molecular specificity - The frequency shifts of the scattered light are related to the vibrational frequencies of the observed molecules, providing information on the local molecular environment

and structural coordination which allows for fingerprinting of characteristic species.

b) Non-destructive nature - If sample is non-absorbing, there is no destruction of the sample although sample decomposition has been reported under very strong beams.

c) Ambient conditions - No vacuum requirements necessary nor any sample preparation procedure.

d) Simplicity of spectra - Only fundamental vibrational modes are seen under normal conditions, and

e) Range of applications - All states of matter can be investigated, liquids as well as solids and gases.

Disadvantages of the technique result mainly from the inherent weaknesses of the Raman effect which is by nature a very low light intensity phenomenon. Local heating as a consequence of incident radiation absorption by the sample under high intensity lasers can result in sample instability. Quantitation procedures presently are lacking due to an underdeveloped theory of photon inelastic scattering. However, probably the major problem to be addressed whenever using the Raman technique is the fluorescence effect which tends to produce false peaks in the spectrum and makes the detection of the weaker Raman spectra difficult.

The Raman effect is an inelastic scattering process between photons of monochromatic light and molecules of a solid, liquid, or gas. Photons of the incident beam with energy $h\nu_o$ encounter molecules in the ground state E_o or excited state E' which scatter the incident photons resulting in a scattered frequency $\nu_o \pm (\frac{E_o - E'}{h})$. This

scattering results mainly from the vibrational energy of the molecules within the sample and appears as altered frequencies, i.e. frequency shifts or displacements of Raman spectral lines from the exciting line ν_o which are identical with the frequency of molecular vibrations in the sample.

A photon, upon colliding with a molecule, can be scattered elastically where no energy change occurs such that $E=h\nu_o$ before and after the collision (Rayleigh scattering), or inelastically where the conservation of energy requires

$$h\nu_o + \tfrac{1}{2}mvo^2 + E_o = h\nu' + \tfrac{1}{2} mv'^2 + E' \qquad (1)$$

The $\frac{1}{2}mv^2$ terms refer to the translational kinetic energy of the molecule before and after the collision, the E terms to the molecular internal energy of the molecule, and the $h\nu$ terms describe the photon energies. Conservation of momentum for the collision yields

$$mv_o^{\text{molecule}} + \frac{h\nu_o^{\text{photon}}}{c} = mv' - \frac{h\nu'}{c} \qquad (2)$$

resulting in a momentum change $m(v'-v_o)$ equal to $h(\nu'+\nu_o)/c$. (3)

As the velocities of the molecules before and after the collision with a photon are relatively small, i.e. $v_o = v'$,

$$h\nu_o + E_o = h\nu' + E' \qquad (4)$$

or $$(E_o - E'/h = (\nu' - \nu_o)$$

Thus, the photons that collide with molecules either lose energy (Stokes: $\nu_s = \nu_o - \nu_i$) or gain energy from the molecules (anti-Stokes:

$\nu_{as} = \nu_o + \nu_i$) as they decrease or increase respectively their frequency ν_o by the vibrational frequency of the molecule ν_i.

Molecular vibrational energy is quantized and defined by the relation $E=(u + \frac{1}{2})h\nu$, where u represents the vibrational quantum number. The number of molecules n_i in the first excited vibrational level ($u = 1$, $E = 3/2\ h\nu_i$) relative to the number in the ground vibrational state n_o ($u = 0$, $E = \frac{1}{2}h\nu_i$) is described by the Boltzman distribution:

$$n_i = n_o \exp\ (-(^3/_2 h\nu_i - {}^1/_2 h\nu_i)/kT)$$

As $h\nu_i$ is greater than kT at room temperature, most molecules will possess the minimum energy $\frac{1}{2}h\nu_i$. Therefore, as a result of Boltzman statistics, photons of energy $h(\nu_o - \nu_i)$ are more widely observed than those with energy $h(\nu_o + \nu_i)$, making the Stokes Raman spectra the one most easily studied. The diagram of Figure 8 shows the energy transitions described above for the various scattering processes.

An alternative way of viewing the Raman phenomenon is to invoke the wavelike nature of light rather than the particle (photon) nature. Monochromatic light with a wavelength much greater than the molecular dimensions of the sample through which it is passing, subjects the molecules to an oscillating electrical field which oscillates at the frequency of the lightwave, ν_o. Electron displacement results within this field and the induced oscillating dipole in the molecule radiates light.

The induced dipole moment M is related to the electric field E (of amplitude E_o and a fluctuation frequency of ν_o) by the equation:

$$M = \alpha\ E_o \cos\ (2\pi\nu_o t).$$

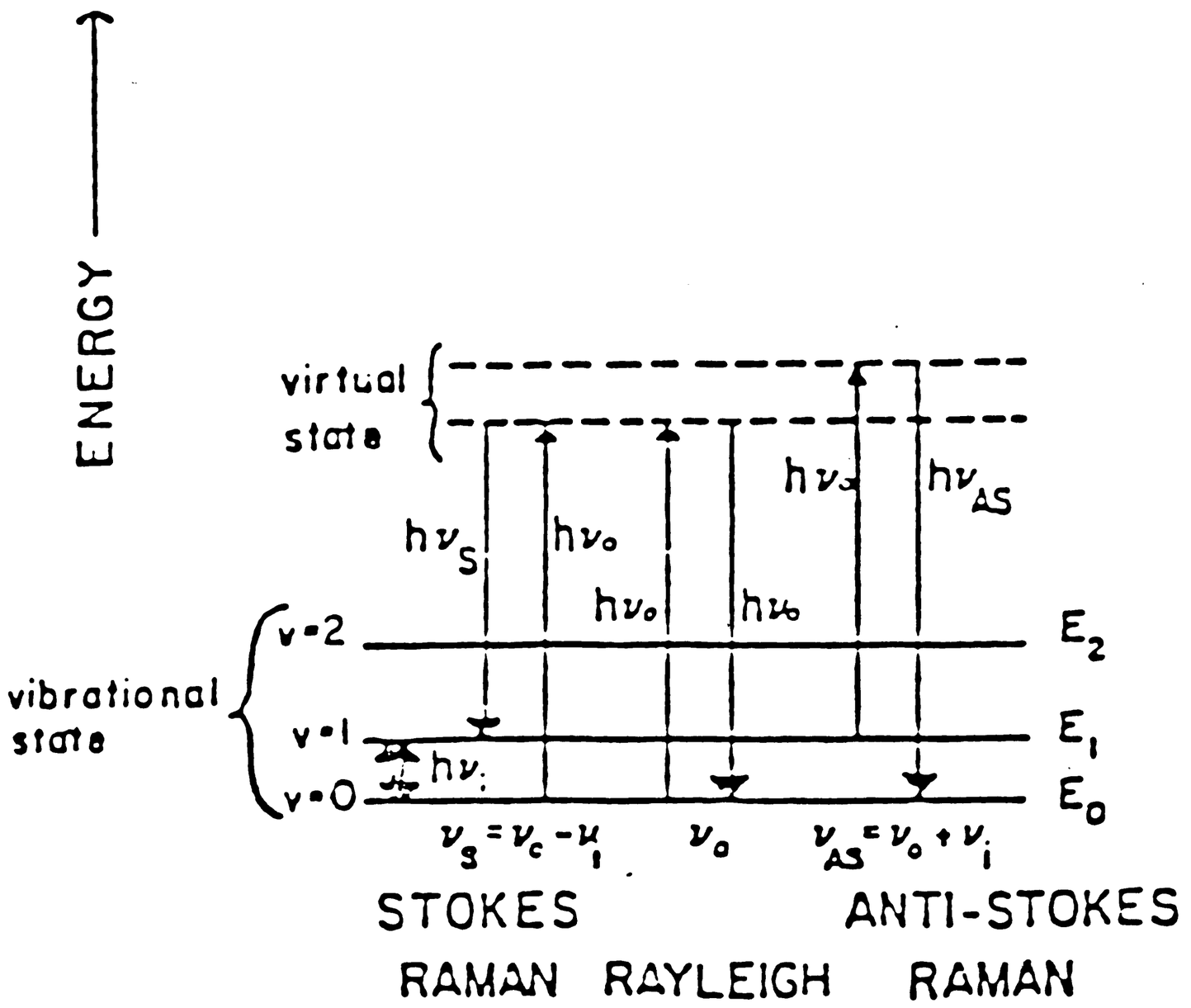

Figure 8. Diagram illustrating the vibrational Raman effect. Two electronic states with vibrational splittings are displayed. (After Etz[51])

The time dependent constant of proportionality α dictates how easily the electrons are displaced by the electric field and is known as the molecular polarizability.

For diatomic molecules, α varies linearly with bond length. At rest, the length of the bond between atoms comprising the molecule is designated as the equilibrium length Q_o. The associated polarizability is accordingly α_o. In the presence of the electrical field, the stretching and contracting motion of the oscillating molecule alters bond lengths, changing the polarizability as a function of displacement from the equilibrium bond length Q_o defined as Q_1, the displacement coordinate. ($Q_1 = 0$ at the equilibrium configuration Q_o). Thus, α varies as $\alpha_o + (\frac{\partial \alpha}{\partial Q_1})_o Q_1 + \ldots$ where $(\frac{\partial \delta}{\partial Q_1})_o$ indicates the rate of change of the polarizability with the change in bond length evaluated at the equilibrium configuration. Q_1 varies with time as the molecule vibrates with frequency ν_i so that $Q_1 = Q_1^o \cos(2\pi\nu_i t)$ where Q_1^o is the amplitude of the vibration or the maximum displacement from the equilibrium bond length Q_o.

The changing molecular polarizability as a result of its sensitivity to bond orientation (rotational transitions), length (vibrational transitions) or nature (electronic transitions) describes the Raman effect. Of these, the vibrational effect is most prominent and provides the chemical information. Polarization then is the key to the Raman phenomenon.

The magnitude of the rate of change in polarizability with respect to the change in bond length $(\frac{\partial \delta}{\partial Q})$ dictates the intensity of

the scattering process. In cases where a diatomic molecule stretches and contracts or bends symmetrically, i.e. when a molecule increases or decreases its occupied space and shape equally in all directions in a pulsating manner, the resulting alteration in the molecular polarizability yields the most intense Raman lines (Figure 9a). However, when the stretching or bending is unsymmetrical, the positive shift in polarizability in one direction cancels the negative shift in the other such that no scattering occurs and therefore no Raman effect results (Figure 9b).

Intensities of Raman lines are related to the fourth power of the excitation frequency (ν_o^4) and are directly proportional to the number density of the scattering molecules in a specific energy state E. This implies that intensity directly relates to the concentration of the species which generates the line. Therefore, quantification can be performed with standards,[52] however, it is necessary to obtain consistent intensity data such that comparisons can be made. This restriction requires that the geometry of the sample with respect to the excitation source and monochromator be reproducible from sample to sample since spectra can change with the direction in which the scattered light is viewed with respect to the plane polarized incident source.

A serious interference problem that occurs when the frequency of the excitation source approximately equals the quantized frequency of any excited levels is (electronic) fluorescence. This phenomenon occurs over a broad range of wave numbers in the Stokes region of the spectrum as a result of heating or photon absorption and appears as

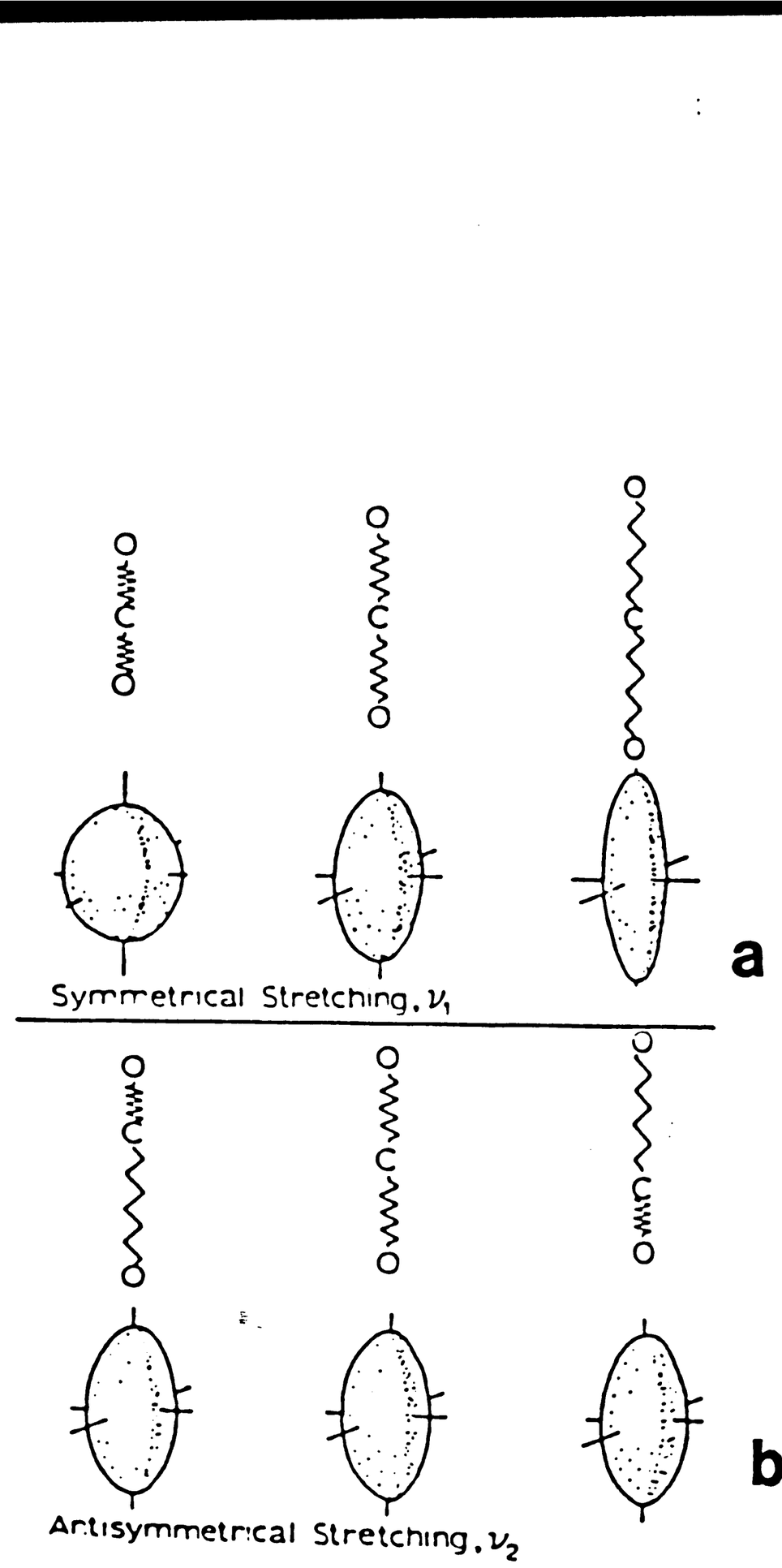

Figure 9. Polarizability ellipsoids for a linear molecule. a.) Symmetrical stretching (Raman active), and b.) Antisymmetrical stretching (Raman inactive).

emitted light with a frequency shifted from that of the incident light. This inelastic scattering process results when the incident energy E_o exactly equals the energy between two electronic levels, thus exciting the transition between the two levels as shown in Figure 10. Fluorescence does not depend on the excitation frequency ν_o and therefore, the artifacts it generates in the spectrum can be detected by changing the excitation frequency.

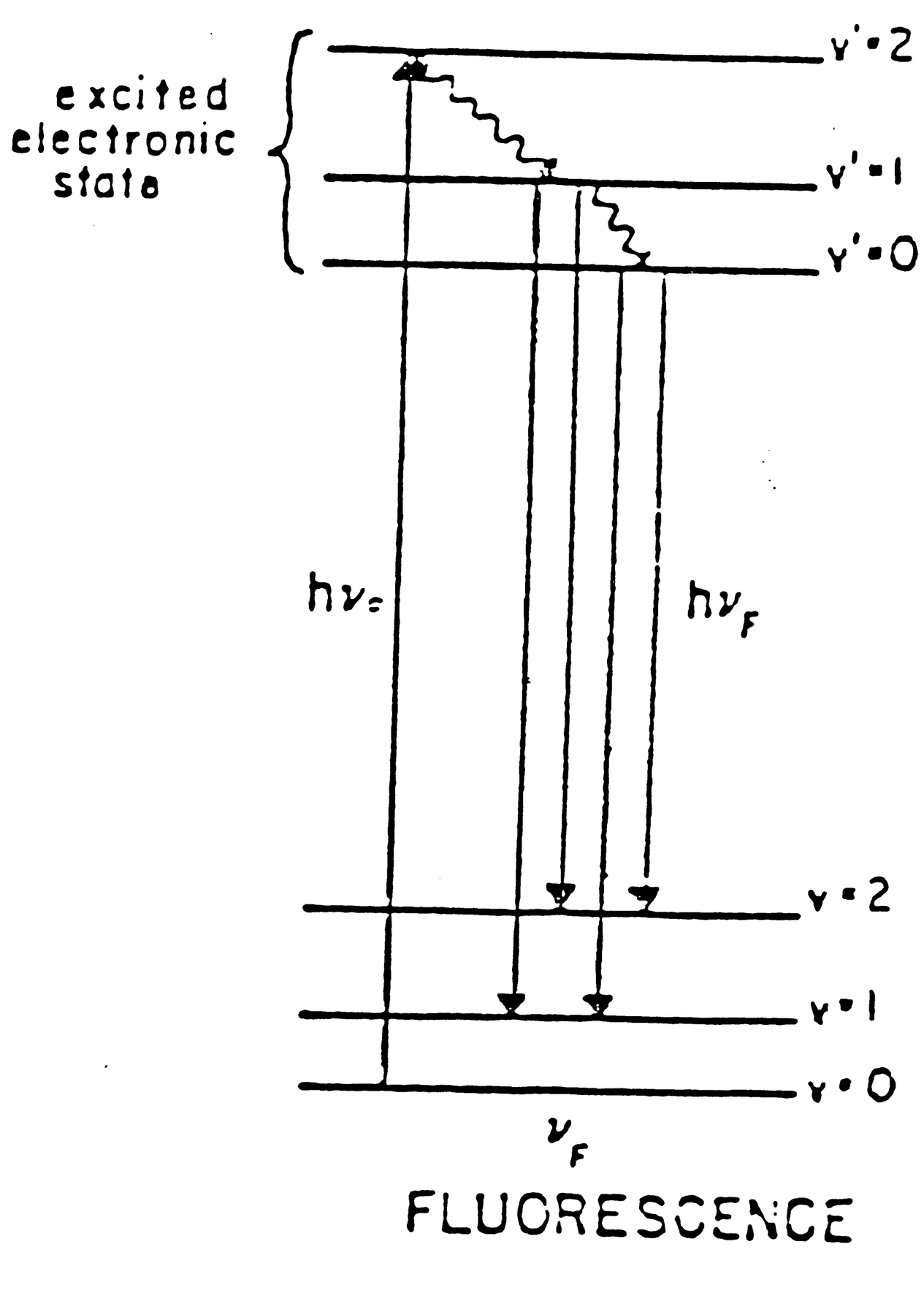

Figure 10. Diagram illustrating Raman flourescence effect (After Etz[51])

EXPERIMENTAL

Powder Preparation

The powders used for portions of this study were the oxides of yttrium and lanthanum (Molycorp Corporation) quoted as 99.99% pure. Table 1 shows the impurity concentrations in the two lots of powder as obtained by the mass spectroscopy technique. Both exhibit primarily other rare earth oxide impurities.

The co-precipitation technique was chosen to prepare the powder compositions of interest since this method allows an intimate mixing of the constituents on an atomic level. Because impurities introduced during the co-precipitation process can grossly affect sintering behavior, the choice of the precipitate was made on the basis of that which would yield a relatively clean product, free of detrimental ionic impurities that are difficult to remove by prefiring heat treatments. The oxalate co-precipitation process was chosen over the sulfate process in this work since the only ionic impurities resulting from the former precipitation procedure are hydrocarbon groups as opposed to sulfur in the latter process which has been shown to segregate to grain boundaries upon sintering, forming a wetting grain boundary phase.[42]

Teflon labware was used where possible throughout the powder processing procedure to avoid potential silicon contamination by glass apparatus. Furthermore, in an effort to reduce powder contamination possibilities, all labware utensils were thoroughly cleaned first with soap and water and then by acid washings in aqua-regia (HCl and HNO_3

Table 1. Impurity Concentrations for the Pure Oxides as Received from Vendor*

Analysis by Mass Spectroscopy
Concentrations in parts per million (ppm)

Y_2O_3 lot #1319		La_2O_3 lot #854	
loss on ignition**=0.46%		loss on ignition**=0.09	
La_2O_3	500	Y_2O_3	75
CeO_2	10	CeO_2	10
Pr_6O_{11}	1	Pr_6O_{11}	15
Nd_2O_3	2.3	$N_dO_2O_3$	15
Sm_2O_3	0.2	Sm_2O_3	30
Eu_2O_3	0.3	Eu_2O_3	30
Gd_2O_3	5	Gd_2O_3	300
Tb_4O_7	0.02	Tb_4O_7	75
Dy_2O_3	0.03	Dy_2O_3	75
Ho_2O_3	30	Ho_2O_3	30
Er_2O_3	7	Er_2O_3	30
Tm_2O_3	2	Ca	92
Yb_2O_3	5	Fe	0.9
Lu_2O_3	0.2	Mn	0.3
Ca	2.8	Cr	10
Fe	1.3	Ni	12
P	None	Zn	1
Mn	6	Pb	20
Cr	10	Sr	29
Ni	12	Ba	25
Zn	1.6	P_2O_5	23
Pb	20		
Mg	1.2		
Sr	6		

*Molycorp, Incorporated, Louviers, Colorado

**adsorbed CO_2, mostly H_2O

mixture), an HF solution, and finally a long time soak in boiling 18Ω deionized water.

A 0.9 Molar (approximately 80% saturated) oxalic acid solution was prepared from hydrated oxalic acid powder and deionized water and slowly heated to ensure complete dissolution of the contents. The pure oxides of yttrium and lanthanum were weighed in appropriate proportions and dry mixed in a one-liter teflon jar with a teflon rod. The mixture was enclosed with plastic tape and placed beneath a 100 ml burette filled with nitric acid and supported by a ring standard. The amount of nitric acid required for the conversion of the oxides to nitrates was obtained from the following chemical equation:

$$La_2O_3 + 6HNO_3 = 2\ La(NO_3)_3 + 3\ H_2O$$

$$Y_2O_3 + 6HNO_3 = 2\ Y(NO_3)_3 + 3H_2O$$

The total amount of nitric acid (HNO_3) was calculated from the requirements of both these reactions, and 50% excess HNO_3 was added to ensure nitrate formation.

The HNO_3 was added to the teflon jar very slowly since the reaction between the acid and the oxides is violent and extremely exothermic. Constant movement of the jar during the HNO_3 addition was performed to ensure as much of the oxides as possible contacted the acid. The large agglomerates that resulted were broken up with a teflon rod and then the contents of the enclosed jar were stirred with a teflon coated magnetic stirrer until a clear liquid was obtained.

Precipitation by oxalic acid incorporations to the nitrate solution was performed below room temperature (14-16°C) in the hopes of preventing particle coarsening in the liquid and also to ensure all

the nitrates came out of solution so as to obtain a high yield. The amount of oxalic acid needed was obtained from the following chemical reactions:

$$2La(NO_3)_3 + 3H_2C_2O_4 = La_2(C_2O_4)_3 + 6HNO_3$$

$$2Y(NO_3)_3 + 3H_2C_2O_4 = Y_2(C_2O_4) + 6HNO_3$$

Fifty percent excess oxalic acid was added in addition to the amount required. Oxalic acid was dripped from the burette at a rate of approximately 16 ml/minute into the agitated nitrate solution which was submerged in an ice bath maintained at 14-16°C. Because of the limited capacity of the burette, the process had to be interrupted periodically for acid refills, and adjustment of the stirring was necessary as the process continued to achieve sufficient agitation with increasing volumes of solution.

The precipitates which formed after the oxalic acid addition were allowed to settle for a short time (∿1 minute) after which the liquid was drawn off and stored. The thick oxalate slurry was then filtered through a 0.2μm polycarbonate mesh and was followed by the liquid. The filtrate was placed into a second teflon jar and washed three times with 18Ω deionized water, each rinse being immediately followed by a filtration step. The washed precipitate was then hand mixed to break up agglomerates and allowed to dry for 7 to 8 hours under a heat lamp.

Calcination to the oxides was performed at 1000°C in a box furnace. The dried oxalate powder, contained in a closed Al_2O_3 crucible was taken to temperature over a 1½ to 2 hour time period, held at 1000°C for 1 hour, and cooled to below 300°C before being

transferred for storage to a nitrogen atmosphere containing glove box. Final powder characterization was performed by x-ray diffractometry using a one degree per minute scan rate between 15° and 65°. Further analyses involved examination on the ETEC scanning electron microscope using a Au-Pd coating to prevent electron charging.

Sample Preparation for 30 mol% La_2O_3/Y_2O_3 Mixtures

Cold Pressing and Heat Treatment

Two grams of the calcined powder were crushed to break down agglomerates and placed within a three-quarter inch diameter graphite die assembly consisting of four graphite spacers and a punch rod (Ultracarbon, Union Carbide Ltd., <100 ppm impurities). Pieces of weighing paper were placed within the die in an effort to reduce contact between the oxide mixtures with the graphite spacers and rod. Pressure was applied slowly over a three to five minute interval, steadily increasing the force to 3000 lbs. (47 MPa) before slowly releasing it and extracting the pellets. Removal of the carbon which contaminated the sides of the pellets as they contacted the graphite walls was achieved by heating the pressed pellets enclosed in an Al_2O_3 crucible in a box furnace for two hours. Green densities were then measured.

Pellets of thirty mol percent La_2O_3/Y_2O_3 powder mixtures that were sintered and heat treated in this study were packed with powder of the same composition to help prevent vaporization of the Y_2O_3-La_2O_3 from the sample.[53-55] The entire mass was enclosed in a covered tungsten crucible which was placed in the hot zone of a tungsten mesh resistance heated furnace (Contorr Associate Inc., Suncook, New

Hampshire). An argon atmosphere was maintained in the evacuated chamber with a flow rate of approximately one SCFH air. Accurate temperature measurement at the container wall in the hot zone was achieved by focusing a high temperature optical pyrometer on the crucible . Quenching was performed by programming the furnace controller unit to decrease temperature from the heat treating setpoint (2025°-2050°C) to room temperature in 1 minute (i.e. essentially cutting the power off) while the rod supporting the crucible was rapidly withdrawn from the hot zone into a jet stream of argon entering at the bottom of the furnace chamber. Cooling rates exceeded 400°C/minute. All sintered densities were obtained by the Archimedes method (Appendix I).

Microscopy

Thin Foil Preparation

Thin foils were prepared by slicing 30 mil thick cross sections of the sintered pellet and mounting them on glass slides for grinding and polishing. Samples were rough ground with 600 grit and then 1200 grit SiC powder until thicknesses less than 100 μm were achieved and then they were polished on both sides with 6 μm diamond paste. Polished foils were mounted between two rhodium plated copper grids and ion beam thinned at 6 kV. A light carbon coating was applied to the thin foils to avoid charging under the electron beam. All TEM analyses were done at 120 kV on a Philips 400T equipped with a Tracor Northern EDS.

k-Factor Determination

For the k-factor determination in this system, a homogeneous

Y_2O_3-9 mol%La_2O_3 sample was prepared by GTE Laboratories (Waltham, MA) in the following manner:

a) sintered at 2150°C for 90 minutes

b) cooled to room temperature

c) annealed at 1950°C for 6 hours to homogenize the sample.

Wet chemistry analysis by the inductively coupled plasma (ICP) technique was performed to yield the concentrations of yttrium and lanthanum metal, and microprobe analyses on the bulk using the sample as its own standard confirmed the homogeneity of the sample within the limits of resolution of the instrument. K-factor measurements were performed on thin foils in both the TEM and STEM modes at 120 kV.

A window approximately 1.2 times the full width half maximum of the lanthanum L peak (the element present in smaller amounts) was established and x-ray counting continued for each analysis point until 100,000 counts were obtained within the window region. This was done to minimize any errors due to poor counting statistics yielding a 3σ error of 1%.

Intensities for the Y^L and La^L peaks were ratioed after performing a background subtraction and with the known concentrations of each element (C_Y, C_{La}) in the foil as obtained from the wet chemistry analysis, the k-factor was determined according to the familiar Cliff-Lorimer relation:

$$\frac{C_Y}{C_{La}} = k_{YLa} \frac{I_Y}{I_{La}}$$

Errors for the k-factor were calculated by the student t analysis in the 95% confidence limit.

Precipitation Sequence Study - 9 mol% La_2O_3 Samples

An experiment was designed to study the nature of the precipitation process in the two phase cubic and hexagonal field. Nine mol percent samples were sintered* in the single phase cubic region at 1950°C for 3 hours and were up quenched into the two phase field and held at 2100°C for the following times: 1 minute, 10 minutes, 30 minutes, 300 minutes. The same procedure was followed for a second set of samples, only these were held at 2200°C for the same amounts of time. All treatments were followed by quenches to room temperature.

Laser Raman Microprobe

A pellet of pure Y_2O_3 powder was pressed and analyzed on the laser Raman microprobe. Analyses were performed with both the 4879.8 A wavelength of the blue laser argon source and the 5145.5 A wavelength of the green laser argon source, and scanning proceeded from ∿70 (100) to 1800 wave numbers with a scan speed of 5 x 10 cm/minute.

*Nine mol% samples courtesy of W. H. Rhodes, GTE Laboratories, Waltham, MA.

RESULTS AND DISCUSSION

Powder Preparation

The powder preparation procedure outlined in this work concentrated on obtaining sinterable, compositionally accurate, and intimately mixed Y_2O_3/La_2O_3 constituents. Many of the studies that have been performed on co-precipitation of rare earth oxides by the oxalate process have focussed on the effects of precipitation temperature and calcining temperature on the particle size, packing, and sintered density. Therefore, before the procedure outlined in the experimental section was chosen, three temperatures of precipitation were studied in order to detect any major effects on powder morphology and/or sintering characteristics.

Precipitations were performed for 30/70 mol% La_2O_3/Y_2O_3 mixtures at 14°C, 25°C (room temperature) and 70°C and the precipitates were allowed to remain for 1 hour in the solution at temperature before filtration. All calcinations were conducted at 1000°C for one hour.

Figure 11 shows high magnification SEM micrographs of the calcined powders for each of the precipitation temperatures. The soft agglomerates shown are comprised of smaller rod like powder aggregates approximately 3 to 4 microns in size for each of the samples. A BET analysis on the individual, deflocculated aggregates is required for more accurate particle size assessment.

The powders were pressed at 12000 psi (83 MPa) and fired in a nitrogen atmosphere at 1750°C for 5½ hours. Figures 12, 13 and 14 show low and high magnification SEM pictures of polished sections of each of the sintered pellets, etched with a 20% HCl solution. The

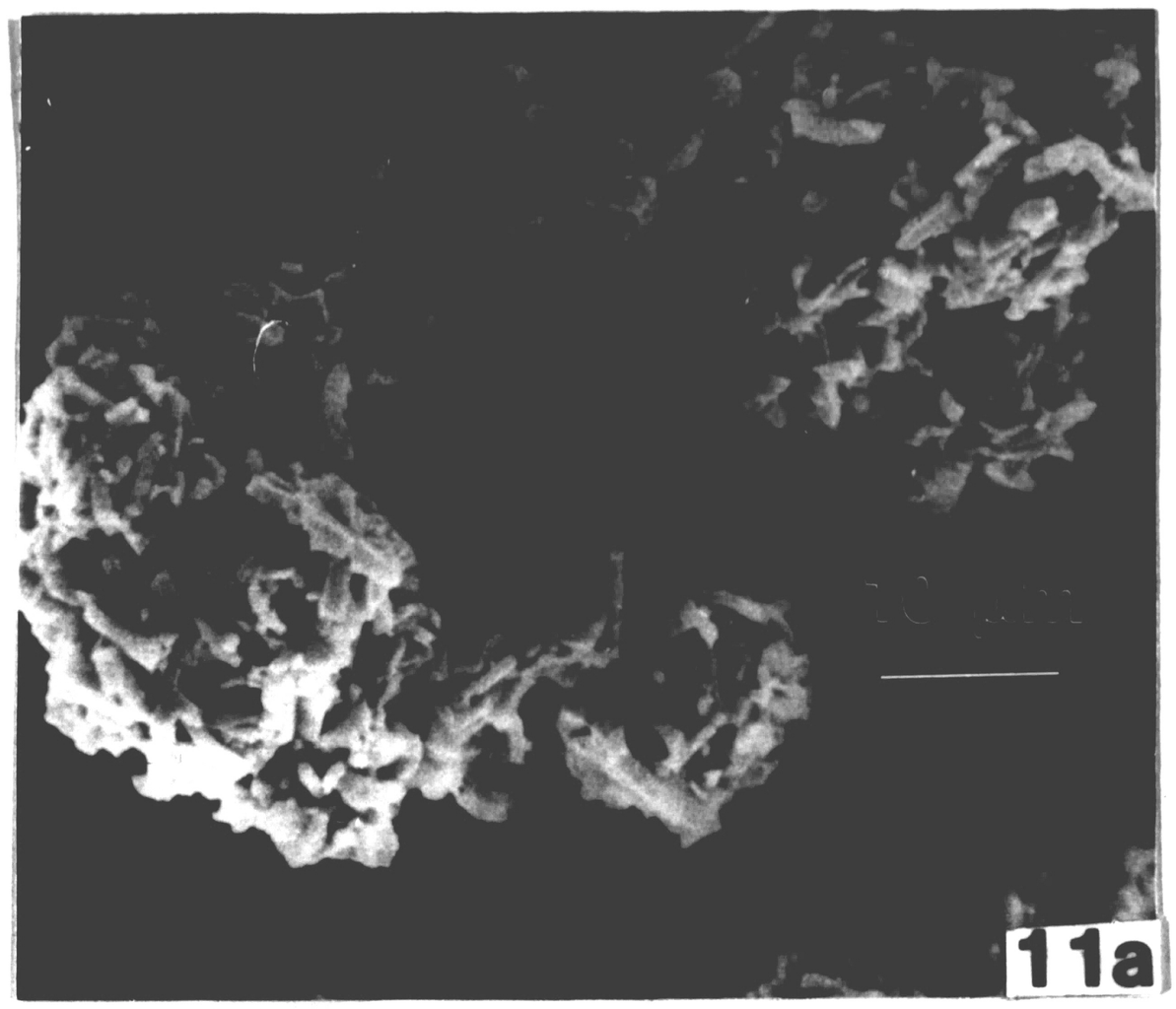

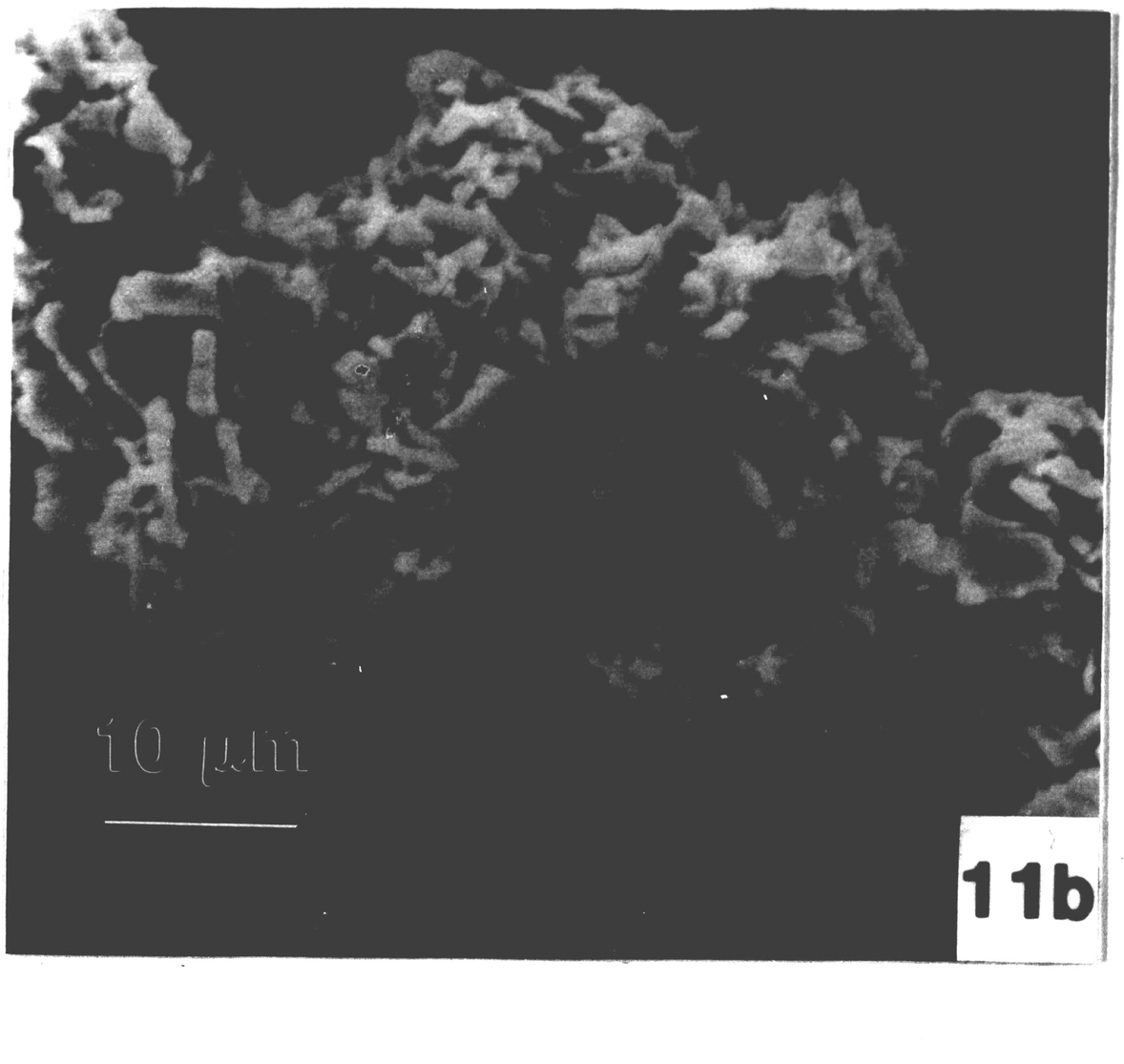

Figure 11. SEM micrographs of calcined Y_2O_3 - 30 mol% La_2O_3 powder coprecipitated at a.) 14°C, b.) 25°C, and c.)70°C.

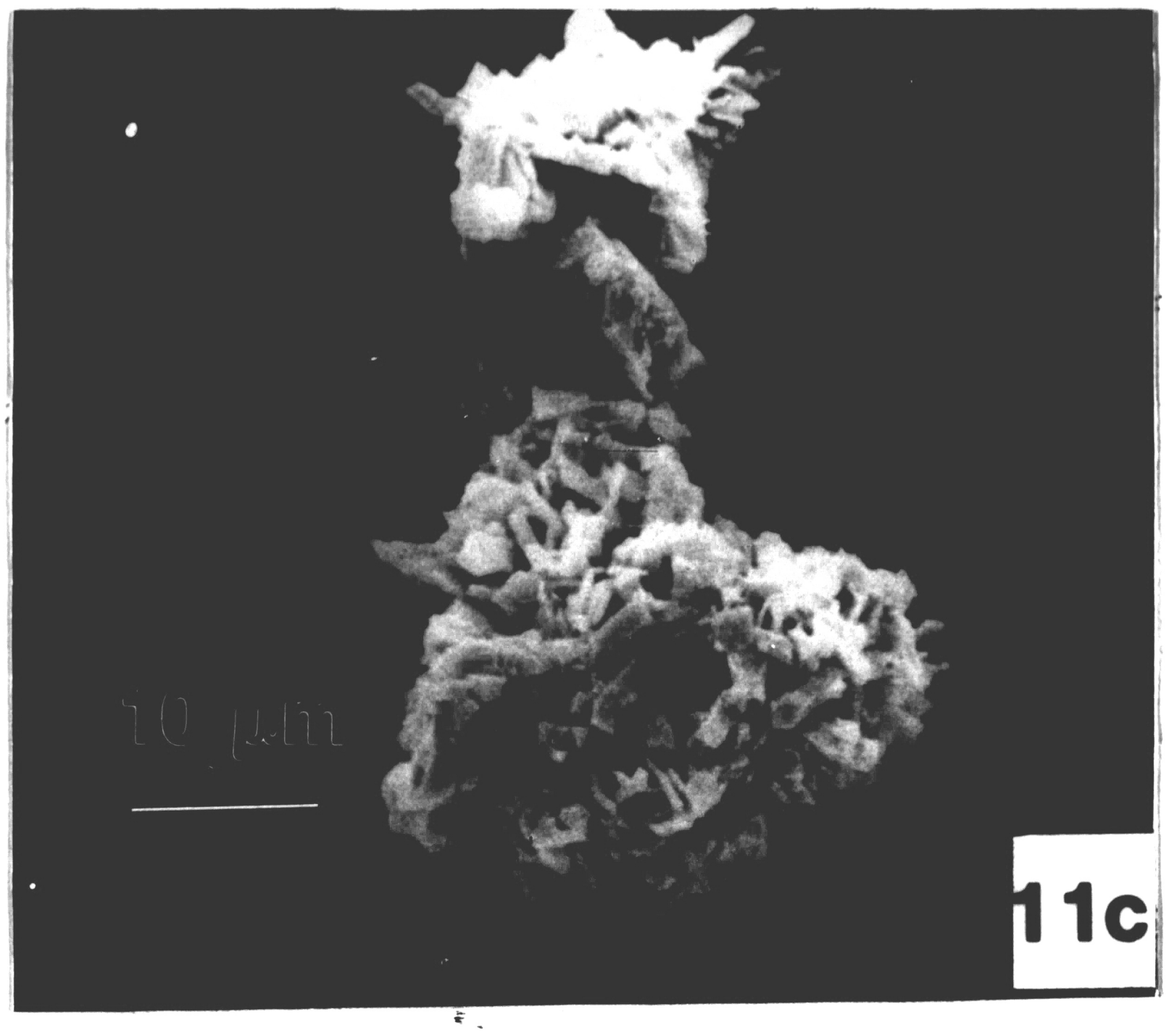
10 µm
11c

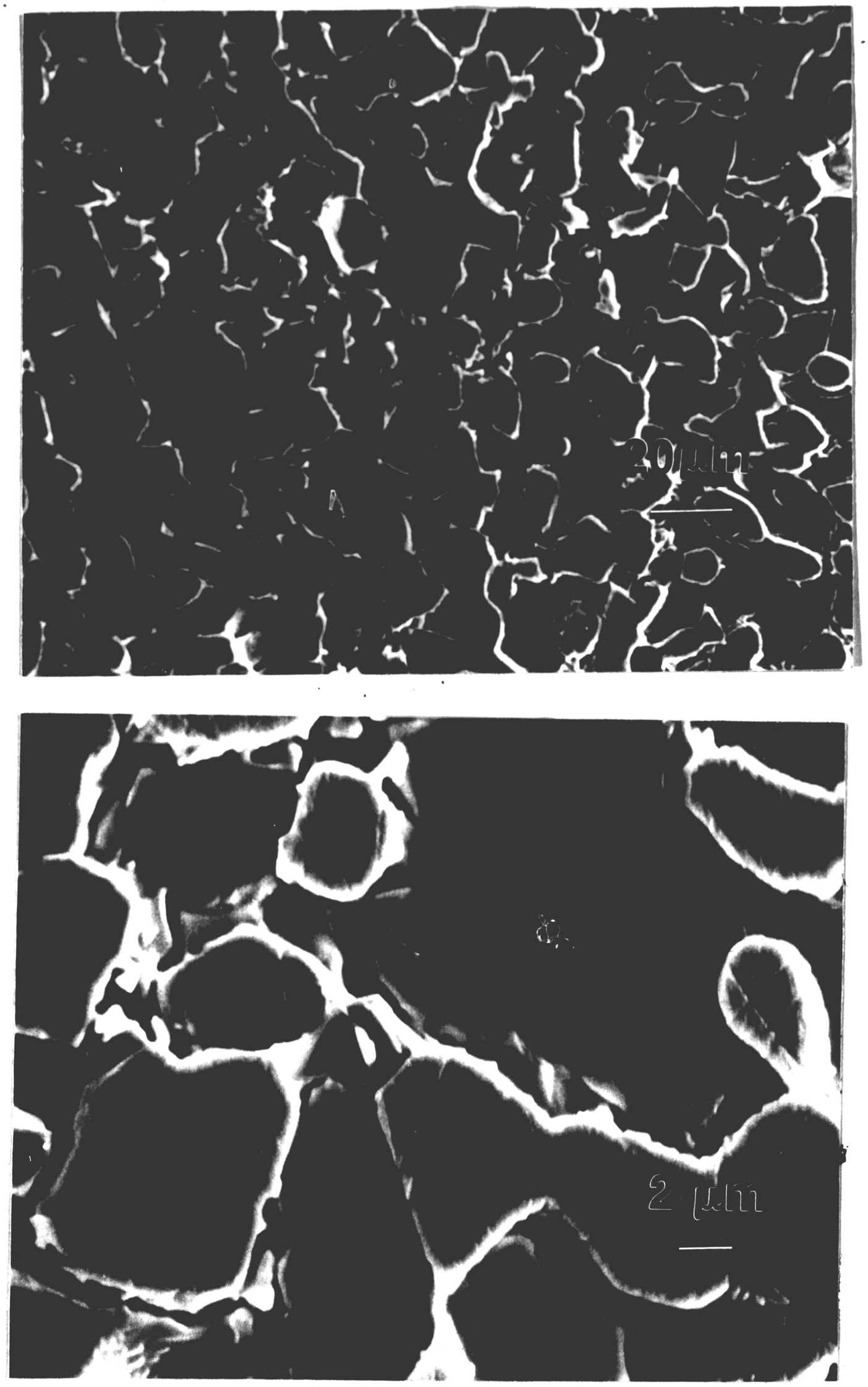

Figure 12. Low and high magnification SEM micrographs of polished and acid etched surface of sample sintered 1750°C for 5.5 hours from powders precipitated at 14°C.

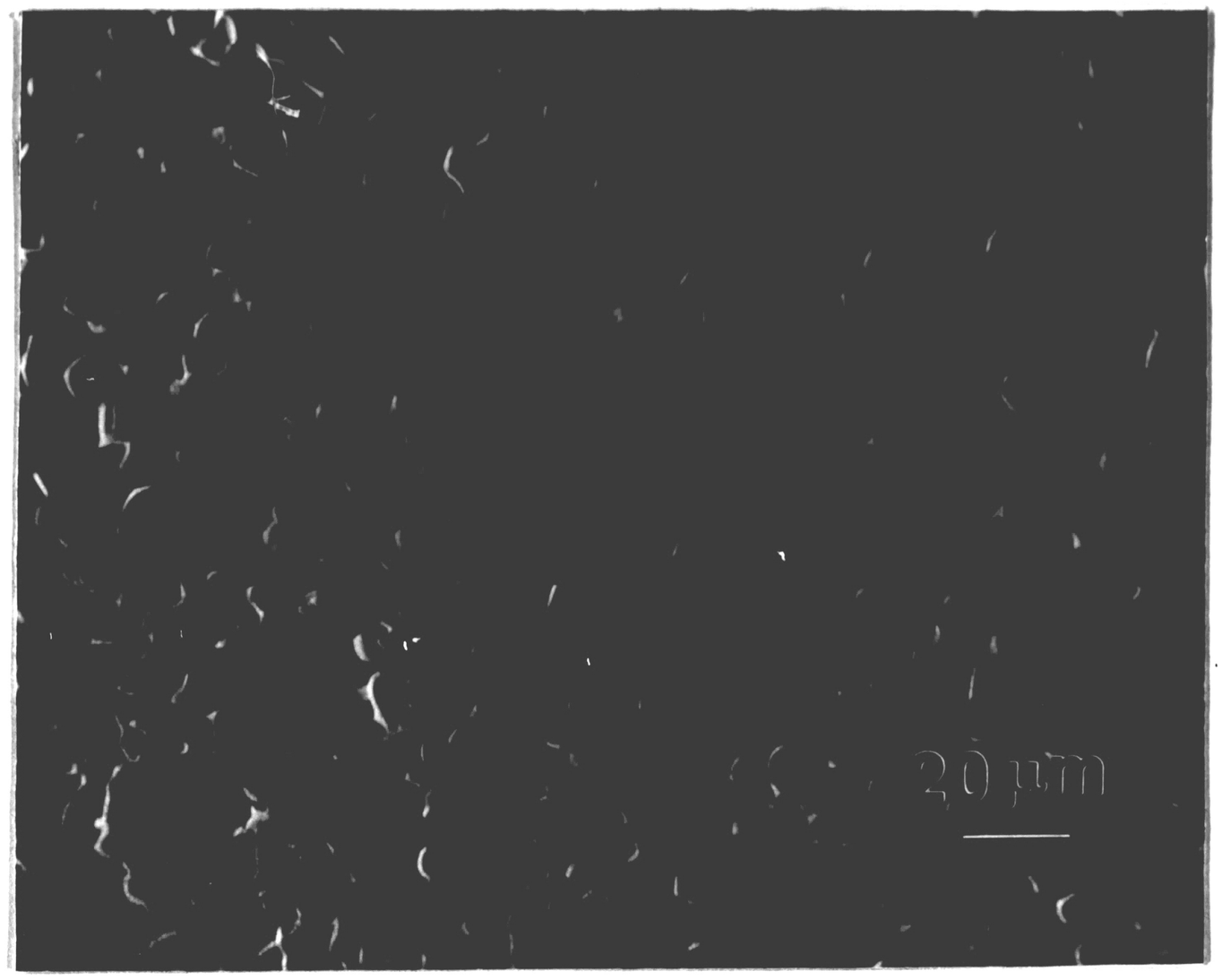

Figure 13. Low and high magnification SEM micrographs of polished and acid etched surface of sample sintered 1750°C for 5.5 hours from powders precipitated at 25°C.

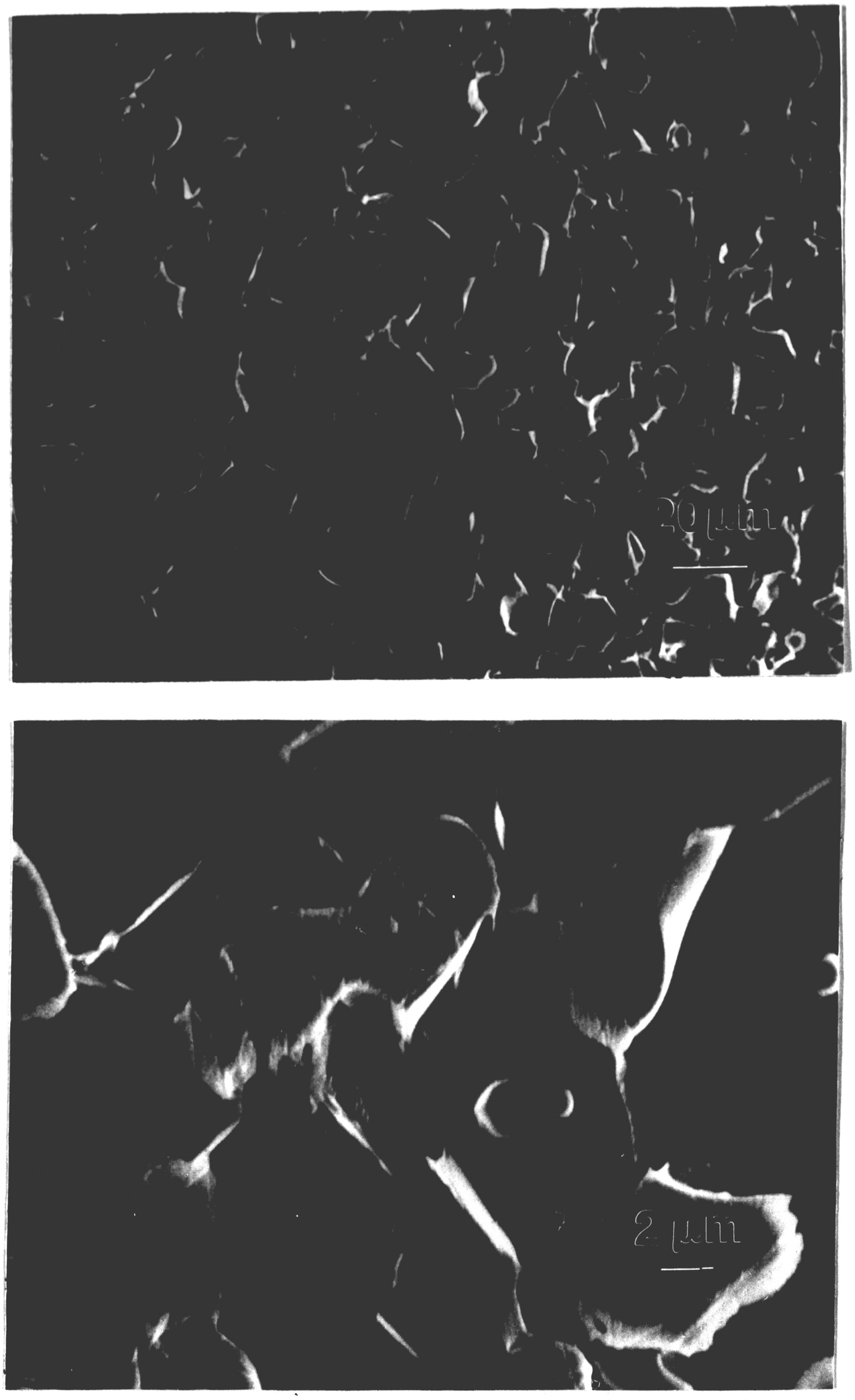

Figure 14. Low and high magnification SEM micrographs of polished and acid etched surface of sample sintered 1750°c for 5.5 hours from powders precipitated at 70°C.

topography of the samples results from the severe, preferential attack by the acid solution on the two phase mixture present as these samples were sintered in the cubic (low La_2O_3 content) and monoclinic (high La_2O_3 content) phase field of the diagram. Grain sizes approximate to 10 microns or more for the three samples.

The green and sintered densities are displayed in Table 2. As can be seen, the precipitating temperature does not appear to affect the compactibility and fired densities. Results obtained by Reetz et al.[34] show gradual increases in green densities and significant reductions in sintered densities (1700°C) with increasing precipitation temperatures up to 80°C due to the increase in particle size with increasing temperature. They showed, however, that green densities only show significant changes for low calcination temperatures and change very little for calcination temperatures above 900°C while sintered densities remain independent of calcining temperature. Therefore, the crude method of green density measurement used in the present investigation may not have been precise enough to show the slight changes, if any, in the green density for powders calcined at 1000°C or perhaps the coarsening effects of the higher calcining temperatures are sufficient to counter any benefits obtained from low precipitating temperatures.

Although the precipitation temperature showed no major observable effects on powder size, compactibility, and sintered densities, the initial oxalate precursor, although not systematically studied, may have shown some gross dependencies. It may be, however, that these dependencies of the oxalate size on precipitating temperature become

Table 2. Density Data for 30 mol% La_2O_3/Y_2O_3 Mixtures Coprecipitated at Three Different Temperatures, Pressed, and Fired at 1750°C for 5½ Hours

	Co-precipitating Temperature	Density (% theoretical) Green	Sintered
Sample 1	25°C	39.7	99.8
Sample 2	14°C	39.0	99.6
Sample 3	70°C	39.68	99.8

lost during calcination due to the nature of the decomposition process which is believed to involve an exothermic reaction of CO and O_2 to form CO_2.[56] CO_2 gas which becomes entrapped within the powder can result in a breakdown of the powder when released. This powder cracking which is recognized by a popping or cracking noise during the calcination, was observed in this study and has been proposed by other investigators to aid in the increase of powder particle surface area.[40] It thus appears that although the temperature of precipitation may determine the agglomerate size, the temperature of calcination is probably very critical in determining the final size of the individual particles.

As no differences could be observed among the three samples with respect to sintered density, the 14°C preparation was chosen merely because the lower temperature aids in bringing the constituents out of solution[57] helping to insure yields. The x-ray powder diffraction results of powders precipitated at 14°C and calcined one hour at 1000°C are shown in Figure 15. The slight differences in the d-spacings for corresponding peaks in the observed data with the JCPDS standards of the C-type polymorph of Y_2O_3 indicate that the sample is a solid solution of La_2O_3 in cubic Y_2O_3. The La^{+3} ion (1.14A), being much larger than the Y^{+3} ion (0.91A) results in an increase in the cell parameter. For the (400) peak shown, the lattice parameter can be obtained for pure Y_2O_3 as follows:

$$a_o = 4(d_{400}) = 4(2.652) = 10.604$$

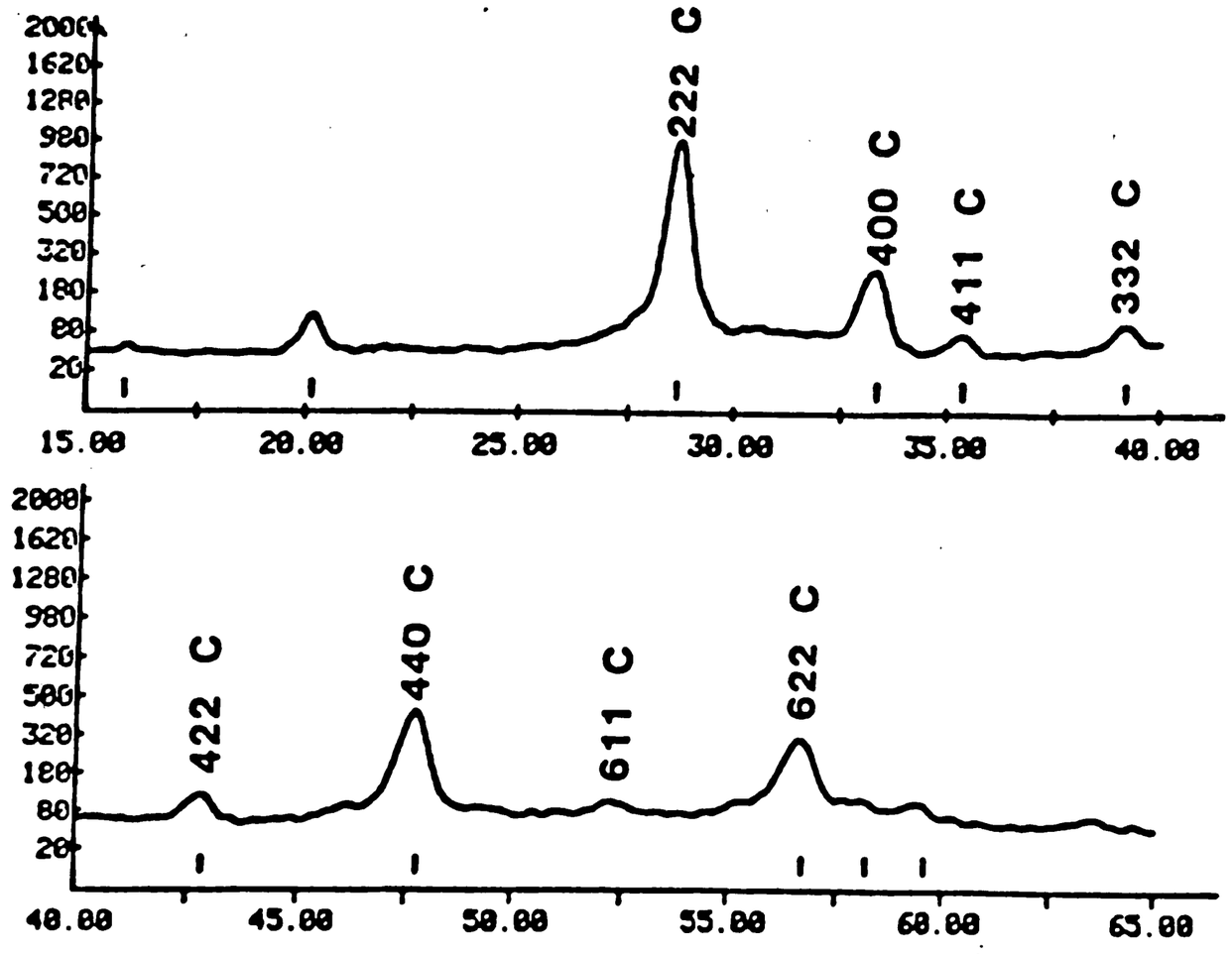

X -RAY DIFFRACTION DATA

30 MOL % La2O3/Y2O3 POWDER

2-THETA (DEG)	WIDTH (APPROX)	COUNTS PEAK	COUNTS BKGND	D (ANG)	I (NORM)
20.13	0.51	110.	41.	4.4121	9.05
28.63	0.76	1218.	49.	3.1184	100.00
30.46	0.40	53.	49.	2.9346	4.38
33.37	0.44	256.	49.	2.6854	21.02
35.43	0.56	49.	49.	2.5338	4.02
39.16	0.40	56.	48.	2.3004	4.62
41.84	0.59	25.	50.	2.1990	2.05
42.88	0.52	83.	52.	2.1088	6.80
47.93	0.37	408.	66.	1.8979	33.50
52.38	0.87	46.	71.	1.7468	3.80
56.98	0.68	256.	67.	1.6181	21.02

11 PEAKS IDENTIFIED 11 CRYSTALLINE 0 AMORPHOUS
11 PEAKS LISTED

Figure 15. Results of x-ray powder diffraction analysis on coprecipitated Y_2O_3 - La_2O_3 powders showing the correlations to the cubic (C) crystal structure

With 30 mol% La_2O_3 in solid solution, d_{400} is determined by x-ray diffraction to be 2.6854. Thus, the lattice parameter a_o becomes 4 x 2.6854 or 10.7416--approximately a 1.3% increase.

Finally, three separate lots of powder, all precipitated at 14°C and calcined at 1000°C for one hour were analyzed by the inductively coupled plasma (ICP) technique to assess the compositional accuracy of the constituents. Results are shown in Table 3. Lots one and two were only tested for La_2O_3 while lot 3 was tested for both Y_2O_3 and La_2O_3. The initial 30/70 mol ratio of La_2O_3 to Y_2O_3 for the dry mixed oxides is maintained after dissolution, coprecipitating, washing, drying, and calcining back to the oxides. Thus, the oxalate coprecipitation procedure used in this work yields sinterable solid solution powders of precisely predetermined compositions.

Electron Microscopy

k-Factor

The k-factor for the analytical electron microscopy study of the Y_2O_3-La_2O_3 system was experimentally measured on thin foils of nine mol% La_2O_3/Y_2O_3 solid solution material. These samples, fabricated by GTE Laboratories (Waltham, MA) were chemically analyzed by the ICP technique to determine the concentrations of yttrium and lanthanum metal. The analyses revealed lanthanum concentrations of 11.63 weight percent and yttrium concentrations of 68.01 weight percent for a total of 9.87 mol% La_2O_3.

The bulk specimen was tested for homogeneity on the electron microprobe (JEOL 733). Typical x-ray maps for the yttrium and the lanthanum metal taken from various regions of the bulk show the

Table 3. Analysis of Three Powder Lots Prepared by the Oxalate Coprecipitation Method for 30 mol% La_2O_3/Y_2O_3 Mixtures

(results obtained by the Inductively Coupled Plasma Technique)

	Lot #1	Lot #2	Lot #3
mol% La_2O_3	30.8	31.6	30.45
mol% Y_2O_3			69.55

distributions of the respective elements (Figure 16). The darker circular areas present near the center of the micrographs is attributed to an artifact of the instrument rather than a feature of the sample as these appeared consistently in the same region of the picture regardless of the area of the sample from which the x-ray map was photographed. Approximately 60 probe analyses were performed on the bulk using the sample as its own standard and measuring oxygen by difference. Average values of the metal contents were determined as 71.29 (±4%) weight percent yttrium and 11.10 (±.5%) weight percent lanthanum in close agreement with the wet chemistry analysis.

K-factor measurements were performed in both the TEM and STEM modes on thin foils prepared from the bulk. Measured values obtained after dividing observed x-ray intensity ratios of the two elements by their concentration ratio in the foil (as determined by wet chemistry) ranged from 0.54 to 0.58 for both the TEM and STEM modes. Values were then tested on the 9 mol% standard to determine which yielded compositions closest to that of the ICP analysis, and that value was then employed. In this work, all chemical analyses were performed in STEM mode using a k-factor of 0.54±2%.

During the course of the k-factor determination, some inconsistency was observed in the intensity ratios obtained which resulted in erroneous k-factor measurements. X-ray counting was performed for each analysis point until a total of 100,000 counts were obtained in the smallest (La) peak, however, at times, wide variations of the I_Y/I_{La} ratio occurred depending upon the thin foil and the area of analysis. This may be a direct result of: a) absorption by the

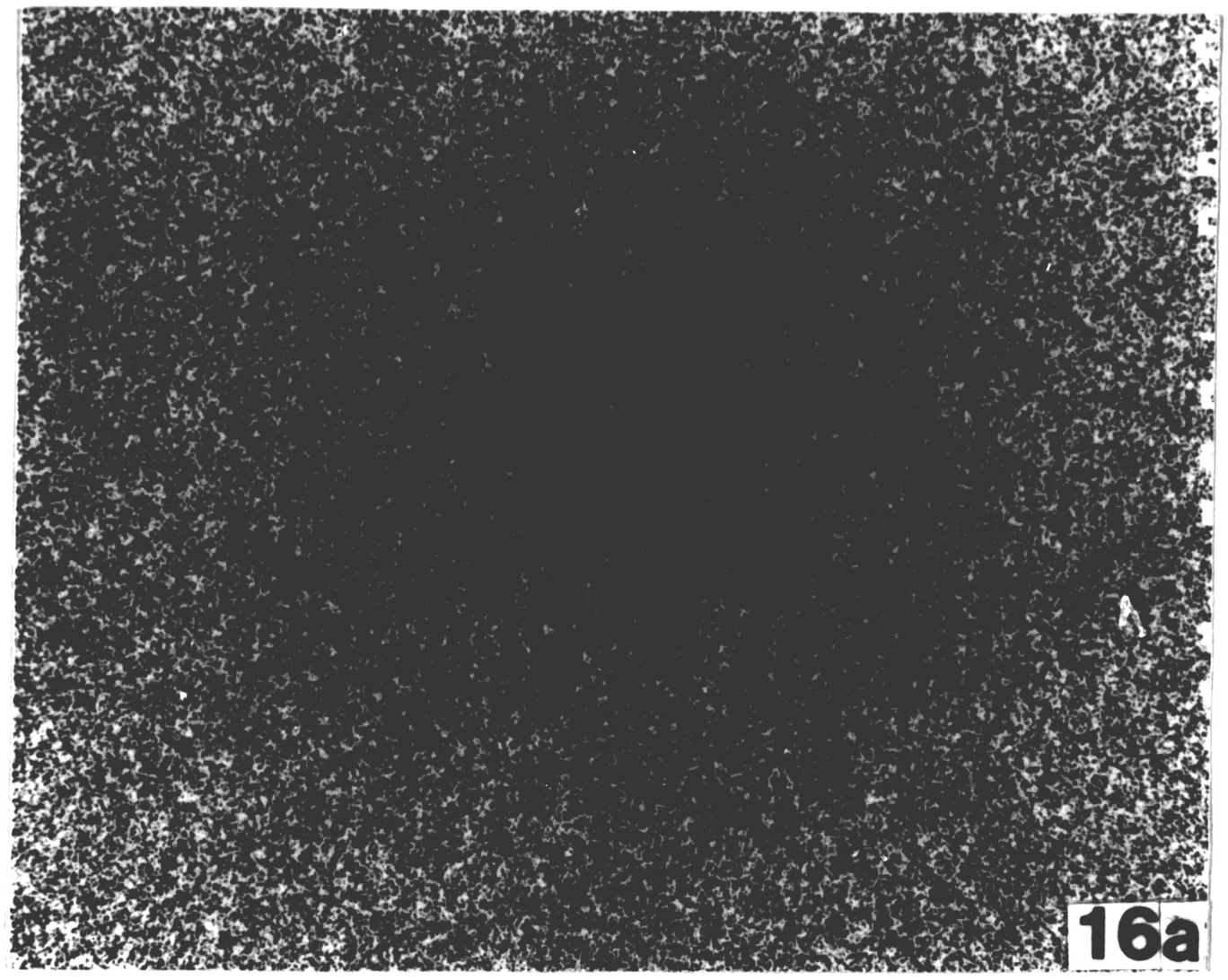

Figure 16.) X-ray maps of 9 mol% La_2O_3/Y_2O_3 standard used for k-factor determination. Light areas exhibit distributions of a.) yttrium and b.) lanthanum respectively.

sample due to the breakdown of the thin film criterion; b) electron beam damage to the foil, or c) contamination. Each of these possibilities was investigated.

For nine mol% La_2O_3/Y_2O_3 samples, the 10% thin film criterion limit indicates a critical thickness of approximately 2000Å beyond which a correction factor must be applied to the Cliff-Lorimer relation to account for absorption of x-rays by the sample (Appendix 2). The low energy yttrium L X-rays are the ones most easily absorbed by the sample in the present case. In the isolated instances where the I_Y/I_{La} ratio was found to be considerably different than the average, it was always less than and never greater than the average value indicating a yttrium deficiency. However, STEM analyses were always recorded on foil edges in thin regions of the sample using a spot size and condenser two aperture large enough to achieve a dead time of 20% or less, and thickness measurements obtained by convergent beam diffraction from some of the analysis areas revealed foil thicknesses below that of the critical limit. Therefore absorption by the sample was ruled out as a cause of the inconsistent intensity ratios.

Electron beam damage to the foil was also studied. Some elements exhibit an instability under the electron beam as they become removed by the incident electrons. Lanthanum and yttrium are rather heavy elements, and are unlikely to be affected by the beam. However, in an attempt to attain 100000 counts in the La^L peak the beam was held stationary on the same area for times that were as long as eighty minutes in some cases. In order to assess the sample stability as a function of counting time, counts were collected in a series of 100

second intervals from a thin portion of the foil and the intensity data of both the yttrium and lanthanum peaks were recorded after each interval. After 15 minutes (nine 100 second intervals), the ratioed intensities I_Y/I_{La} were plotted against the amount of time the beam was held stationary on the sample. Figure 17 shows the results of this analysis. The straight line fit to the data with zero slope indicate that for counting times as long as 15 minutes, no sample degradation was detected.

Carbon contamination buildup in the vicinity of the stationary beam during the long counting times may result in an absorption of x-rays, thereby causing the intensity inconsistencies. However, no contamination spots were observed on the thin foil after the analysis in most cases. Also, the results of the beam damage study should testify to the possible absorption by carbon contaminants as the sample was subjected to potential contaminants for an extended period of time. Nevertheless, contamination of a different form has been determined to be the reason for the anomalies observed in some of the data collected.

Silicon contamination was found to be present on some of the samples. At times, the amount of silicon was significant enough to result in a ring pattern superimposed on the selected area diffraction pattern obtained from a region of the foil on which the silicon lay. This contaminant appeared in the EDS display during microanalysis as well, but due to the relative energies of the peaks studied, its detection wasn't always easily recognized.

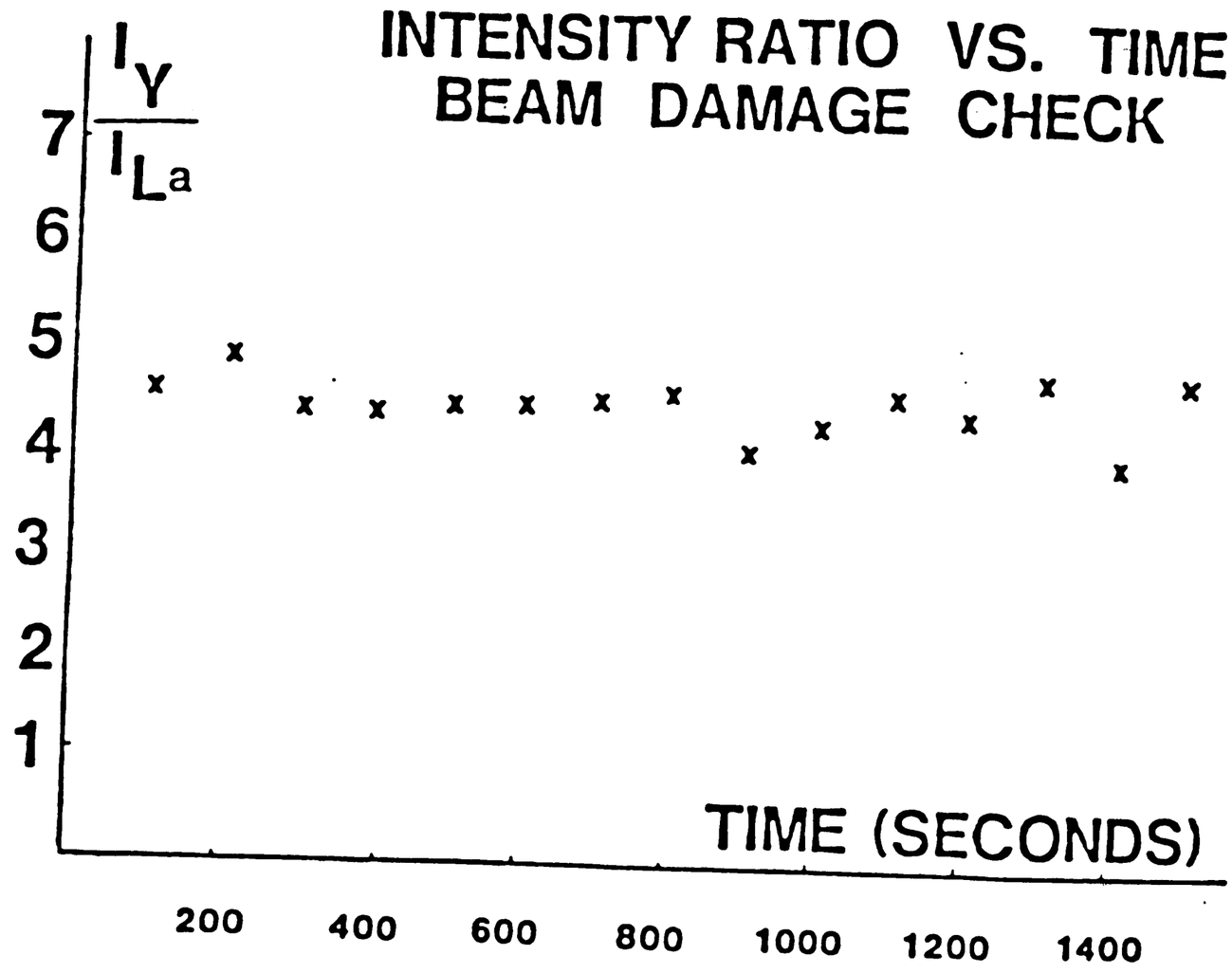

Figure 17. Plot of the ratio of the yttrium to lanthanum intensities versus time of exposure to electron beam.

The silicon K peak lies at the lower energy end of the spectrum (1.84 keV), partially overlapping the yttrium L peak on its lower energy side. By nature, the Y^L peak always exhibits a "tail" or a region of raised background on its lower energy side which diminishes with decreasing energies from the main Y^L peak. The silicon K peak can be confused as part of this tail region. However, in cases where contamination becomes significant or when extended count times are used, the overlap of the Si^K and Y^L peaks produces an extremely sharp shoulder on the low energy side of the Y^L peak which raises the background much above normal. This, in conjunction with silicon's large mass absorption coefficient for Y^L x-rays (μ/ρ = 3000) yields poor background fits of the data to the standard and erroneous intensity ratios.

Silicon contamination thus proves to be a serious threat to reliable quantitative STEM analyses in the Y_2O_3-La_2O_3 system and in other Y_2O_3 containing ceramics as well since silicon is a common contaminant present in many powders as a consequence of the powder processing route. The problem can be alleviated by utilizing the Y^K line in the quantitative analysis for which the silicon mass absorption coefficient is much lower ($\sim$11) or by determining and eliminating the cause of contamination in the sample.

In the present investigation, silicon contamination was traced to the ion beam thinner which uses a silicon based pump oil that can vaporize and condense on the sample when the sample remains in the thinner too long after the beams shut off. Cold trapping and/or switching to a hydrocarbon based oil can avoid sample contamination.

Successful removal of the silicon can be performed by ion milling the sample a short period of time before immediately removing it from the thinner.

Precipitation Sequence - Nine mol% La_2O_3/Y_2O_3 Samples

Previous work on precipitation and transformations involving the hexagonal polymorph in 9 mol% La_2O_3/Y_2O_3 samples focussed on attempts at quenching in the hexagonal second phase from sintering temperatures in the two phase cubic and hexagonal field. An experiment was designed to investigate the nature of the hexagonal phase precipitation process in the two phase field. The sintered 9 mol% La_2O_3/Y_2O_3 specimens used in this study were annealed in the cubic and hexagonal field for various amounts of time and quenched to room temperature. Results of the TEM/AEM examinations follow.

Figures 19 through 23 show microstructures obtained for samples annealed at 2100°C. In general, the 2100°C series is characterized predominantly by grain boundary precipitation as shown by the back-scattered electron microprobe micrograph (Figure 18) for the sample annealed for 300 minutes. According to the phase diagram, nine mol% La_2O_3 samples annealed at 2100°C lie close to the cubic/cubic and hexagonal phase boundary, not very far into the two phase region. As a result, the driving force for homogenous nucleation in the grain is relatively weak and heterogeneous nucleation on the grain boundary can be expected. It is this heterogeneous boundary nucleation that is most likely responsible for grain boundary pinning during the transient second phase sintering technique described earlier.

Figure 18. Backscattered electron micrograph of polished section of 9 mol % La_2O_3/Y_2O_3 sample annealed 300 min. at 2100°C showing distribution of the second phase.

After one minute at 2100°C, the precipitates are nucleated on the grain boundaries as regularly shaped La_2O_3 rich particles approximately 1 micron in size (Figure 19). Figure 20, although not a typical micrograph for the sample annealed ten minutes at 2100°C, merits attention in that it exhibits strain contrast along the grain boundary indicating the initial stages of the precipitation process. For anneals longer than ten minutes, the grain boundary phase appears as elongated structures as evidenced by the dark field micrograph for the thirty minute heat treatment (Figure 21) and the micrographs for the sample annealed 300 minutes (Figures 22a-b).

The second phase in the 300 minute sample exhibits a substructure of twins and has an overall facetted appearance. TEM studies performed on the hexagonal and monoclinic polymorphs of other rare earth oxide systems yielded similar observations of twin structures.[27-29] Strained interfaces can also be noted in the bright field photos of Figures 22 and 23 between both the facetted regions or sections within the second phase (22a) as well as between the second phase itself and the cubic matrix (22b). Previous results by GTE on samples quenched to room temperature after six hours at this temperature have shown that the hexagonal phase rapidly transforms to monoclinic symmetry in a manner accompanied by twinning and slip. Therefore, since the second phase in the sample annealed 300 minutes at 2100°C contains twins it is believed to be monoclinic.

The sectioning of the second phase or its partitioned nature which yields its facetted appearance may be a direct result of the the hexagonal to monoclinic transformation. As mentioned previously in

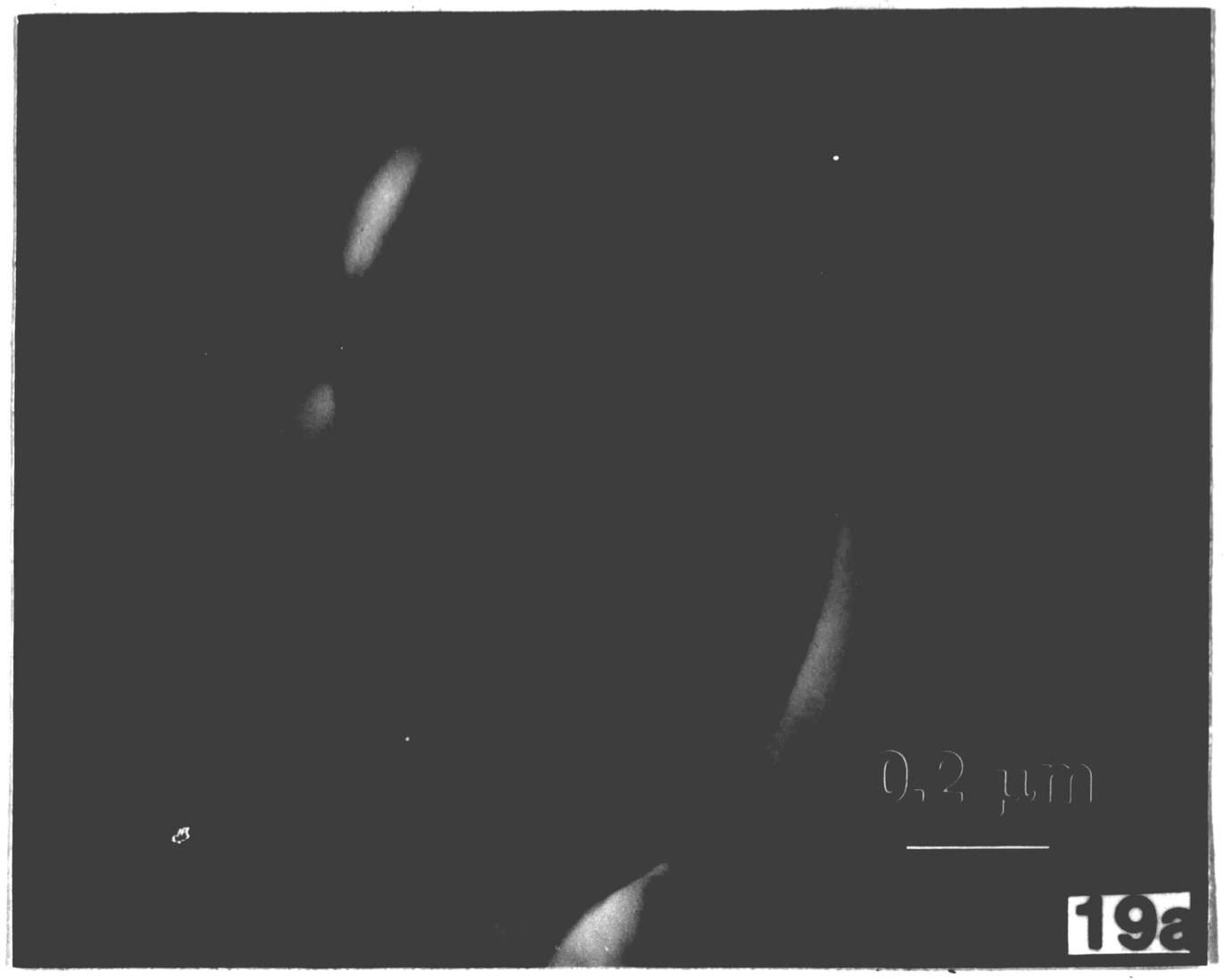

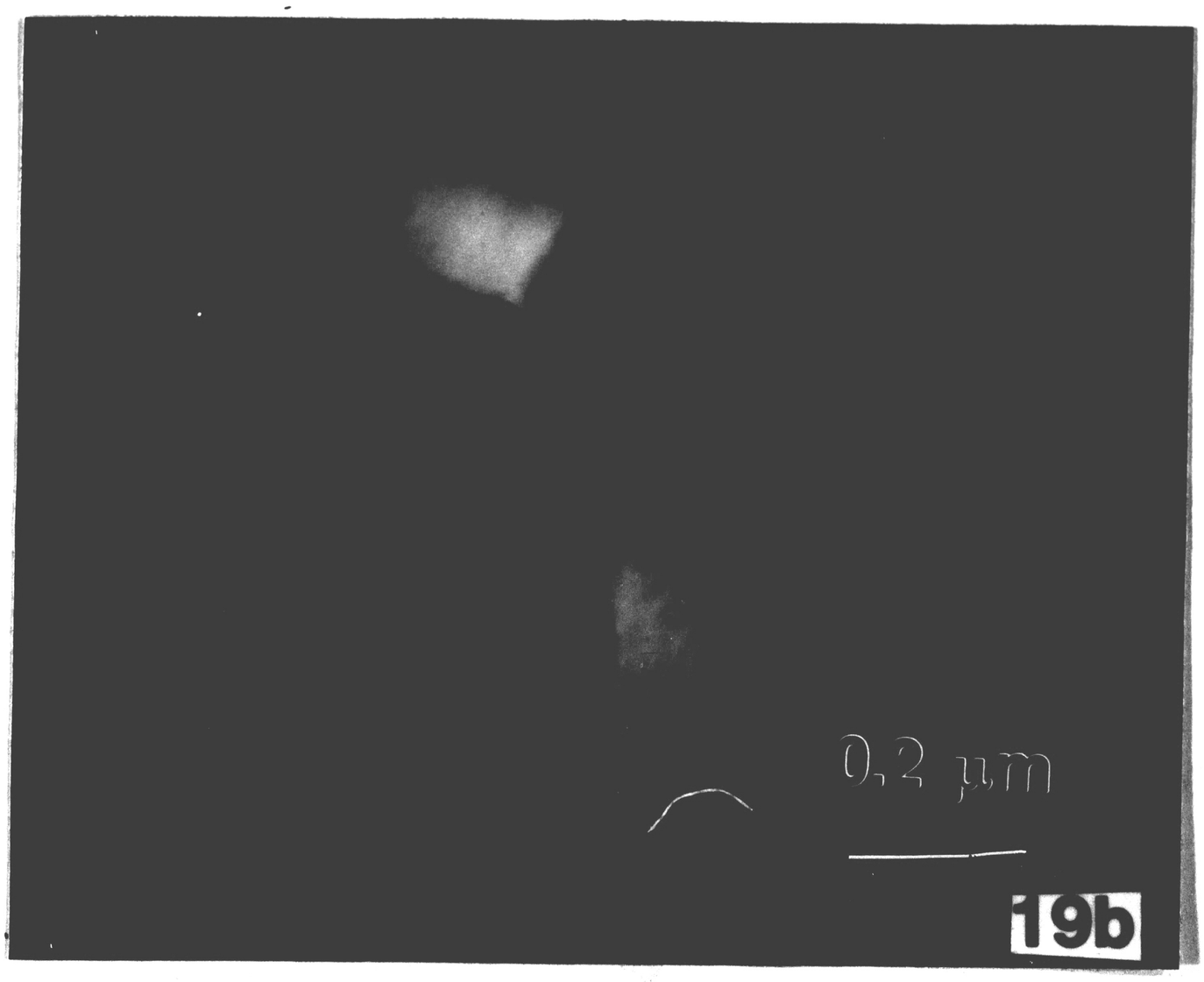

Figure 19 a,b. TEM bright field micrographs of La_2O_3 rich grain boundary precipitates in 9 mol % La_2O_3/Y_2O_3 samples quenched after 1 min. at 2100°C.

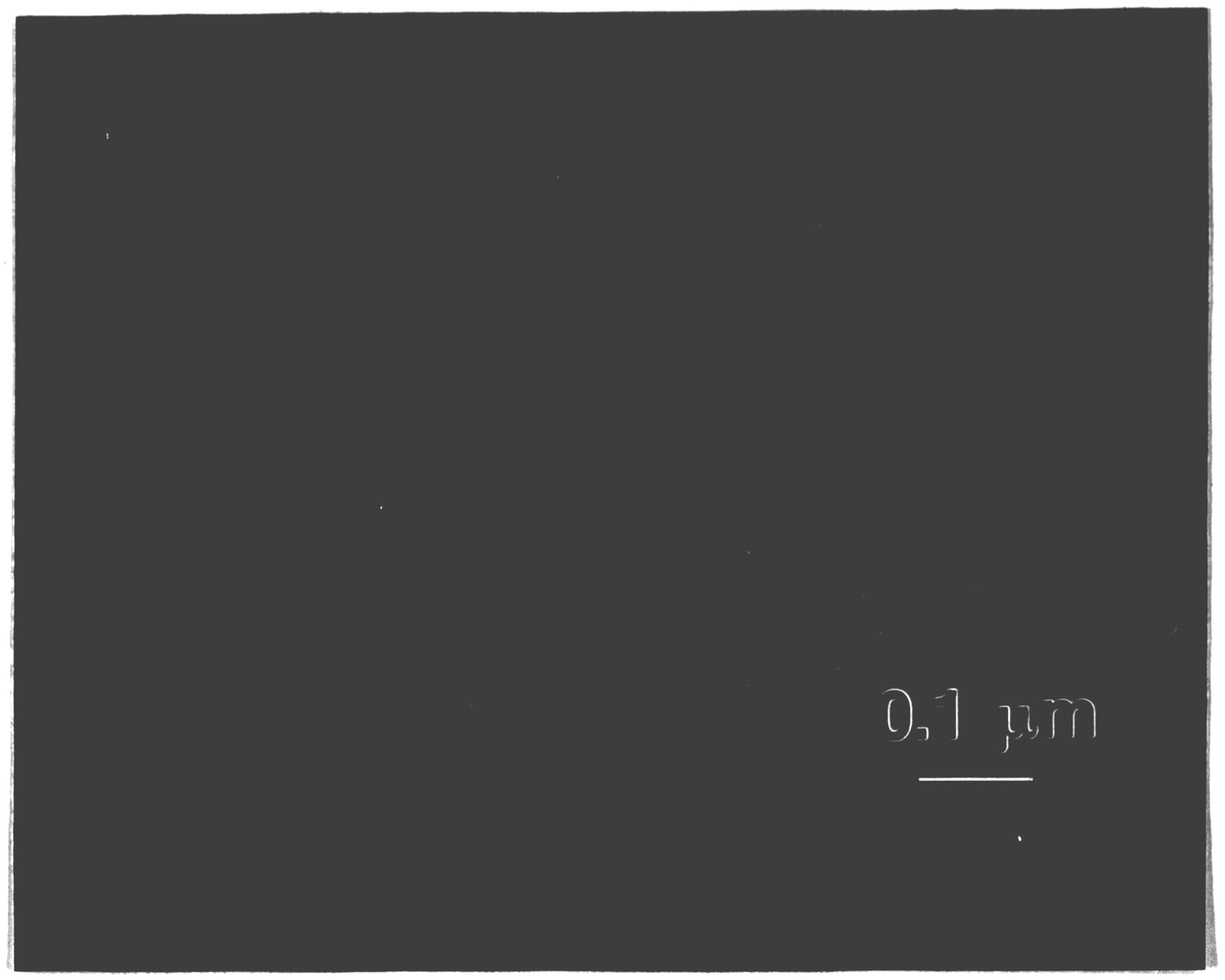

Figure 20. TEM brightfield micrograph exhibiting grain boundary strain contrast indicating the initial stages of precipitation in a 9 mol% La_2O_3 sample annealed 10 min. at 2100°C.

RETAKE

The Operator has Determined that the Previous Frame is Unacceptable and Has Refilmed the Page in the Next Frame.

Figure 20. TEM brightfield micrograph exhibiting grain boundary strain contrast indicating the initial stages of precipitation in a 9 mol% La_2O_3 sample annealed 10 min. at 2100°C.

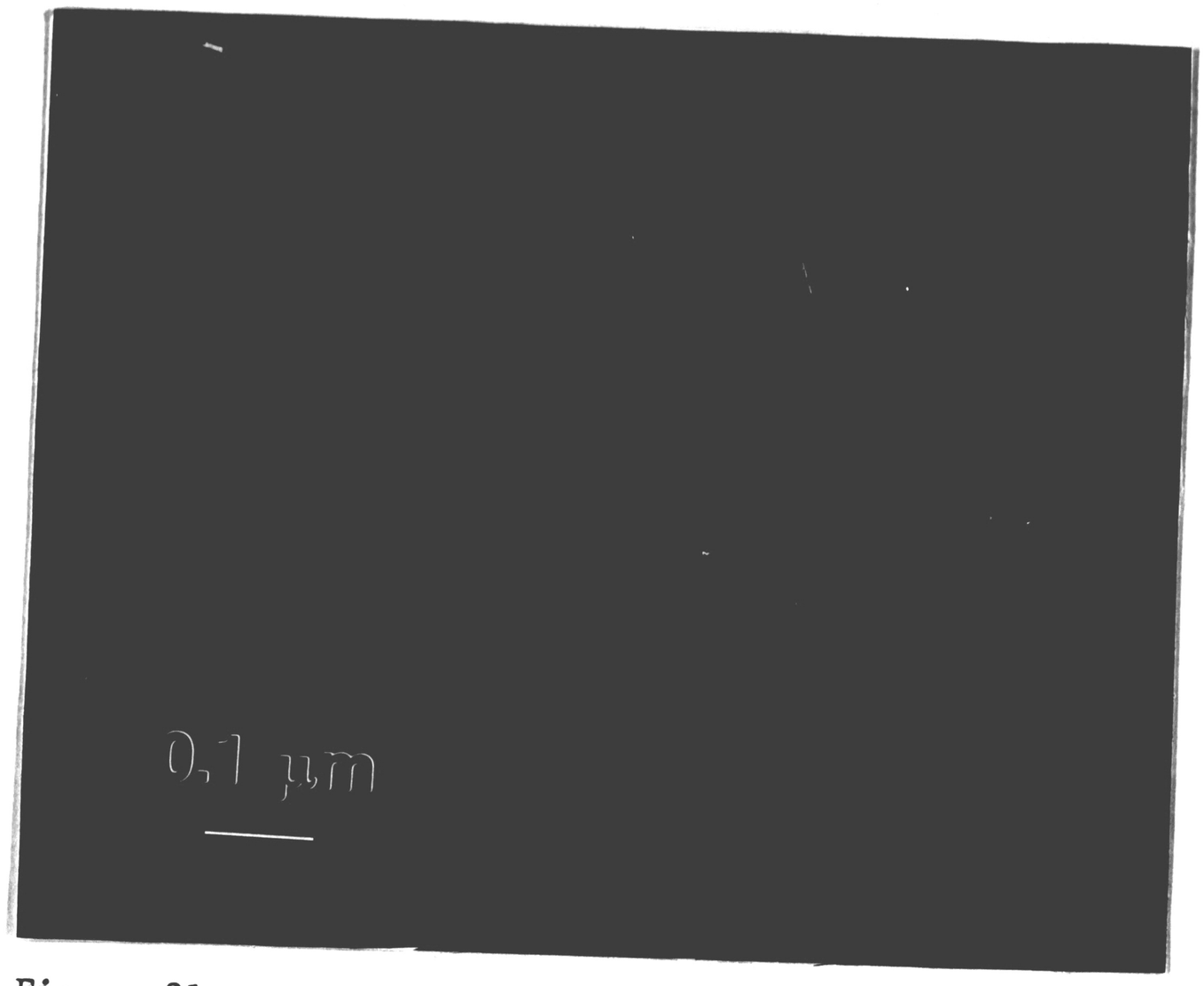

Figure 21. Dark field micrograph of elongated grain boundary precipitate for sample annealed 30 min. at 2100°C.

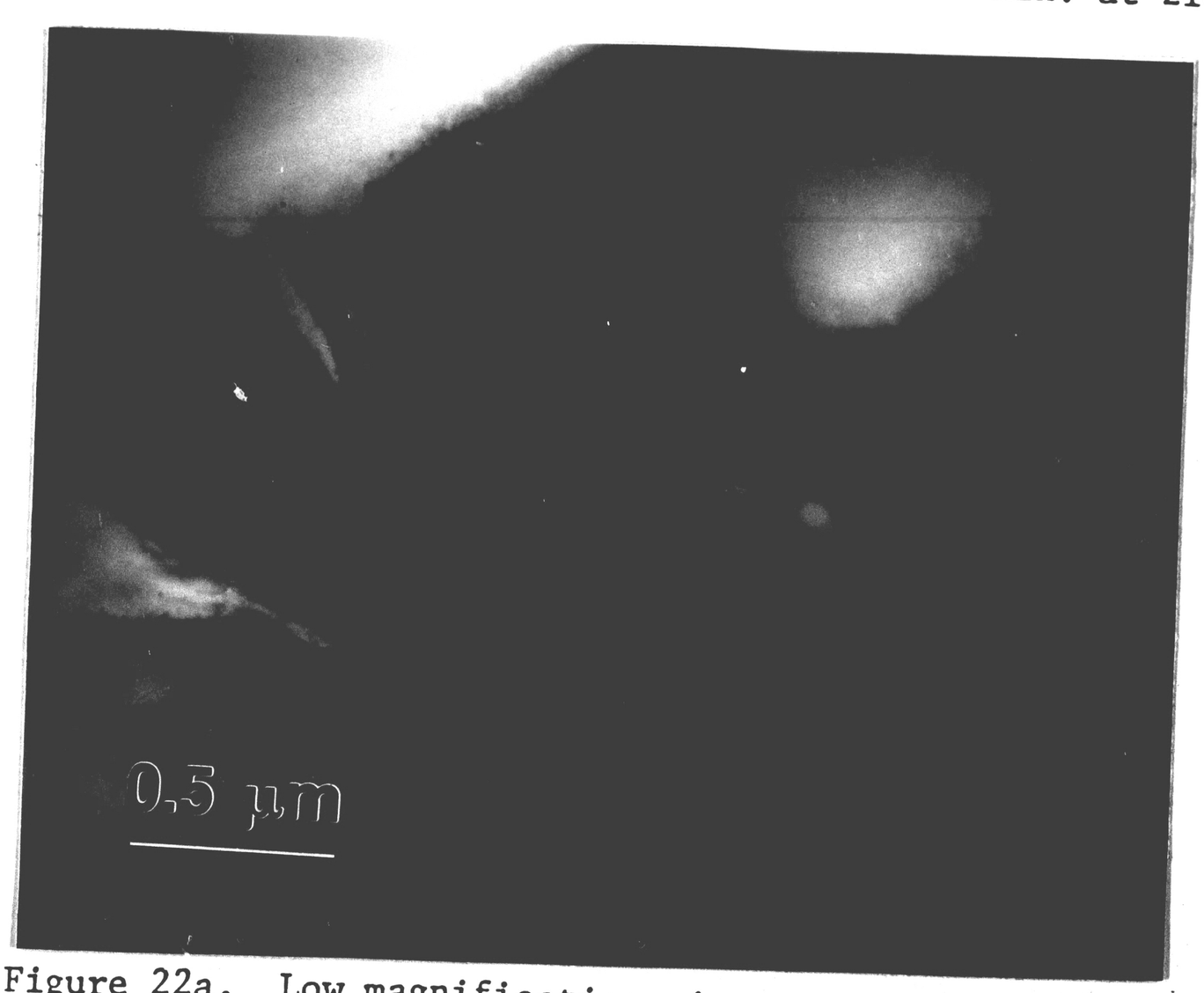

Figure 22a. Low magnification picture of elongated precipitate showing strain and twin substructures after 300 min. at 2100°C.

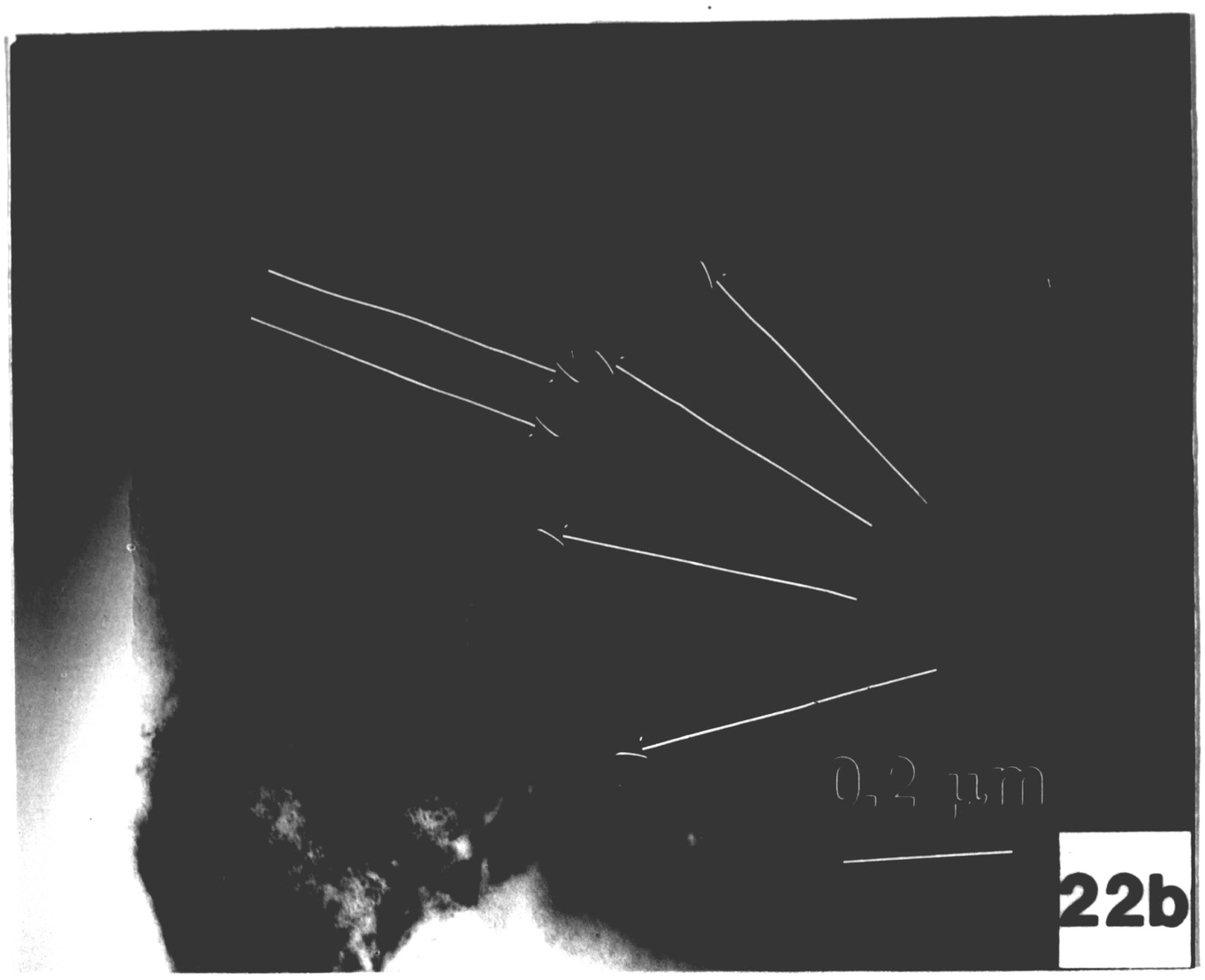

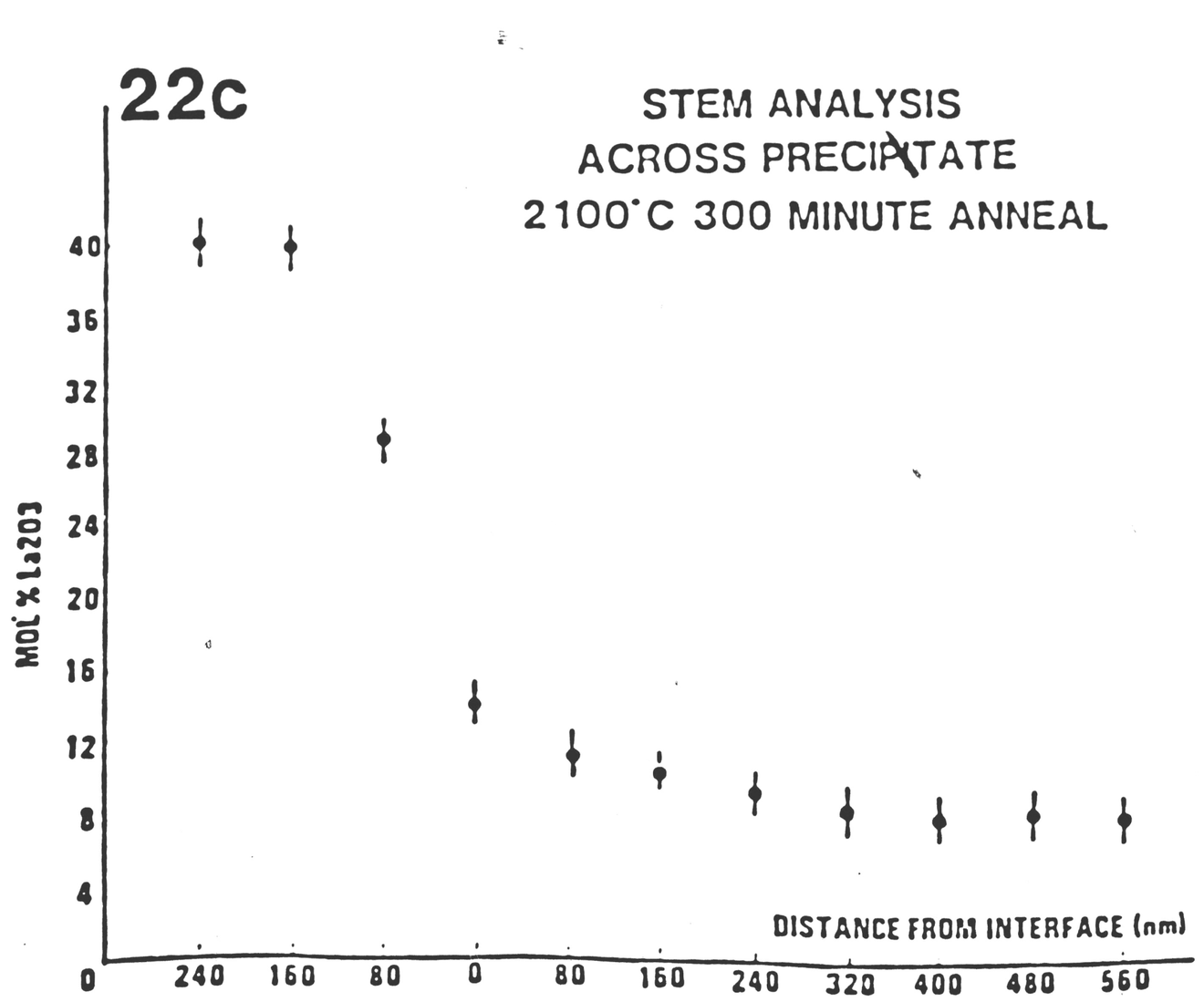

Figure 22b,c. b.) High magnification bright field micrograph of same precipitate as 22a showing twinned substructure. c.) The corresponding La_2O_3 profile across matrix/precipitate interface.

the discussion of the ferroelastic nature of the transition, the hexagonal cell can deform in several different ways to yield a variety of monoclinic domains, the number of which depend upon the space groups of the two crystal structures involved and the growth of which depend upon the strain condition of the interface.[25] The sectional, facetted appearance of the second phase (see regions marked by arrows in Figure 22b) may actually be individual, differently oriented domains of the monoclinic polymorph. Convergent beam electron diffraction studies on these second phases are necessary to verify this. The twinned regions of the second phase most likely result from the deformation involved in transforming from the hexagonal to the monoclinic phase. Caro[28] in his studies of Gd_2O_3, states that the deformation that transforms the three {110} planes of the hexagonal polymorph to 2{313} and 1(020) planes of the monoclinic structure yields two reciprocal systems of twins. The system of twins labeled type I involve twinning on a (313) plane together with a twin whose axis is [132]. The type II system consists of a $(3\bar{1}3)$ twin plane together with a twin whose axis is $[1\bar{3}2]$. Again, convergent beam electron diffraction analysis will be required to determine similar twin relationships in the Y_2O_3-La_2O_3 system if these precipitates are actually monoclinic derivatives of the hexagonal phase.

The micrograph of Figure 23 exhibits some fringe contrast in the second phase near the upper right corner of the picture. Series of fine, parallel lines also appear near the top of the second phase shown just to the right of center. The origin of these lines has not been investigated, however, Caro reports observing similar features in

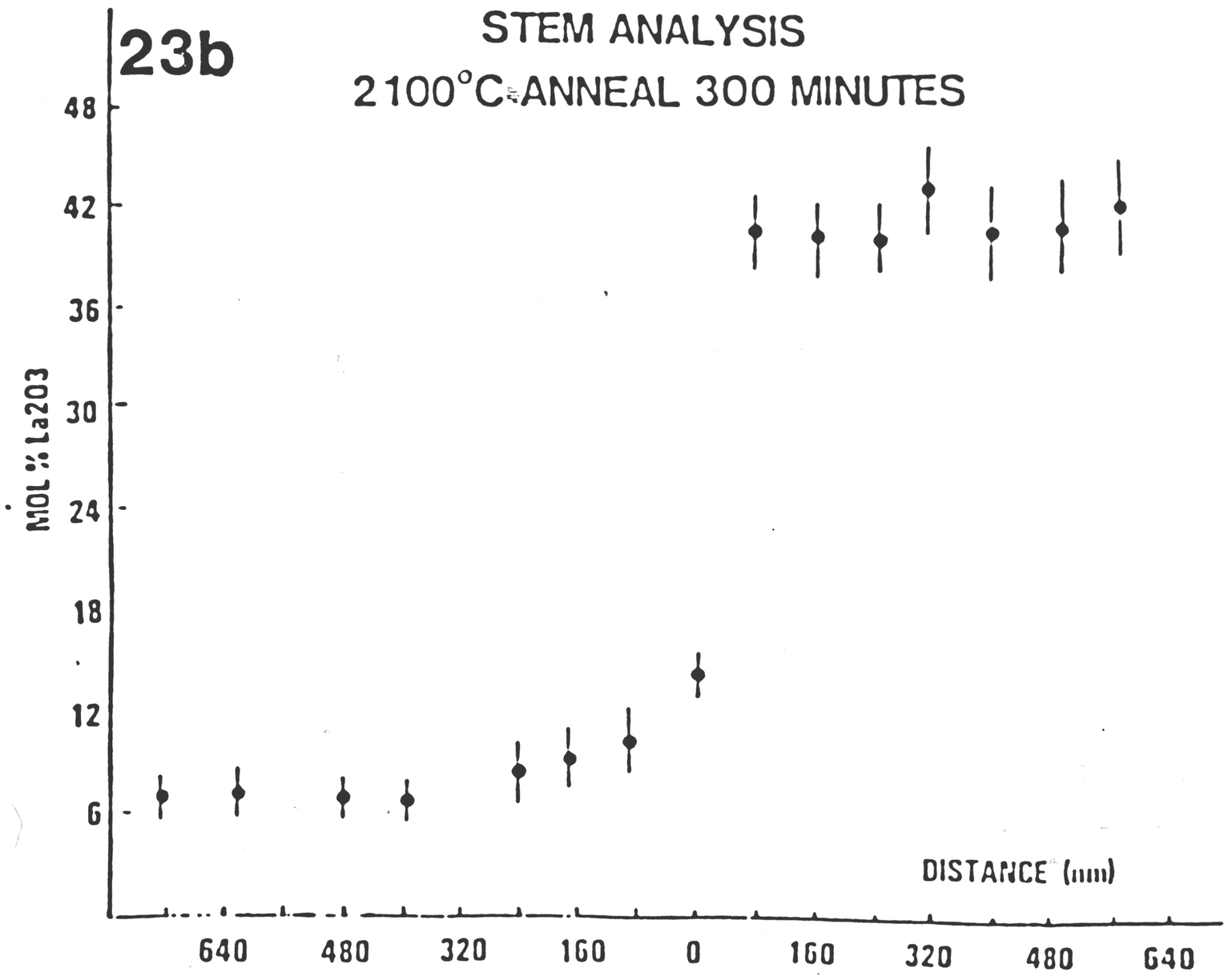

Figure 23 a,b. a.) Bright field micrograph of second phase of a different morphology obtained in sample annealed 300 min, at 2100°C b.) Corresponding microanalysis across interface separating matrix and twinned region of precipitate.

B-type Gd_2O_3. These features exist as complex lattices of curves, or lines with a definite crystallographic orientation ([010],]1$\bar{3}$2]], [132] for monoclinic; <1010> for hexagonal), or even isolated hexagonal figures whose contours have the same orientation as the above mentioned. The fringes appear as a result of differences in film thickness due to surface irregularity and the surface irregularity is a consequence of the stacking of tetrahedra in the monoclinic structure. The faces of the LnO_4 tetrahedra which do not lie parallel to the film surface form the slopes between the cliffs and plateaus which occur between adjacent layers of tetrahedra.(28)

Scanning transmission electron microscopy (STEM) microanalysis was performed on the precipitates shown in Figure 22b and the results shown in 22c. Typical nucleation and growth profiles exhibit a solute depletion zone adjacent to the interface which decreases with time to the equilibrium concentration. To observe the interface concentration microanalytically, the precipitate interface must extend through the thickness of the foil and it must be tilted parallel to the electron beam. The absence of the depletion zone indicates that either the system has reached equilibrium or that the facetted nature of the second phase is not yielding interfaces that extend through the foil. In this case, interaction of the matrix and precipitate with the electron beam at the interface yields compositions that are a mixture of both phases rather than just the matrix itself, thereby overshadowing any evidence of solute depletion in the matrix adjacent the interface.

The matrix exhibits concentrations of La_2O_3 in close agreement with the value depicted by the phase diagram of figure 1(∿8-9 mol% La_2O_3). However, the second phase has a La_2O_3 content as high as 38 to 40 mol%, far in excess of that dictated by the phase diagram (2-23 mol% La_2O_3 at 2100°C). A similar analysis across the twinned second phase of Figure 23 shows the same results--the equilibrium matrix concentration with a 40 mol% La_2O_3 precipitate concentration. Reasons for this discrepancy will be discussed later.

Microprobe analyses were performed on random portions of the second phase in the sample annealed for 300 minutes at 2100°C (Figure 18). Table 4 shows some of the probe results obtained. Except for the matrix phase which shows excellent agreement with TEM observations and phase diagram predictions, the concentrations calculated may not necessarily be precise since the size of the second phase usually lies below the resolution limits of the instrument. Nevertheless, some of the second phase areas sampled yielded La_2O_3 concentrations as high as 37 to 38 mol% La_2O_3. GTE[51] also reports similar findings of La_2O_3 contents far in excess of phase diagram predictions in some of the second phase studies they are performing.

The samples annealed at 2200°C, further into the two phase field, exhibit precipitation within the grain as well as on the grain boundaries. The backscattered electron micrograph of the sample annealed 300 minutes at 2200°C shows the distribution of the second phase (Figure 24).

Figure 25 shows typical microstructures for a 1 minute anneal. These precipitates lie within the grain, but appear to form

Table 4. Microprobe Analysis Results on 9 mol% La_2O_3/Y_2O_3 Samples Annealed 300 Minutes at 2100°C in the Two Phase Cubic and Hexagonal Field and Quenched to Room Temperature

mol% La_2O_3	mol% Y_2O_3	Location
9.9±1.08	90.10	matrix
10.6±1.12	89.39	matrix
9.8±1.06		matrix
14.59±1.623	85.41	grain boundary phase
19.73±2.02	80.27	grain boundary phase
25.70±2.59	74.30	grain boundary phase
36.97±3.61	63.03	grain boundary phase
16.45±1.75	83.55	grain boundary phase
12.37±1.34	87.63	grain boundary phase
14.02±1.51	85.98	grain boundary phase
12.21±1.35	87.79	grain boundary phase
31.79±4.26	68.21	grain boundary phase
16.29±1.69	83.71	grain boundary phase
12.977±1.33	87.03	grain boundary phase

Figure 24. Backscattered electron micrograph of polished section from 9 mol % La_2O_3/Y_2O_3 sample annealed 300 min. at 2200°C showing distribution of the second phase.

heterogeneously on dislocations as can be seen in the micrographs. Coherency strain is also evident. The bright field picture of Figure 26 was also taken from the sample annealed for one minute at 2200°C. The associated diffraction pattern obtained from the untwinned region of the second phase indexes as a $[\bar{2}\bar{1}1]$ zone of the hexagonal system (Figure 26b). Thus, this heat treatment appears to have successfully quenched in the hexagonal phase.

Quenches after 10 minutes and longer result in the twinned structures of Figures 27 through 29. The 10 minute anneal shows a rod-like morphology with a twin substructure. The sample annealed for 30 minutes at 2200°C exhibited precipitates of two different morphologies, one of which is shown in Figures 28a,b. Figure 28a exhibits the bright field picture of a precipitate within the cubic matrix as determined by electron diffraction analysis. The second phase is facetted with a ribbed substructure and coherency strains are also evident. The other type of morphology found in much greater numbers in the 30 minute sample is the long lath or elongated rod shapes shown in the three different precipitates of Figures 28c-e. The twins within the phase and the strained interfaces separating precipitate and matrix are clearly evident.

One reason for the dual morphology after 30 minutes at 2200°C may be that the precipitation process involves a two-step sequence: a heterogeneous nucleation of precipitates on dislocations in the early stages which coarsen by the time the second homogeneously nucleated precipitates form away from the dislocations at longer times. This argument was used by Busovne, Kotchick and Tressler[58] in their

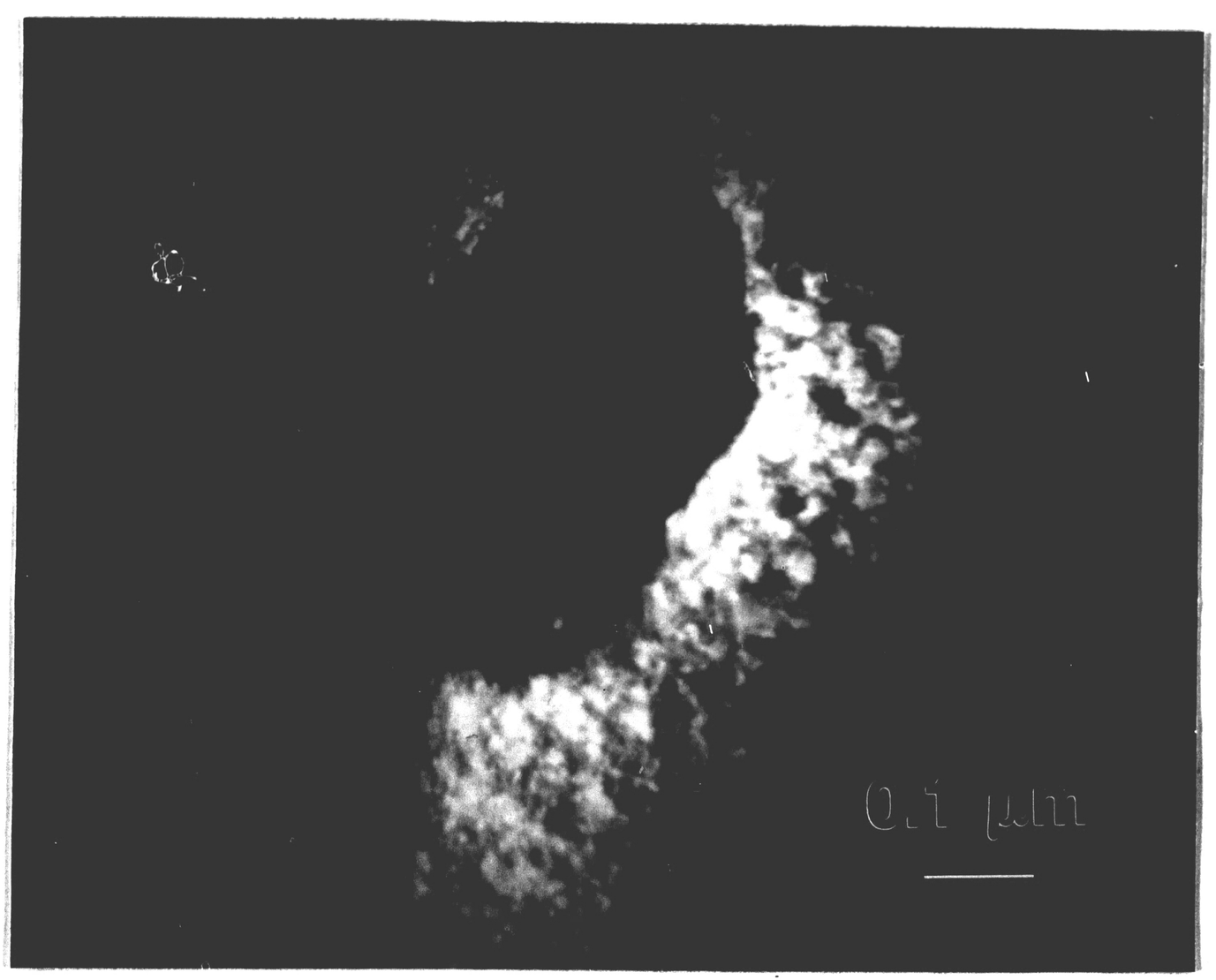

Figure 25. TEM micrographs of second phases found in 9 mol% La_2O_3/Y_2O_3 samples annealed 1 min. at 2200°C.

Figure 26a. Bright field micrograph of second phase in 9 mol % La_2O_3/Y_2O_3 sample annealed 1 min. at 2200°C.

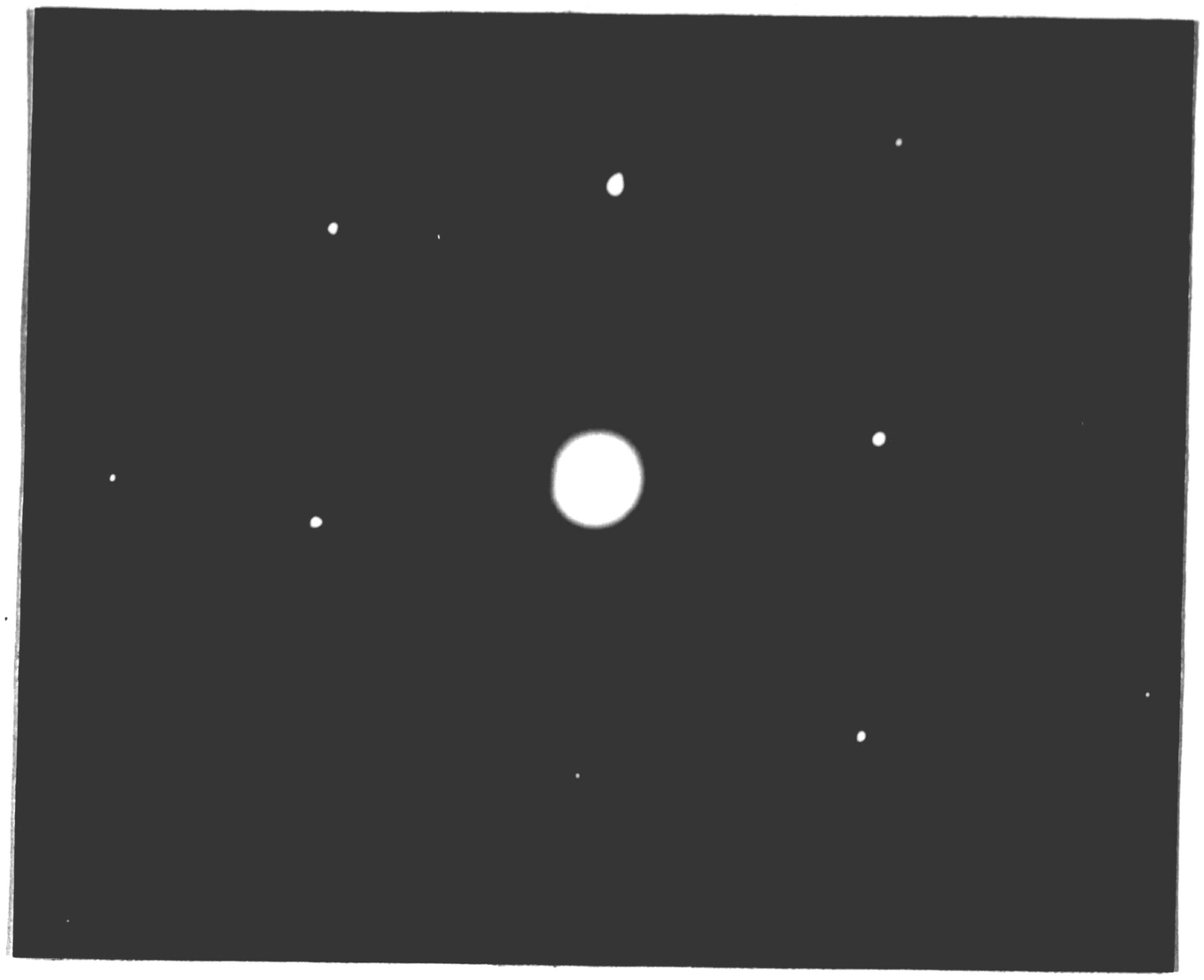

[$\bar{2}\bar{1}1$] HEXAGONAL

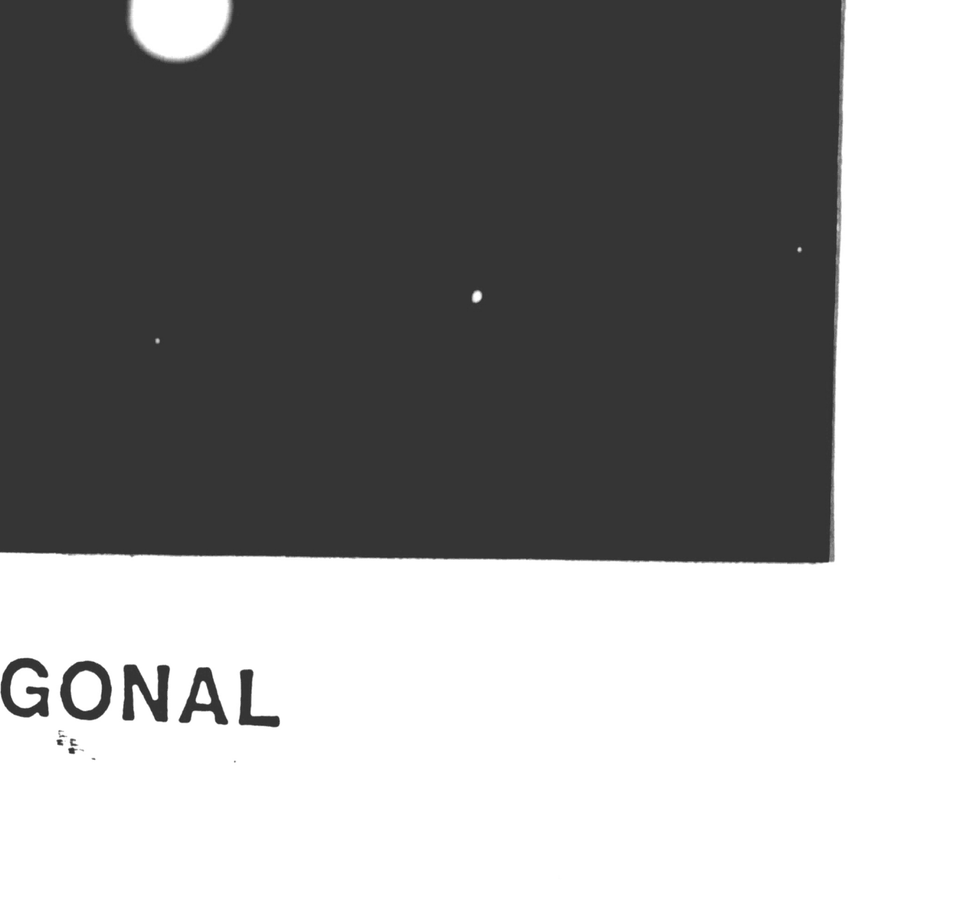

Figure 26b. The corresponding diffraction pattern of the untwinned area in 26a showing hexagonal symmetry.

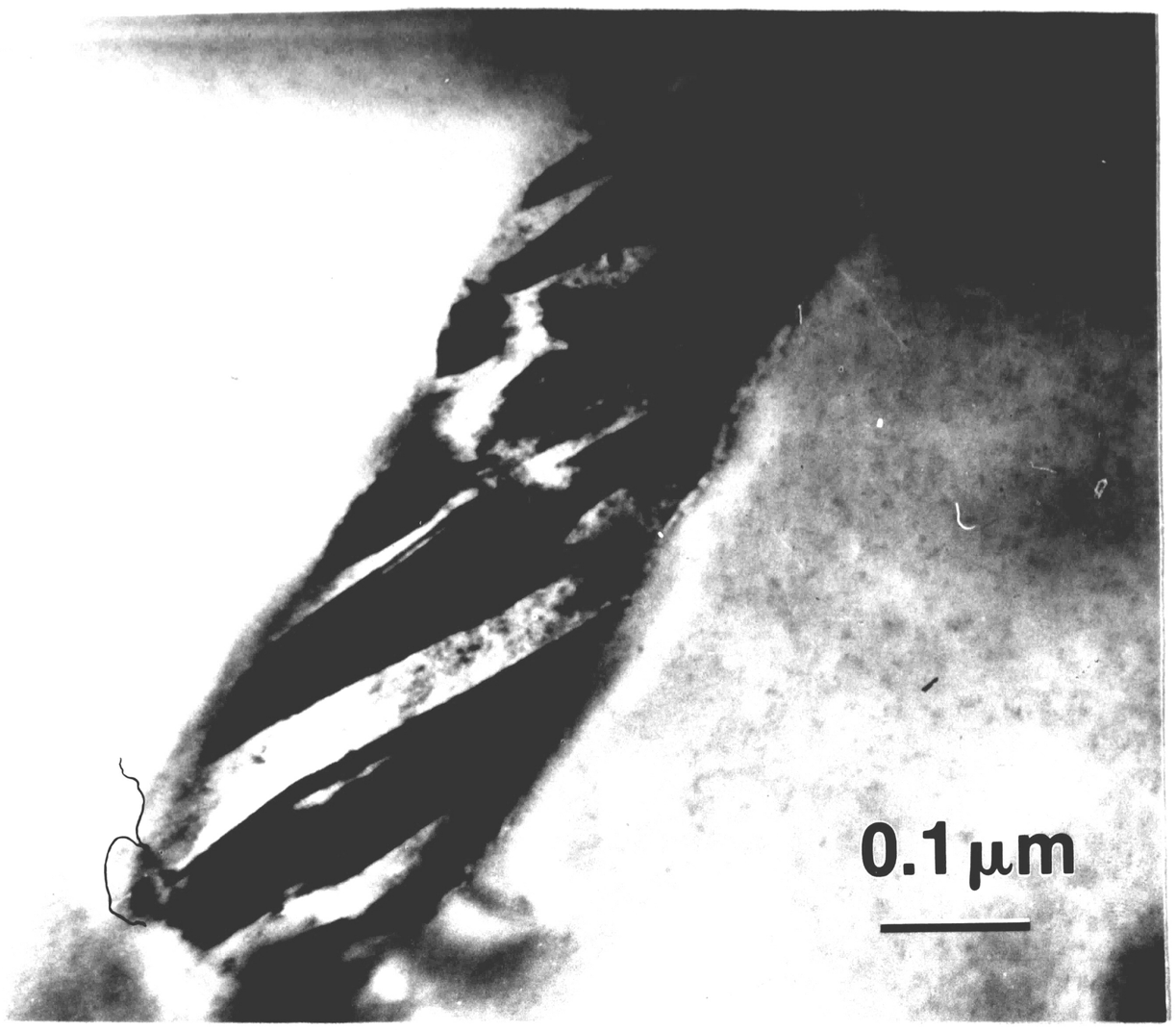

Figure 27. TEM bright field of rod-like second phase exhibiting twin structures found after 10 min. at 2200°C.

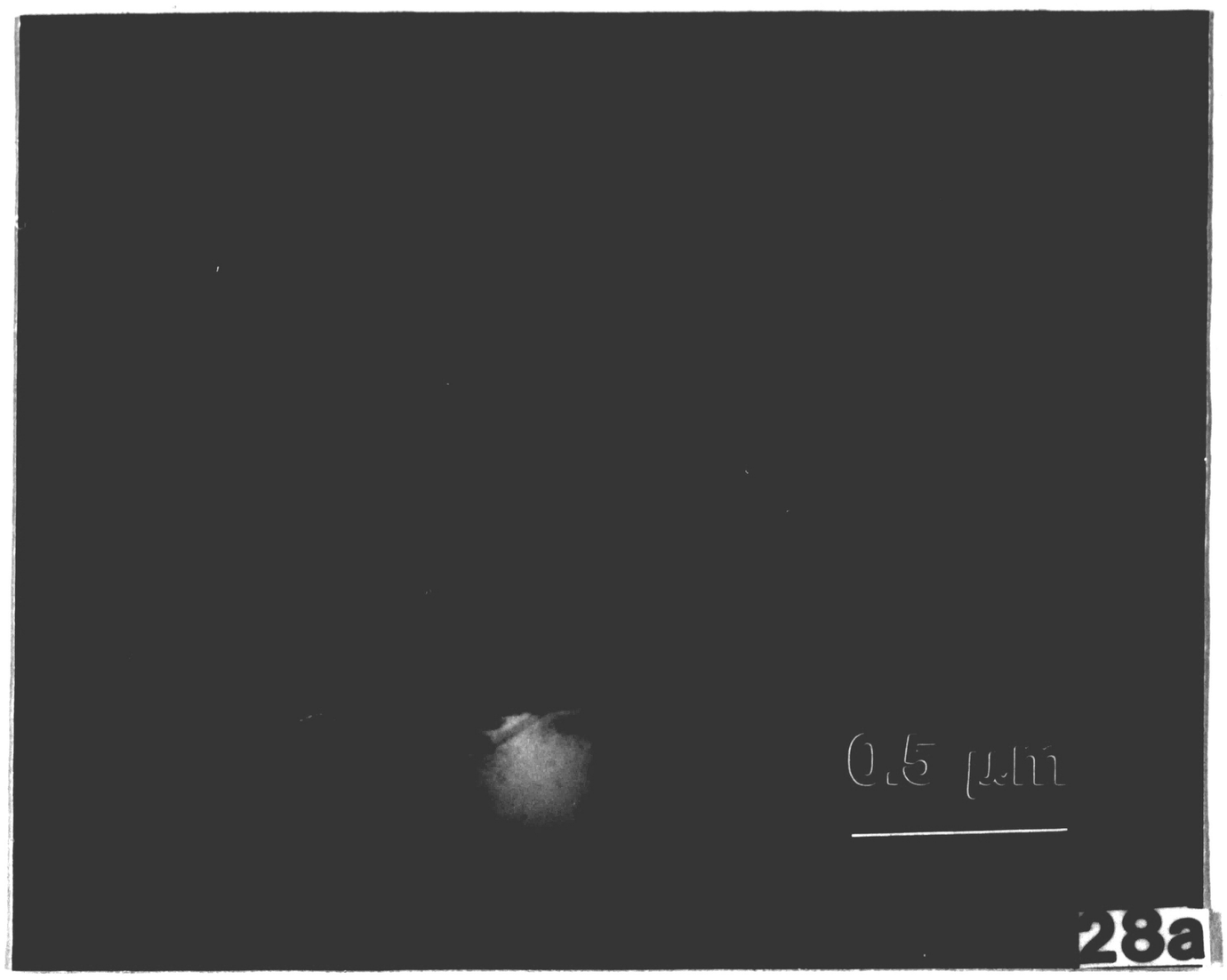

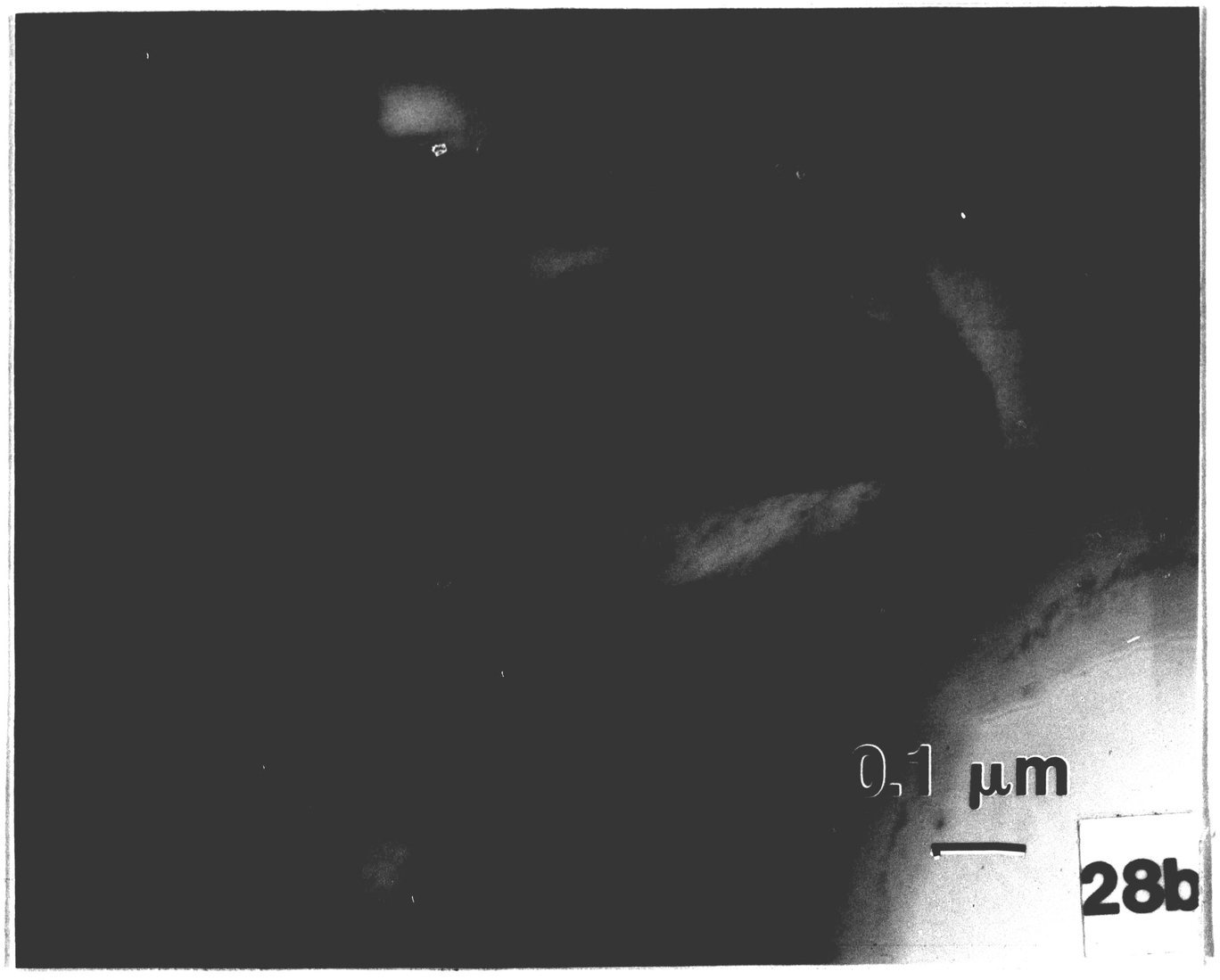

Figure 28a,b. Bright field micrographs of second phase of one type of morphology found in 9 mol% La_2O_3 samples samples annealed 30 min. at 2200°C.

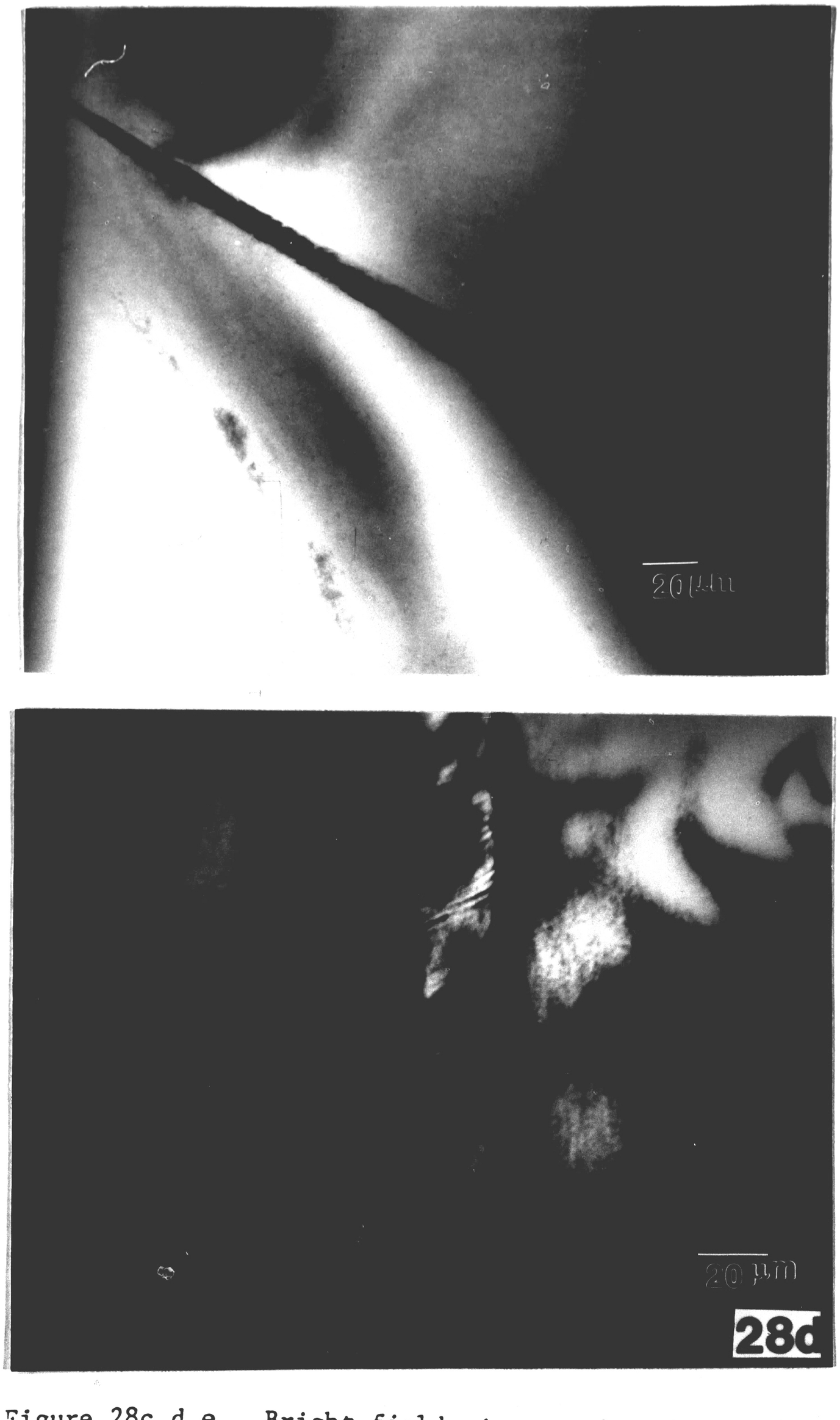

Figure 28c,d,e. Bright field micrographs of second phase with rod or lath-like morphologies more typical of a 9 mol% La_2O_3 sample annealed 30 min. at 2200°C. Note the strain contrast at the precipitate/matrix interface (d,e) and the overall twinned structure.

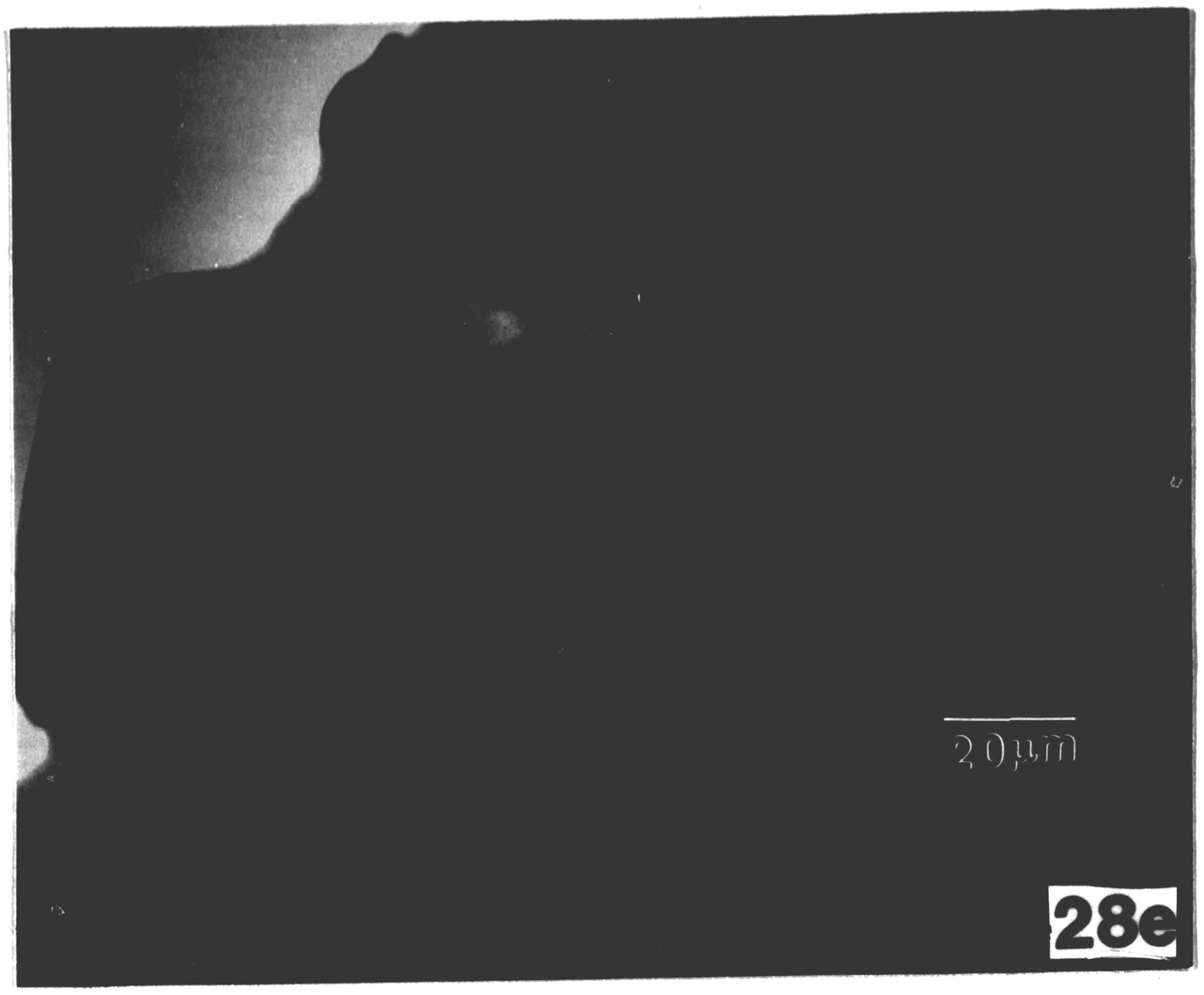
20µm
28e

explanations of bimodal distributions of Ti^{+4} rich precipitates in TiO_2 doped sapphire. Another possibility for the observed morphologies may be that at 2200°C, the kinetics of the precipitation sequence are so rapid that after 30 minutes, the equilibrium volume fraction of second phase is rapidly being approached. The small, randomly dispersed second phases shown after one minute may have begun to coarsen by 30 minutes so as to develop the long, rod like morphologies. As a result, the small particles in Figure 28a could actually be a result of the Ostwald ripening phenomenon. Dissolution profiles of these second phases will help determine this, however, the facetted nature of the second phase will make accurate interface concentrations difficult to detect.

For 300 minutes at 2200°C, the microstructure consists almost exclusively of the long, rod like second phases. Most of the second phases of the 2200°C/300minute samples nucleate within the grain and show a preferred growth direction and orientation relationship with the cubic matrix.

Figure 29 shows the various precipitates observed for the 2200°C/300 minute sample. The STEM profile (Figure 29d) across the precipitate of Figure 29c shows a La_2O_3 matrix concentration in agreement with phase diagram predictions (∿6-7 mol% La_2O_3) while the second phase exhibits La_2O_3 contents near 25 to 26 mol% La_2O_3. Again, the second phase La_2O_3 concentration exceeds phase diagram predictions (∿19 mol% La_2O_3 at 2200°C). Analyses on other precipitates such as those shown in Figure 30a yielded similar results (30b). Microprobe analyses on regions of the second phases shown in Figure 24 confirmed

Figure 29a,b,c. Typical microstructures obtained after 300 min. at 2200°C showing elongated, rod or lath-like morphologies.

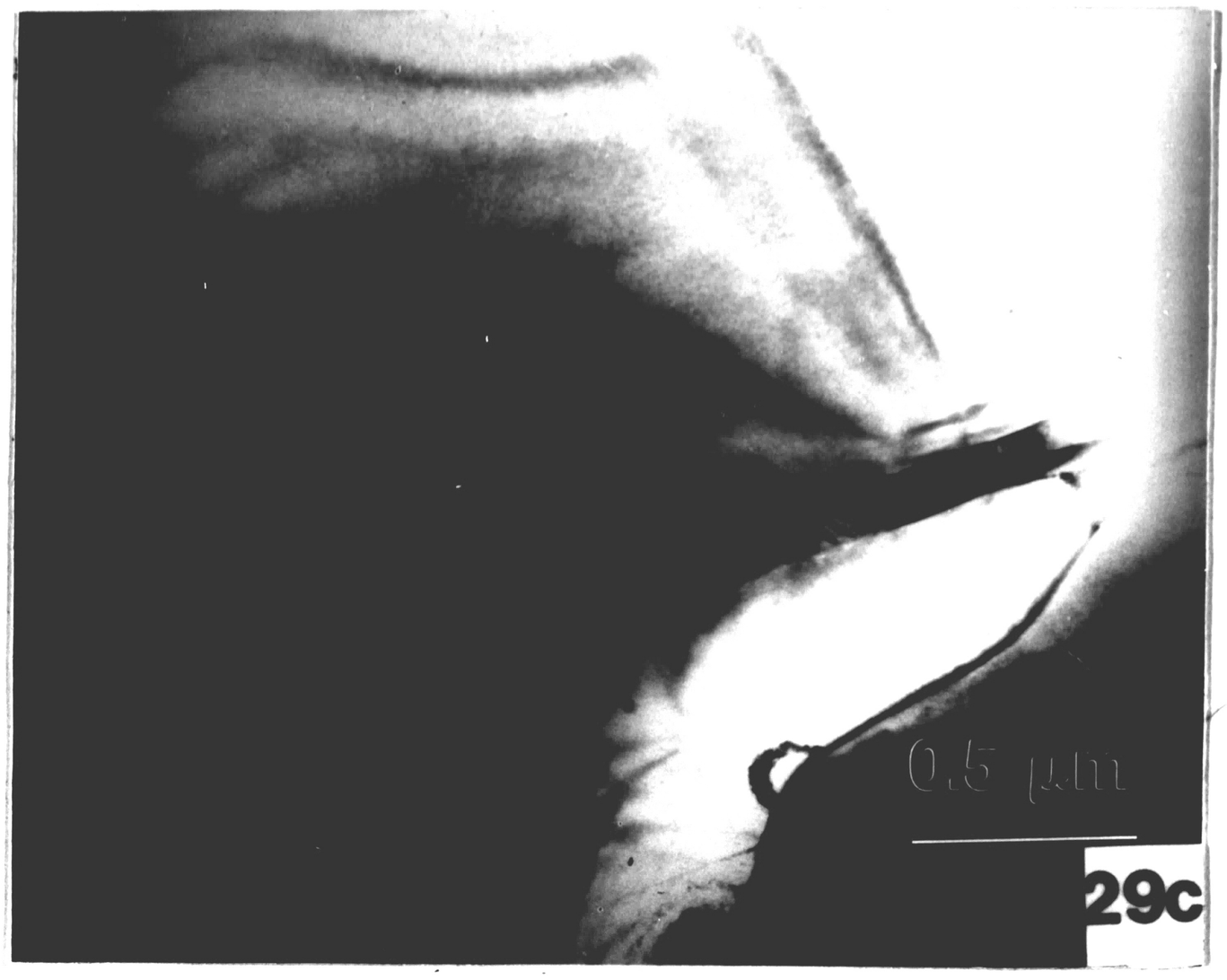

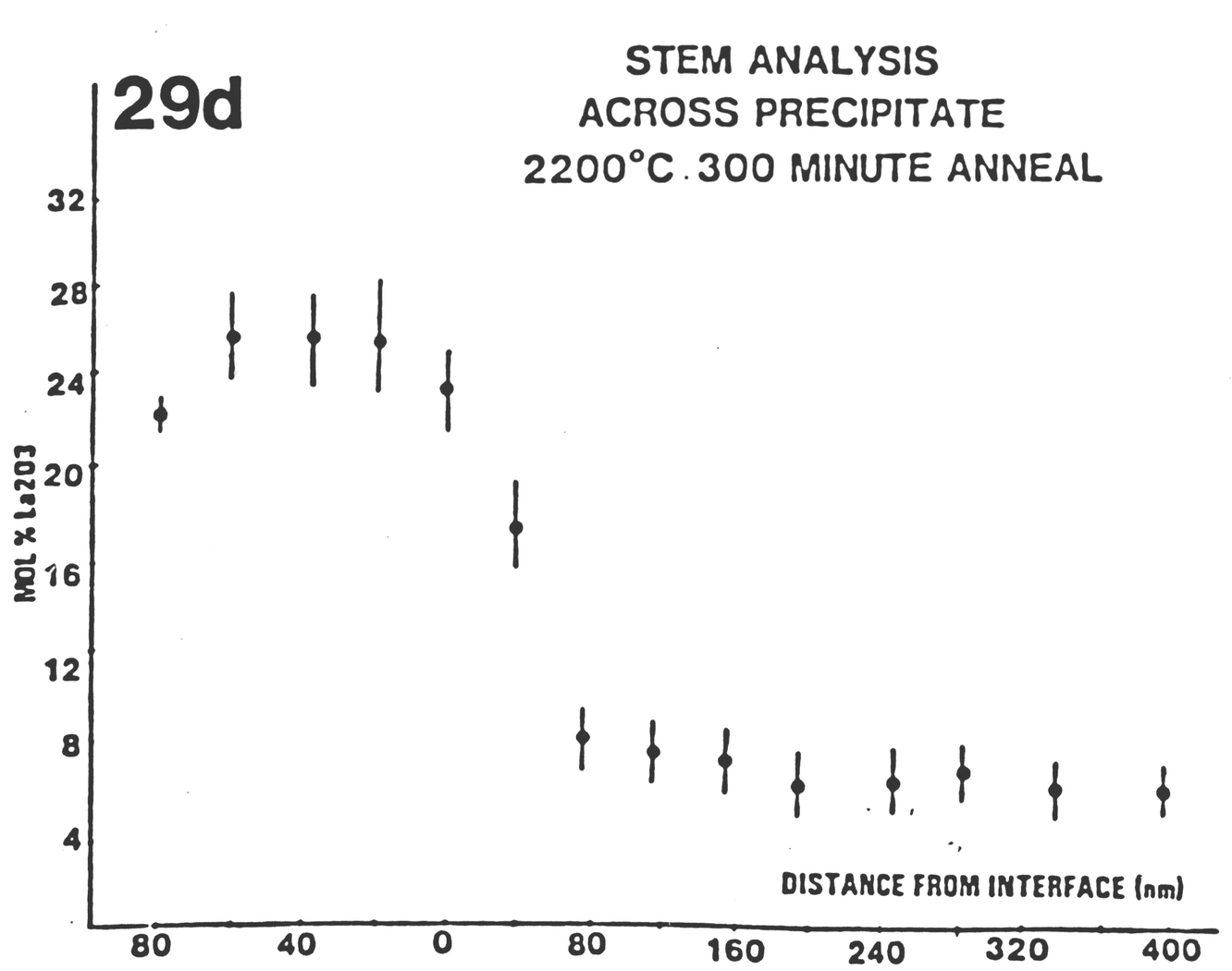

Figure 29d. The microanalysis profile across the precipitate/matrix interface for the precipitate of 29c.

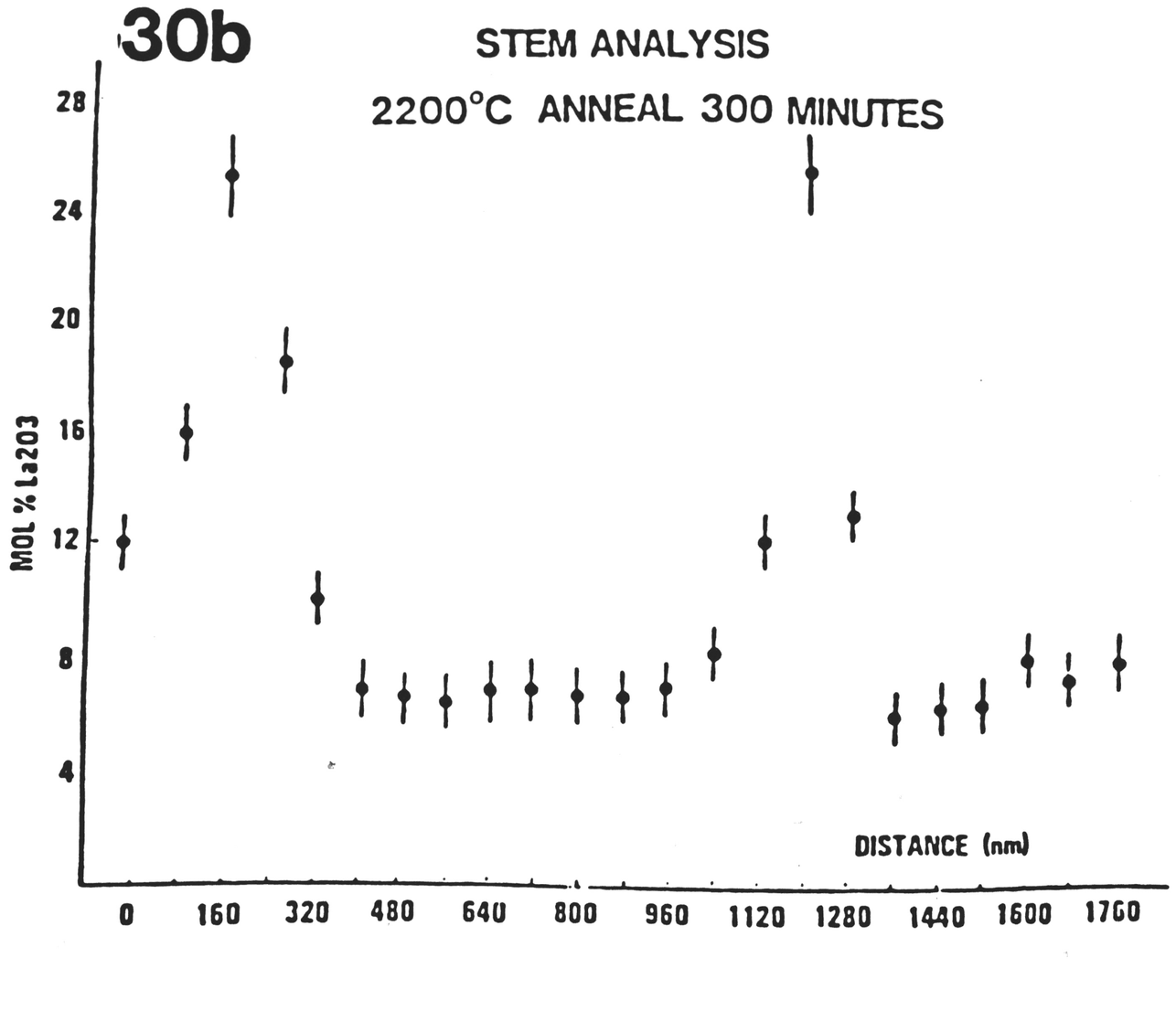

Figure 30a,b. a.) Series of precipitates found after 300 min. at 2200°C. b.) The microanalysis across two of the second phases, showing the variation of La_2O_3 content between precipitate and matrix.

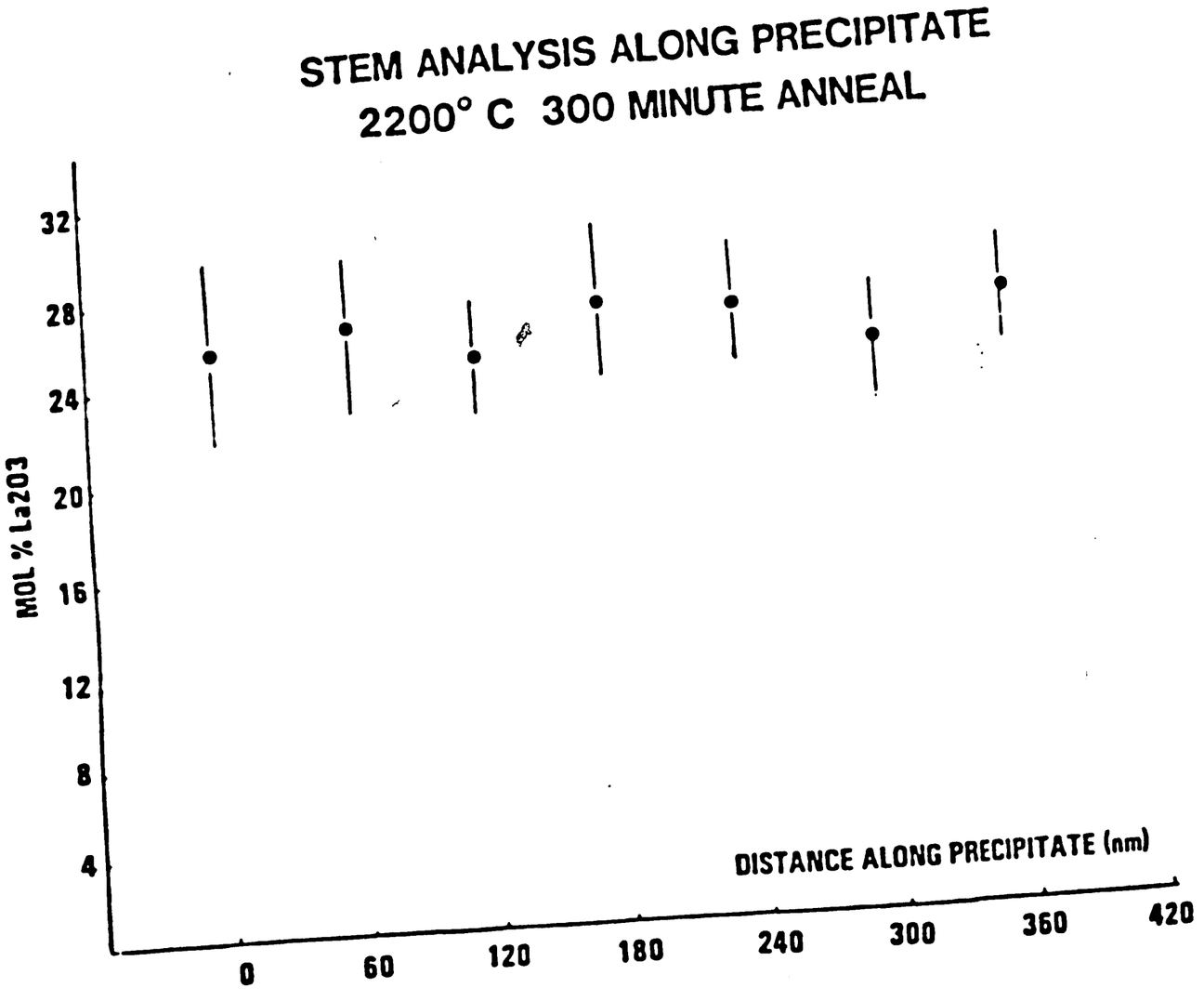

Figure 30c. Microanalysis results along one of the precipitates of 30a showing composition invariance.

RETAKE

The Operator has Determined that the Previous Frame is Unacceptable and Has Refilmed the Page in the Next Frame.

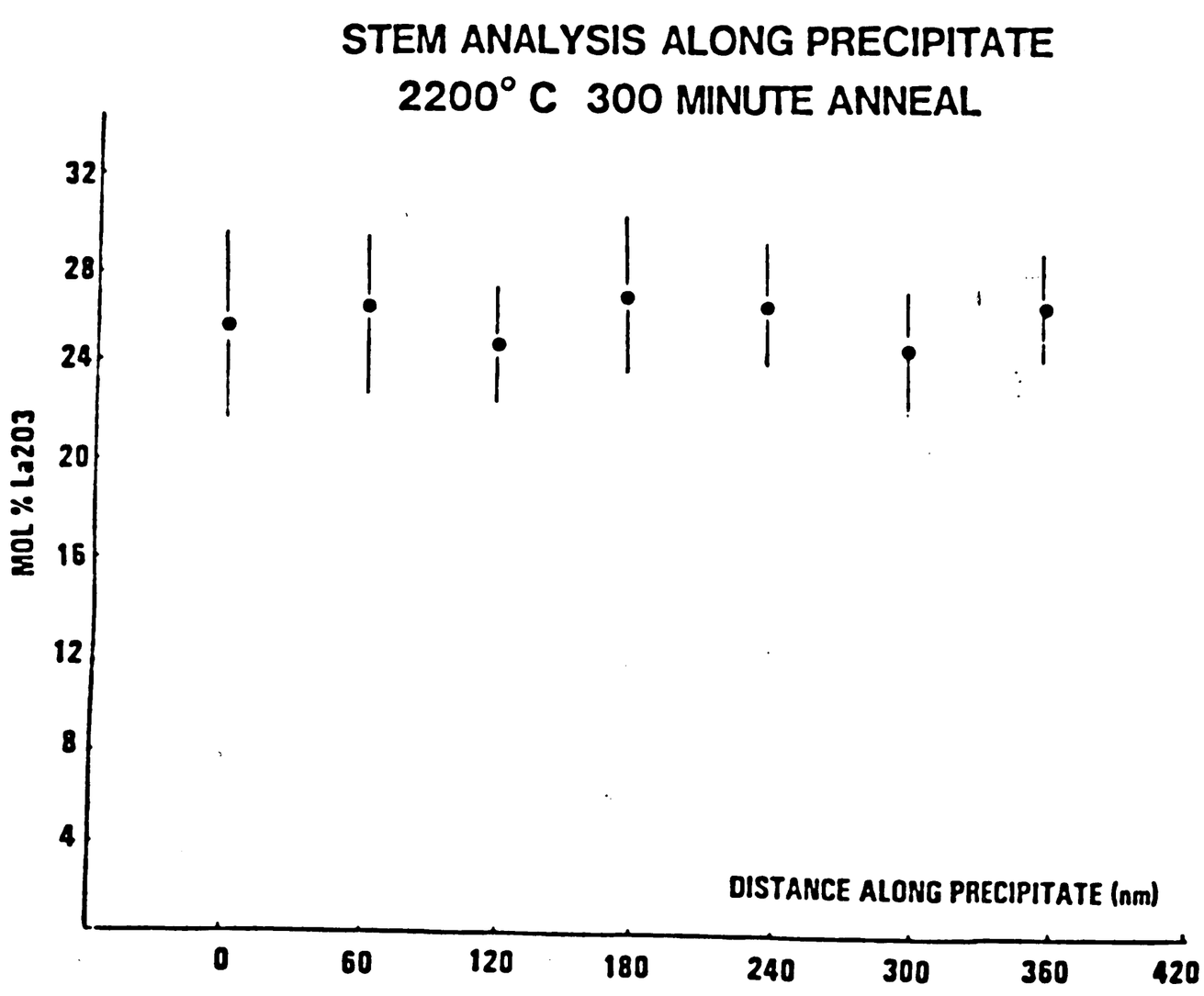

Figure 30c. Microanalysis results along one of the precipitates of 30a showing composition invariance.

Table 5. Microprobe Analysis Results of 9 mol% La_2O_3/Y_2O_3 Samples Annealed 300 minutes at 2200°C in the Two Phase Cubic and Hexagonal Field and Quenched to Room Temperature

$\%La_2O_3$	$\%Y_2O_3$	Location
17.10±1.78	82.90	grain boundary phase
28.20±2.69	71.80	grain boundary phase
11.04±1.19	88.96	grain boundary phase
8.90±0.95	91.10	matrix
8.47±0.90	91.53	matrix
8.48±0.904	91.52	matrix
8.33±0.87	91.66	matrix
12.42±1.32	87.58	triple point phase
8.54± .93	91.46	matrix
12.69±1.38	87.30	triple point phase
12.47±1.36	87.53	grain boundary phase
16.06±1.65	83.94	grain boundary phase
22.59±2.22	77.41	grain boundary phase
29.89±2.92	70.10	grain boundary phase
14.66±1.59	85.34	grain boundary phase
13.87±1.504	86.13	grain boundary phase
23.12±2.29	76.88	grain boundary phase
23.19±2.30	76.81	grain boundary phase
8.94±0.95	91.06	matrix

the presence of second phase La_2O_3 concentration as high as 28-29 mol% La_2O_3 (Table 5). All the needle-like precipitates showed composition invariance along the precipitate as evidenced by the STEM analysis of Figure 30c.

As mentioned, the second phase concentrations of the samples annealed 300 minutes exceed the limits defined by the hexagonal/cubic and hexagonal solvus boundary while matrix concentrations agreed very well with phase diagram predictions. All analyses were taken in precipitates lying on the edge of the foil and thickness estimations by the convergent beam diffraction technique on most of the samples revealed that the thin film criterion was upheld. Microprobe analyses on both samples testify to the existence of La_2O_3 concentrations in the second phase in excess of the phase diagram boundaries.

An interesting explanation for these anomalies which requires further investigation is the effect of coherency strain on the equilibrium composition values obtained in the phase diagram. As mentioned, the interfaces separating precipitate and matrix exhibit strain contrast and facetting, indicating attempted lattice matching across the boundary. Models have been proposed to qualify the effects of including coherency strain and elastic energy terms in the determination of phase equilibria for two phases coexisting coherently.

Recent models by Williams[60] and Cahn and Larche[61,61] on phase equilibrium in systems exhibiting coherency of the second phase with the matrix have proven theoretically that the inclusion of elastic and interfacial energies in the determination of phase equilibria often invalidates the phase rule. Williams has shown in his study of the

Cu-Au system that interfacial energy directly restricts the minimum volume fractions which can exist in the coherent mixture. The common tangent construction to the classical free energy curves which are usually based in the volume free energy, designate the equilibrium compositions of the phases present at the points where the common tangent touches the minima of the two energy curves. However, with inclusion of coherency and interfacial energies, the tangent touches the free energy curves at more restricted compositions such that the free energy of the coherent system is a minimum (Figure 31). Interfacial energy, not dependent upon relative volume fractions of the two phases, raises the total energy reducing the limits between which the coherent mixture can exist. Relative volume fractions of the two phases becomes restricted, decreasing the width of the two phase field.

Williams' work begins to explain why the existence of metastable coherent structures of stable phases alter limits of the field boundaries in the phase diagram which is usually determined for the more stable incoherent second phases. Cahn and Larche propose a model for the invalidation of the phase rule due to coherency. They define incoherent equilibrium as a state where each phase experiences the same hydrostatic pressure and in which the chemical potentials for each component are constant. The free energy remains invariant to transfers of atoms from one phase to another as each of the same phases form separate crystals which do not interact elastically with the other phases.

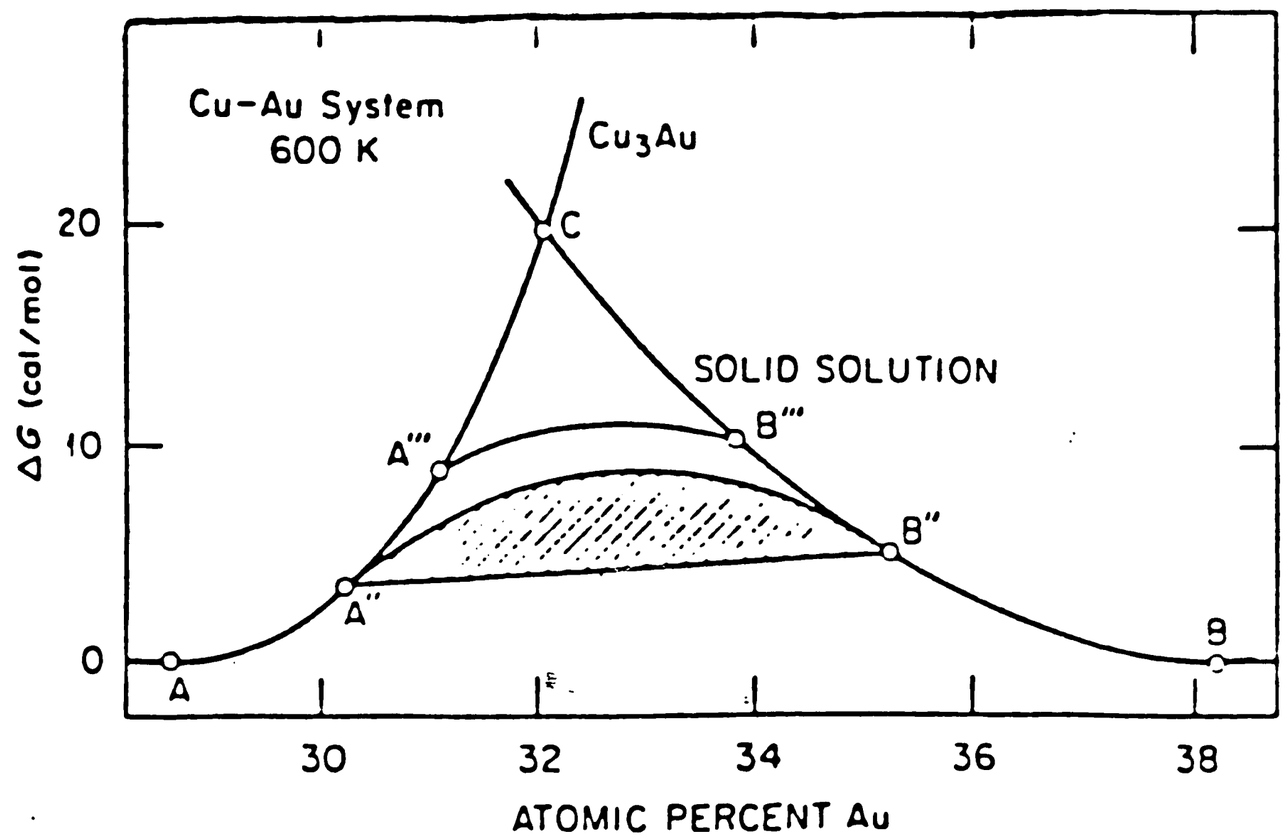

Figure 31. Modification of equilibrium concentrations by the inclusion of coherency energies (A",B") and both coherency and interfacial energies (A''',B''') in the Cu-Au system. (After Williams[60])

Coherent equilibrium refers to equilibrium subjected to a constraint which does not permit discontinuities along the interface. Coherent coexistence of the two phases with different stress free lattice parameters yields internal stresses which depend upon the size and shape of the second phase particles. Transfer of atoms from one phase to another changes the stress fields in a way that the coherent compositions differ from incoherent compositions in a manner that reduces the elastic energy. This elastic energy can be reduced by a change in composition to reduce the mismatch between phases or by a reduction of the volume fraction of the second phase, which again requires individual phase composition adjustment. Both of these however yield increases in total free energy of the individual phases, thus showing why the coherent equilibrium case is a metastable form of a stable phase.

Coherent phase diagrams differ both qualitatively and quantitatively from incoherent diagrams. The classical phase equilibrium determination by the common tangent construction to the minima of two free energy curves for mixtures of phases whose free energy equal the sums of the free energies of individual phases becomes invalid with the addition of an elastic term due to coherency. Addition of the elastic term to the free energy curve yields a new free energy curve which can be used with a common tangent construction to determine coherent equilibria. The points of equilibria define critical points where elastic energy can be reduced by narrowing the composition difference and therefore the lattice parameter difference which results in a coherent miscibility gap within the incoherent one.

Cahn and Larche define a parameter A to represent the effects of coherency induced elastic energy. It is proportional to the ratio of the linear mismatch between phases (ε) and the difference between equilibrium compositions of the incoherent phase diagram field boundary ($C_\beta^e - C_\alpha^e$) i.e. A relates the coherency energy to the differences between the energy of a single phase and that of the same system after it forms an equilibrium incoherent mixture of phases.

$$A = \frac{4VE\varepsilon^2}{(1-\nu)F(C - C_\beta^e)_\alpha^e}$$

where V = molar volume,

E = Young's modulus

ν = Poisson's ratio

The parameter A is large for large mismatch (ε) or small differences between equilibrium compositions in the incoherent diagram. The diagram of Figure 32 shows the relationship between this energy parameter A and the reduced composition w ($=1-2(C-C_f^e)/(C_\beta^e-C_\alpha^e)$ where C = constant overall composition equal to $ZC_\alpha+(1-2)C_\beta$, and Z is the mol fraction of α phase). For A>4, only single phase occurs however for any A<4, two phases can coexist coherently over a range of alloy compositions. This range is enclosed by the incoherent composition boundaries defined where w=±1. The compositions of the coherently coexisting phases may lie outside the defined boundaries of the incoherent diagram (A=0) (Figure 33). These tie lines shift with A until in the limit, A=0 and the compositions of the coexisting phases correspond to those depicted by the field boundaries of the two phase

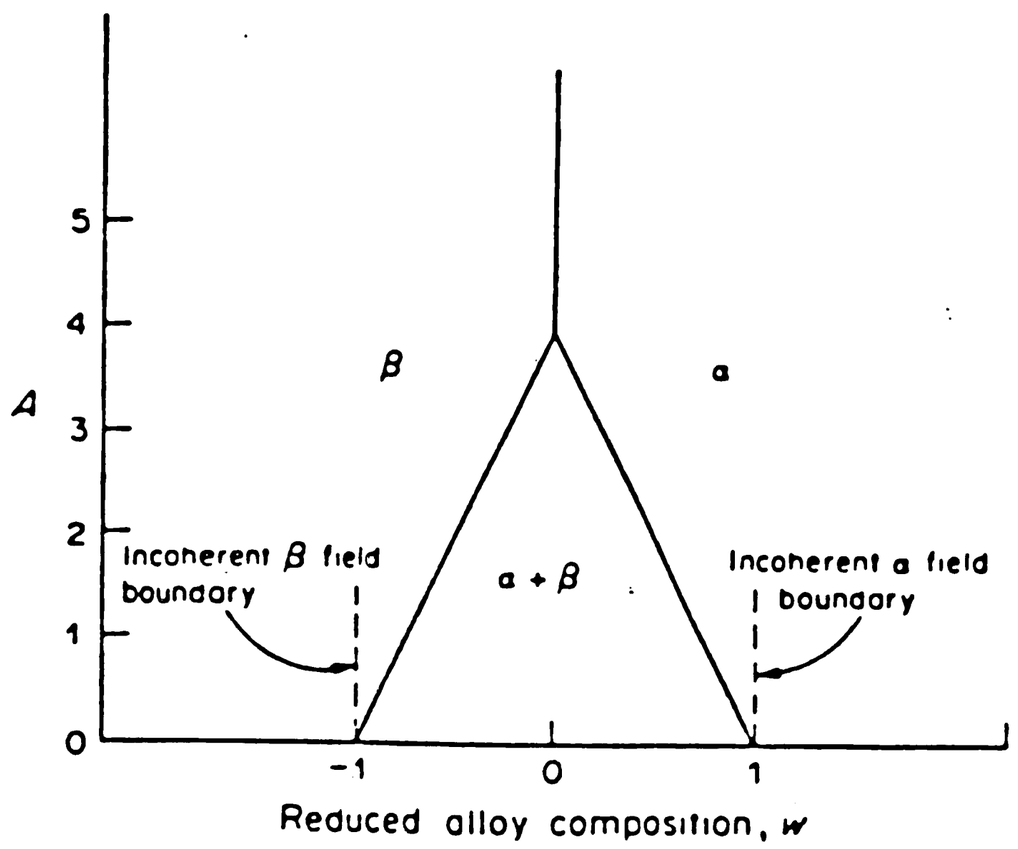

Figure 32. Field diagram in terms of the dimensionless composition w and the energy ratio A. (see text). Coherent two phase field is confined to the triangle whose apex is (0,4), the Williams' point. Above this point, two phase coexistence does not occur. (After Cahn and Larche[61]).

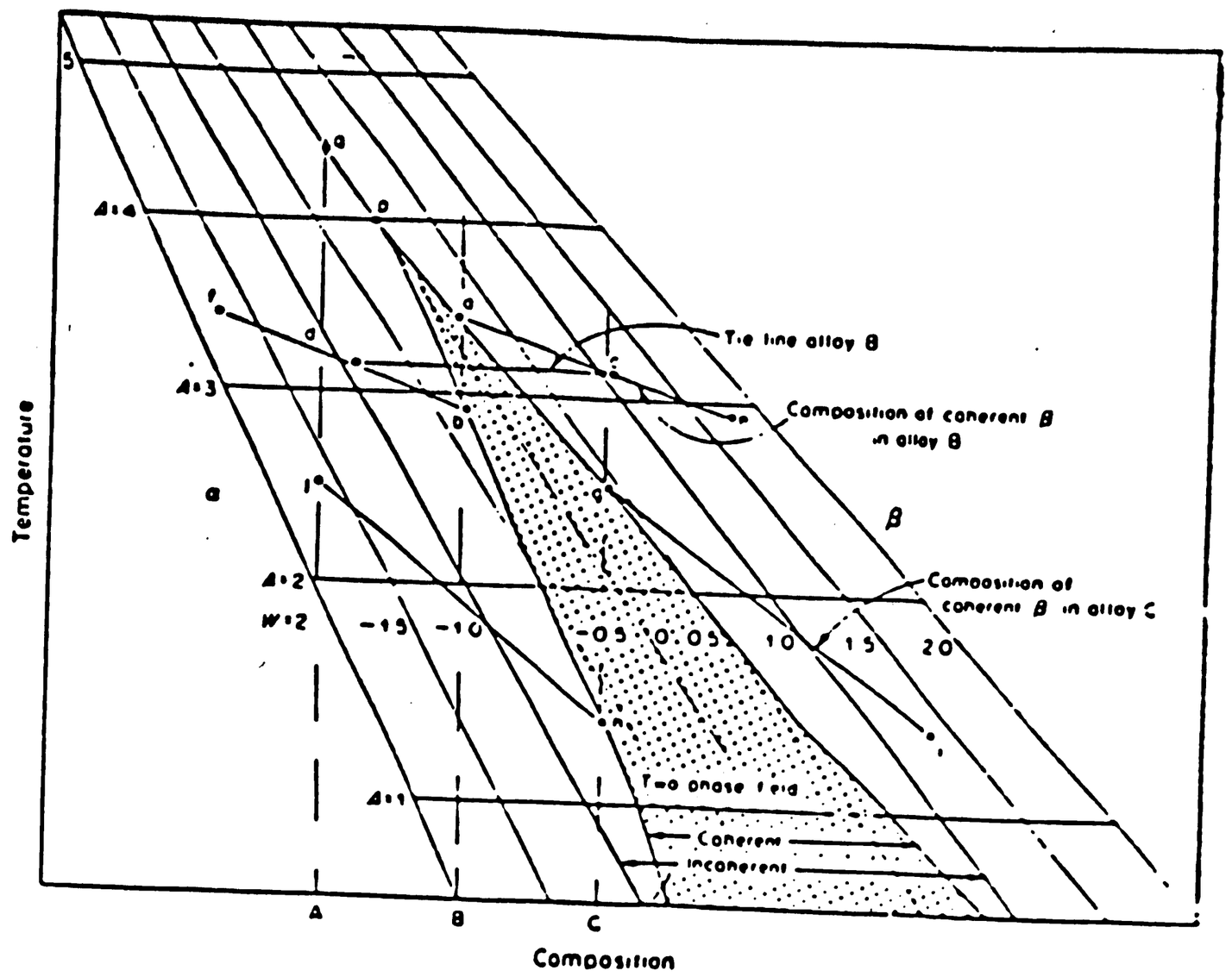

Figure 33. Schematic two phase field with temperature and composition as axes.

The A scale is indicated. The T_o line and incoherent field boundaries are along the w=0, 1,-1 curves respectively. The William's point occurs at p, and predictions for coherent equilibrium for three different alloys are given.

Alloy A: transfoms at q and shows no two phase coexistence

Alloy B: shows two phase coexistence in the temperature range a-b marking the field boundaries. Measurement of the compositions of the coexisting phases in this alloy would give tie lines like c-d whose locus of endpoints give tie end curves ace and fdb.

Alloy C: would provide points hg on the diagram field boundary but would give tie end curves gi and hj.

(After Cahn and Larche[61])

region determined for the incoherent case. The shifting of tie lines with coherency energy invalidates the phase rule. In the regions of two phase coexistence below the Williams point (i.e. the point at which the two phase region disappears and the single phase begins), there is one more degree of freedom than the phase rule allows due to the constraining effects of coherency. (Standard derivations of the phase rule assume equal, constant pressures in all coexisting phases.) Away from this point, the two phases can be different elastically, and compositions depend on whether the softer phase is the matrix or minor phase.

Thus, the theorem that ends of tie lines lie on field boundaries of the phase diagram and are thus independent of volume fraction do not apply for coherent equilibria. The entire concept of coherent equilibria derives from the minimization of elastic energy. Reducing the volume fraction of the second phase reduces elastic energy which can be facilitated by shifting the phase compositions. The amount of shift depends upon the balance between elastic and chemical energy.

The coherent equilibrium phenomenon then imposes some serious implications on the accuracy of present phase diagram determinations. The field boundary limits obtained by equilibrating a series of binary alloy samples of differing compositions and observing the phases present should be identical with tie compositions determined from individual phases of samples exhibiting two phase coexistence. For two phases in coherent equilibrium, however, the experimental field determination will provide a coherent field diagram, but because the composition of the individual phases in the two phase region depends

upon their volume fractions, the individual compositions will differ with the initial concentrations for the same temperature in the same two phase field.

Coherent equilibrium may explain why the compositions of the second phase determined in this study are in excess of phase diagram predictions, but it doesn't account for the matrix being in agreement with the diagram concentrations. A series of experiments must be performed to assess the validity of the proposed effects of coherency strain on two phase equilibrium in the Y_2O_3/La_2O_3 system. One such test will be to anneal in the two phase region for various times to attain a series of precipitates of varied degrees of coherency and to evaluate the change in composition as a function of the degree of coherency. Rhodes' experiments with second phase development in samples which were sintered in the two phase field and quenched to room temperature revealed second phases in the form of large incoherent abnormal grains. Microprobe analyses on these second phases showed excellent agreement with phase diagram predictions.(63)

Thirty mol percent La_2O_3/Y_2O_3 samples

Pressed pellets of thirty mol percent La_2O_3/Y_2O_3 powders were prepared by the oxalate coprecipitation technique, sintered at 2025°C in the single (hexagonal) phase region, and quenched to room temperature. The bulk of the sample was ground for x-ray powder diffraction analyses and thin foils made for electron diffraction and STEM analysis.

X-ray results for the bulk sample for scans between 15 and 65° are shown in Figure 34. The associated table of d-spacings for the

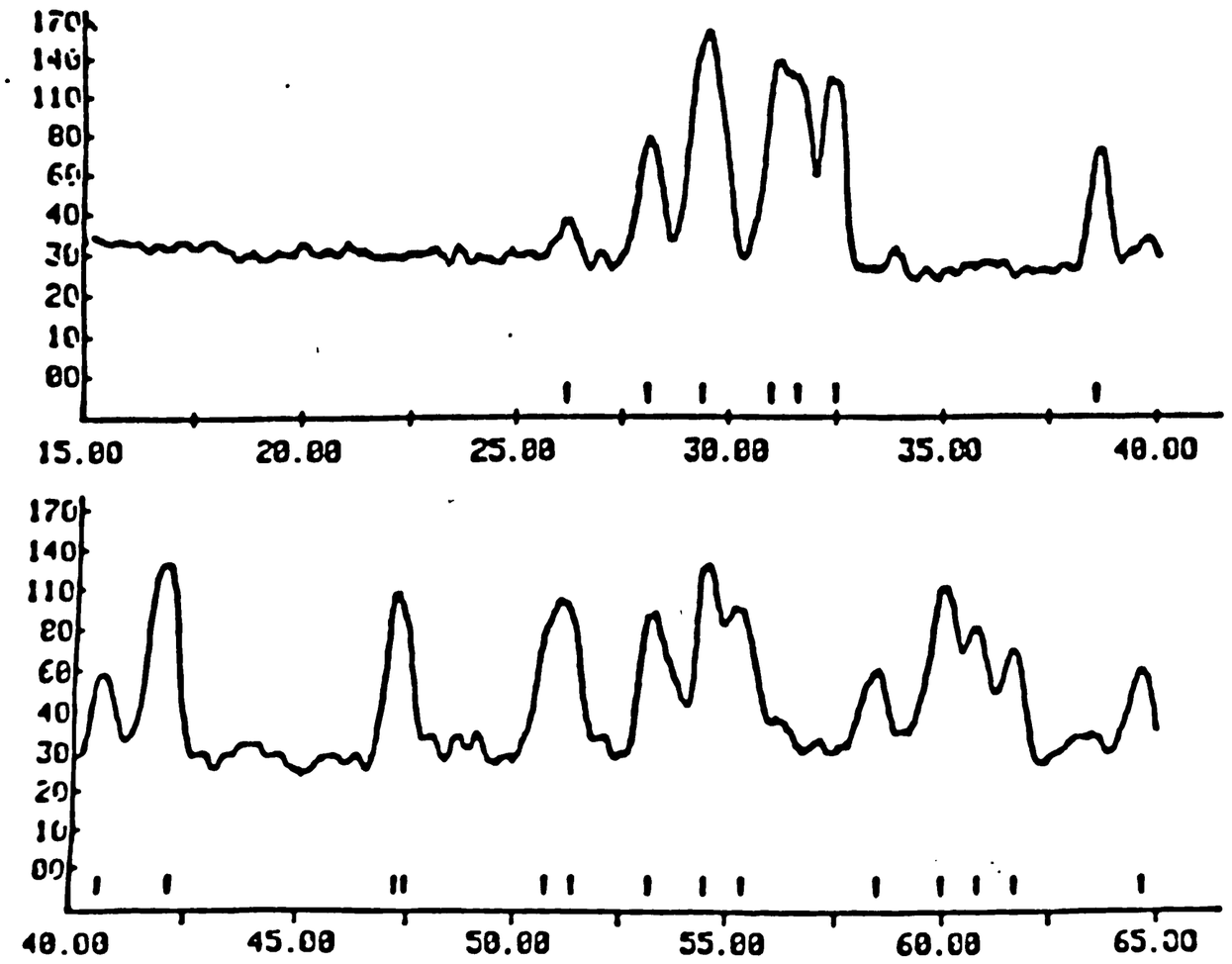

15° TO 65° X-RAY SCAN 30 MOL % La2O3 SAMPLE

2-THETA (DEG)	WIDTH (APPROX)	COUNTS PEAK	COUNTS BKGND	D (ANG)	I (NORM)
26.18	0.33	14.	26.	3.4045	11.96
28.06	0.62	56.	25.	3.1799	49.13
29.37	0.88	114.	25.	3.0410	100.00
30.95	0.33	110.	24.	2.8897	96.30
31.55	0.29	88.	24.	2.8356	77.18
32.45	0.31	90.	23.	2.7594	78.83
38.52	0.50	53.	23.	2.3371	46.55
40.60	0.58	30.	25.	2.2218	26.42
42.15	0.37	94.	26.	2.1438	82.18
47.21	0.36	92.	24.	1.9250	80.50
47.44	0.30	67.	25.	1.9164	58.73
50.74	0.32	59.	25.	1.7994	51.79
51.37	0.50	59.	25.	1.7786	51.79
53.19	0.56	69.	25.	1.7220	60.17
54.49	0.43	96.	25.	1.6839	83.89
55.38	0.54	77.	24.	1.6591	67.64
58.51	0.40	37.	24.	1.5776	32.50
59.98	0.57	94.	23.	1.5423	82.18
60.82	0.38	50.	23.	1.5230	44.03
61.70	0.50	58.	23.	1.5034	50.45

Figure 34. Results of x-ray powder diffraction analysis on 30 mol % La_2O_3/Y_2O_3 sample quenched from 2025°c, exhibiting the crystalline peaks between 15° and 65°

Table 6 - X-ray Diffraction Data Comparison for 30 mol % of La_2O_3/Y_2O_3 Sample Quenched from the Single Phase Hexagonal Field

Sample	I/I_o	Monoclinic	I/I_o	Hexagonal	I/I_o
3.4045	12	3.396	10	3.30	20
3.1799	49	3.155	70		
3.0410	100	3.028	60	3.04	100
2.8897	96	2.961	100	2.89	100
2.8356	77	2.820	75		
2.7594	78	2.752	75		
2.3371	47	2.308	10		
2.2218	26	2.258	6	2.235	20
2.1438	82	2.131	45		
1.9250	80	1.915	40		
1.9164	59	1.915	40	1.905	15
1.7994	52	1.794	25		
1.7786	52				
1.7220	60	1.700	30	1.725	20
1.6839	84	1.665	20		
1.6591	68	1.651	30		

hexagonal and monoclinic phases are shown in comparison to observed results in Table 6. The monoclinic values are those obtained from B-type Gd_2O_3, a stable form of Gd_2O_3 because monoclinic Y_2O_3 only exists under high pressure atmospheres. The measured parameters for the high pressure form of monoclinic Y_2O_3 agree reasonably well with those of B-Gd_2O_3 as do the majority of other rare earth oxide monoclinic structures.

The observed d-spacings for the sample match extremely well with respect to both relative intensities and interplanar spacings with those of the hexagonal phase, and many of the monoclinic peaks correspond closely to the observed data as well. To verify the crystal structure, a lower angle scan (2 to 15°) was performed. The monoclinic form of Y_2O_3 exhibits peaks near 6° that do not occur for the hexagonal phase. The results of this scan, which was performed with the lowest available scan rate (0.5°/min) are shown in Figure 35. As can be seen, no crystalline low angle peaks are present and therefore the structure of the bulk was concluded to be hexagonal.

However, electron diffraction patterns obtained from twinned regions and areas exhibiting dislocations yield patterns that can be indexed in the monoclinic system. The diffraction pattern of Figure 36a taken from the twinned region shown in Figure 36b exhibits two superimposed $[\bar{1}30]$ monoclinic patterns. STEM microanalysis across the bands reveals a constant 30 mol percent La_2O_3 concentration (Figure 36c). The monoclinic symmetry as determined by electron diffraction and the composition invariance across the individual strips indicate the strips are actually twin bands which result from the displacive

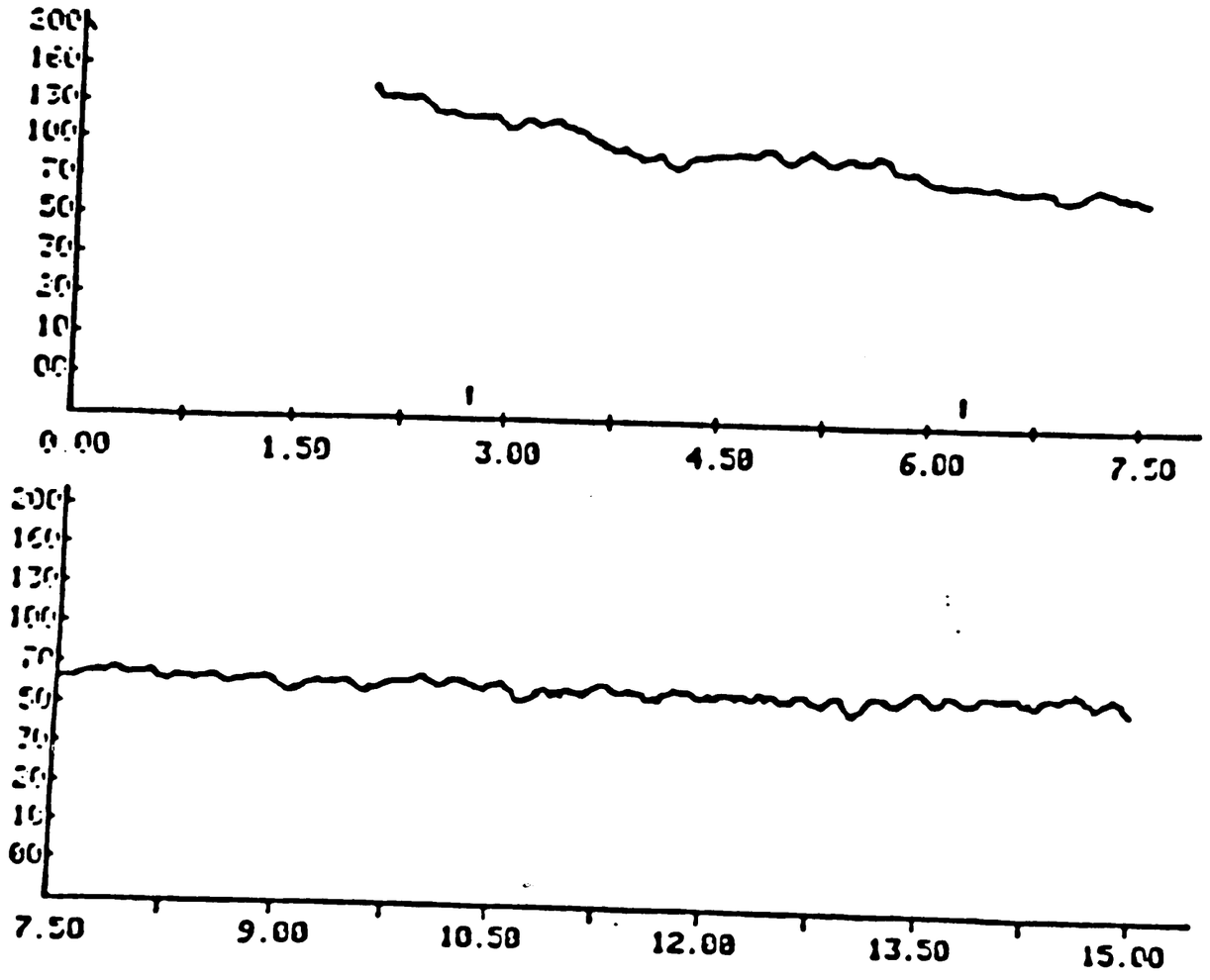

2° TO 15° X-RAY SCAN 30 MOL % La2O3 SAMPLE

2-THETA (DEG)	WIDTH (APPROX)	COUNTS PEAK	COUNTS BKGND	D (ANG)	I (NORM)
2.75	5.00	0.	0.	32.1262	
6.25	2.37	99	0.	14.1412	

2 PEAKS IDENTIFIED 0 CRYSTALLINE 2 AMORPHOUS
2 PEAKS LISTED

Figure 35. Results of x-ray powder diffraction analysis on 30 mol % La_2O_3/Y_2O_3 samples quenches from 2025°C showing no crystalline peaks below 15°C.

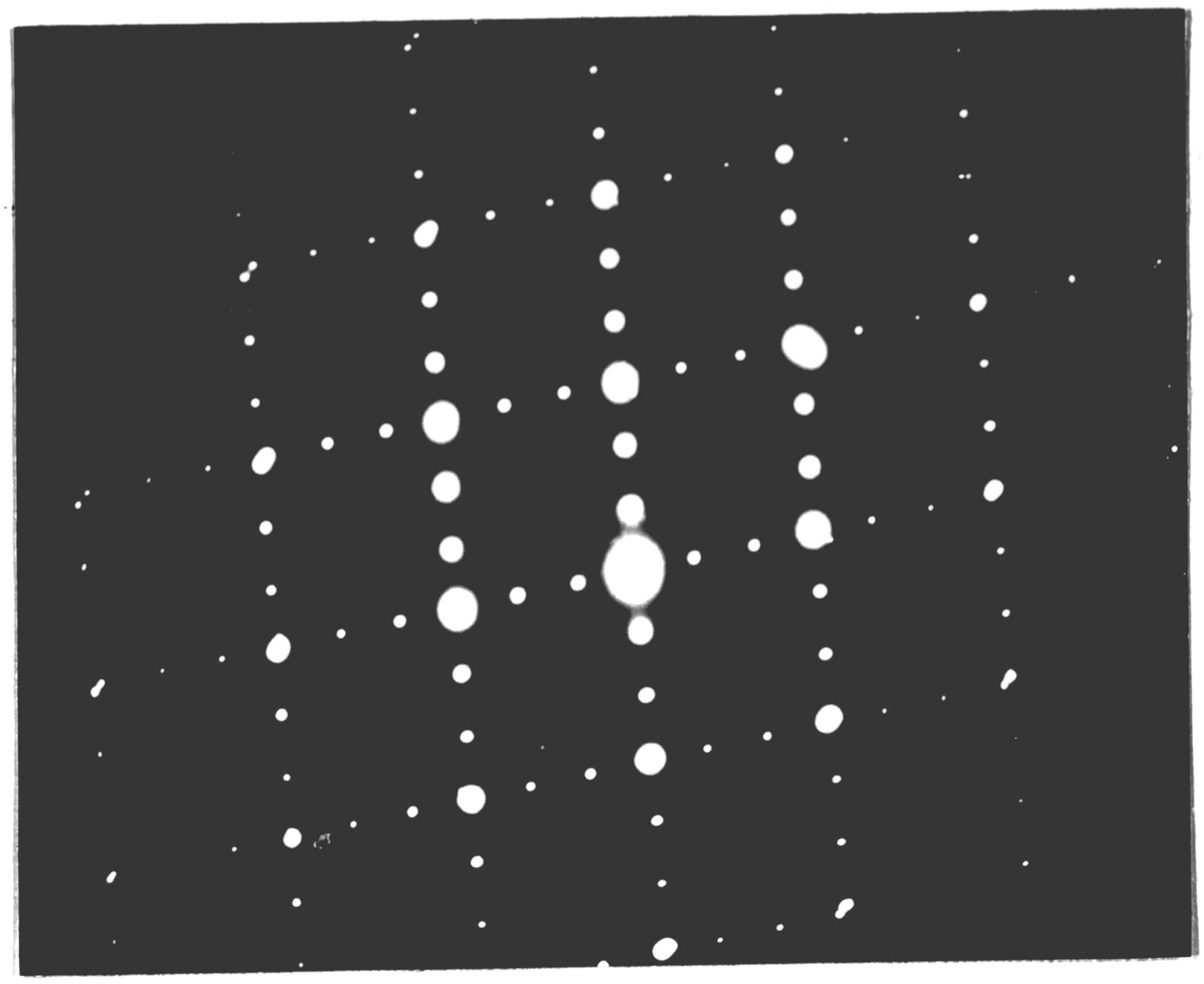

MONOCLINIC

[$\bar{1}$30]

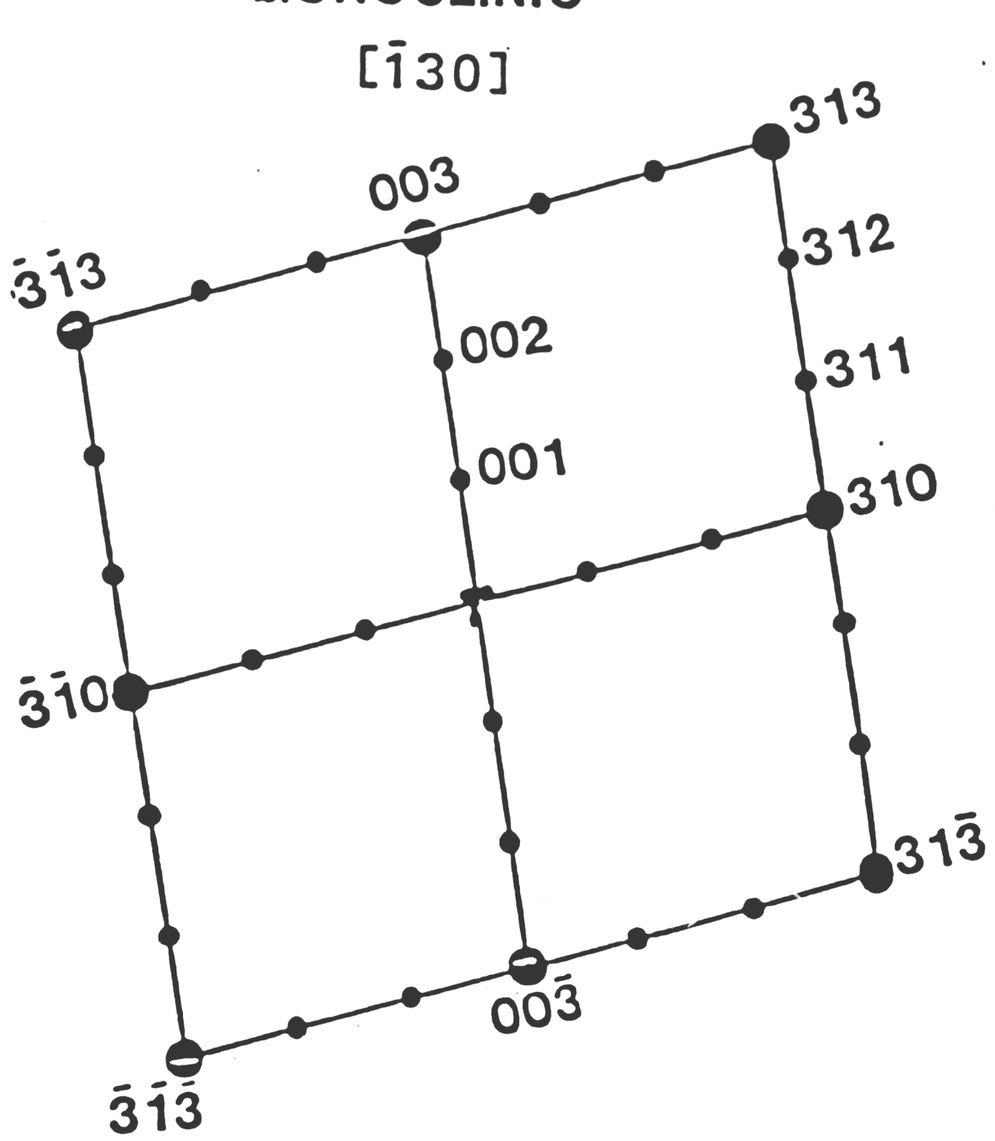

Figure 36a. Selected area diffraction pattern from region shown in 36b, exhibitihg two superimposed [$\bar{1}$30] orientations of the monoclinic phase.

Figure 36b. Bright field micrograph of twinned or banded region obtained in a 30 mol% La_2O_3 sample quenched from the single phase hexagonal phase field.

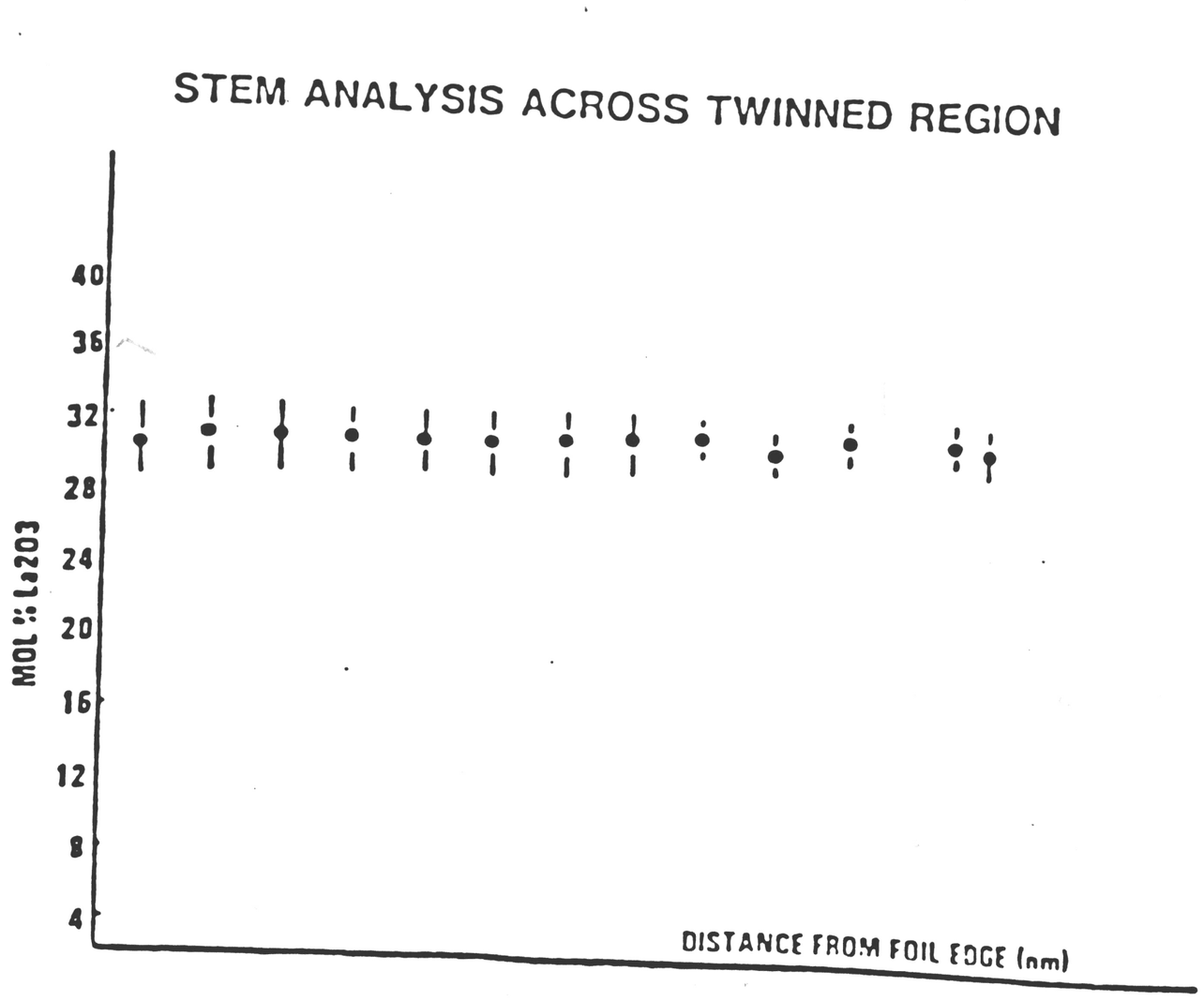

Figure 36c. Microanalysis across banded region of 36b showing compositional invariance.

transformation of this hexagonal phase grain to the monoclinic polymorph.

However, the monoclinic phase has been found to form as alternate bands within the hexagonal matrix and within cubic matrices as well. In situ fast quench TEM studies of Nd_2O_3 by Caro et al.[28] revealed that upon rapidly cooling the hexagonal phase, alternate bands of monoclinic symmetry form within the hexagonal matrix, maintaining a definite epitaxial relationship with the hexagonal phase. Composition invariance was observed between the two phases as well, testifying to the martensitic or displacive transformation of the hexagonal phase to the monoclinic polymorph. GTE reports a banded structure in 16 mol percent La_2O_3 samples which were sintered at 2150°C cooled, and annealed 6 hours at 1950°C. However in this case, the monoclinic strips form within the cubic matrix and differ in composition from their cubic phase counterparts for the structure shown in Figure 37. The observed microstructure of Figure 36b and the monoclinic symmetry testify to the possible displacive nature of the hexagonal to monoclinic phase transition. Center dark field analyses on the high and low intensity spots as well as convergent beam electron diffraction on the individual bands could verify the possibility of two phase coexistence.

Figure 38a exhibits another region of the same sample containing a dislocation network from which the [001] monoclinic selected area diffraction pattern of Figure 38b was obtained. The dark field micrograph shown, taken with the aperture around the (600) reflection clearly show the dislocations (Figure 38c). Although the entire

Figure 37. Banded structure obtained in 16 mol % La_2O_3/ Y_2O_3 samples studied by GTE Laboratories.

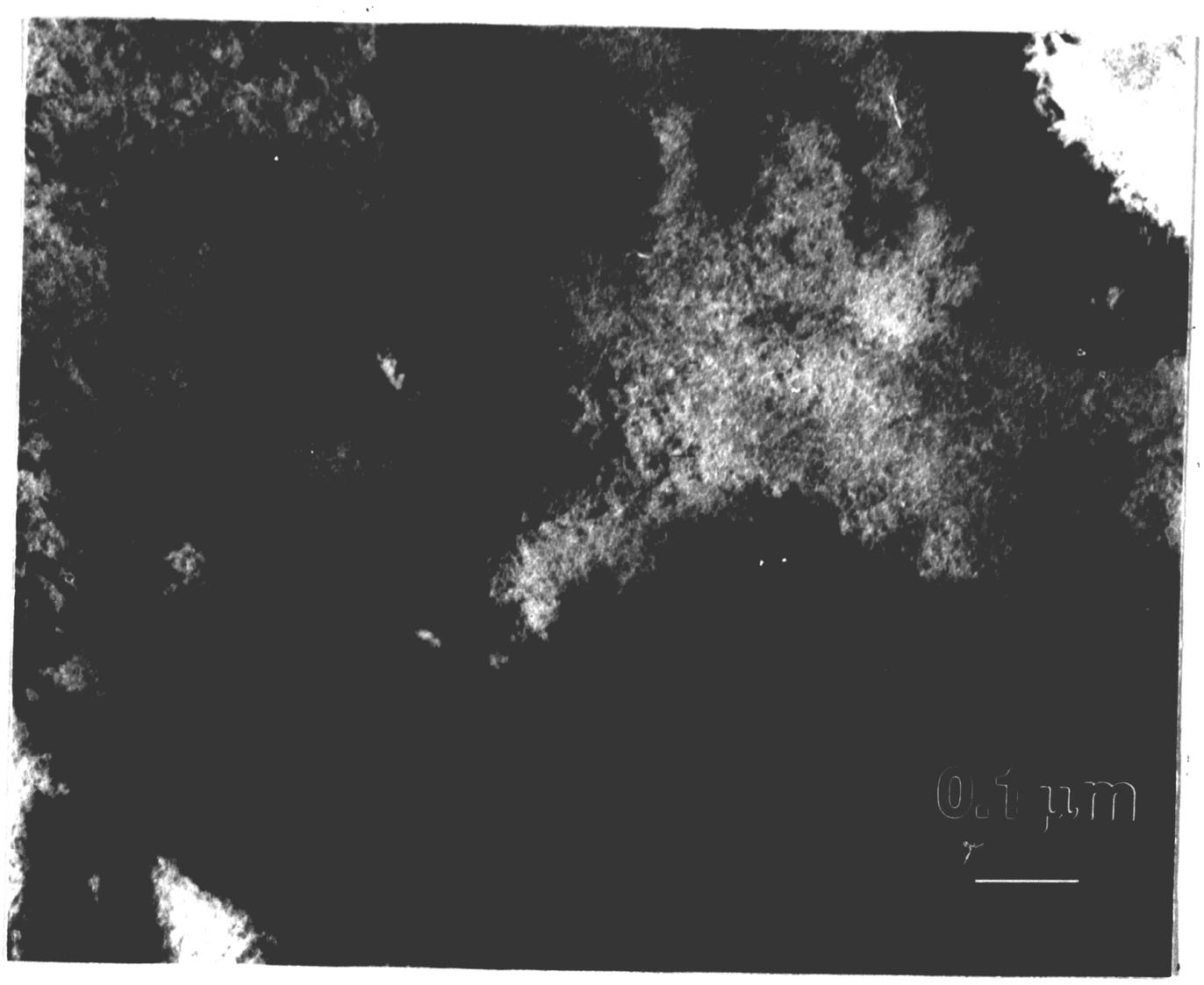

Figure 38a. Bright field micrograph of region of 30 mol% La_2O_3 sample quenched from 2025°C showing dislocations.

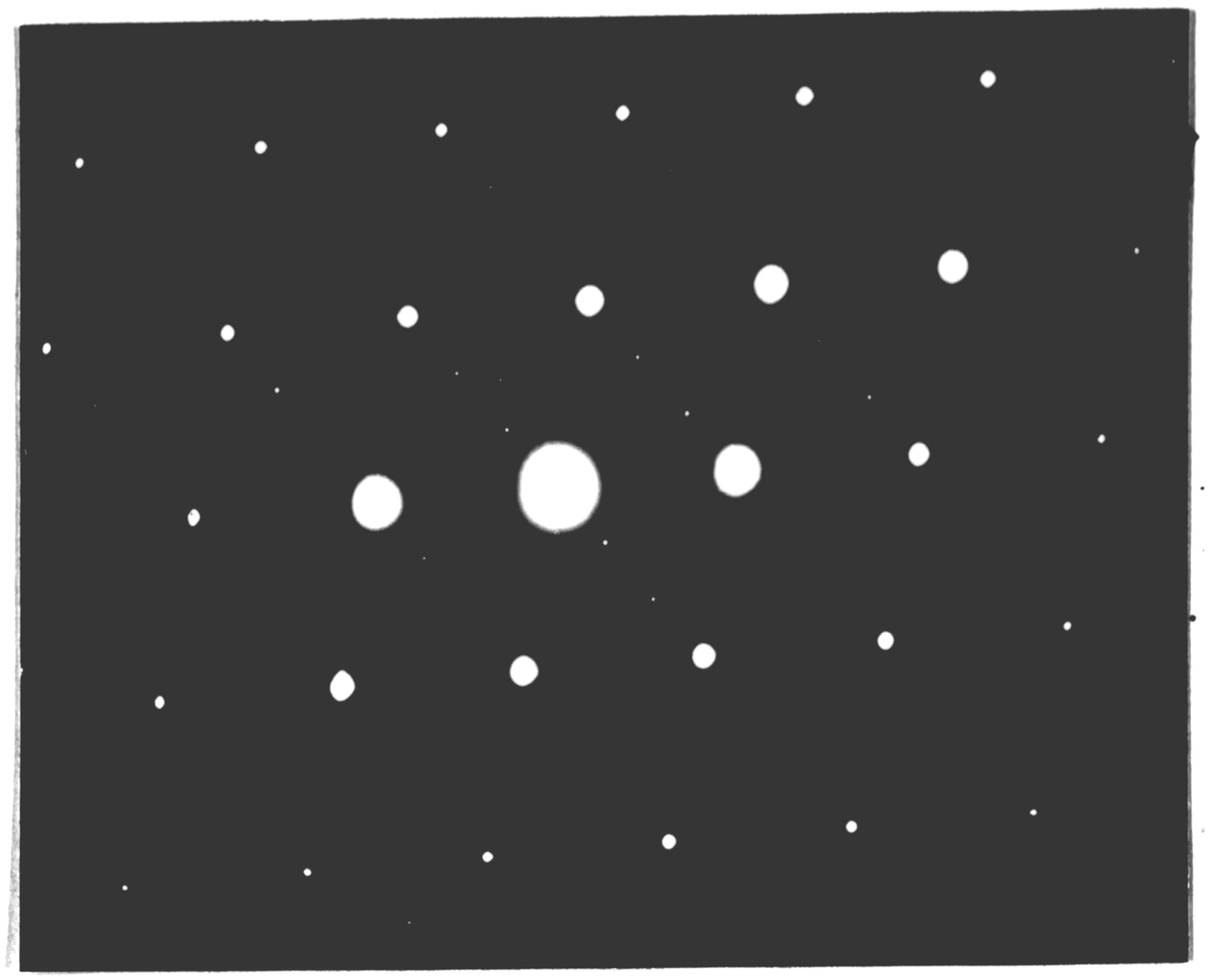

MONOCLINIC
[001]

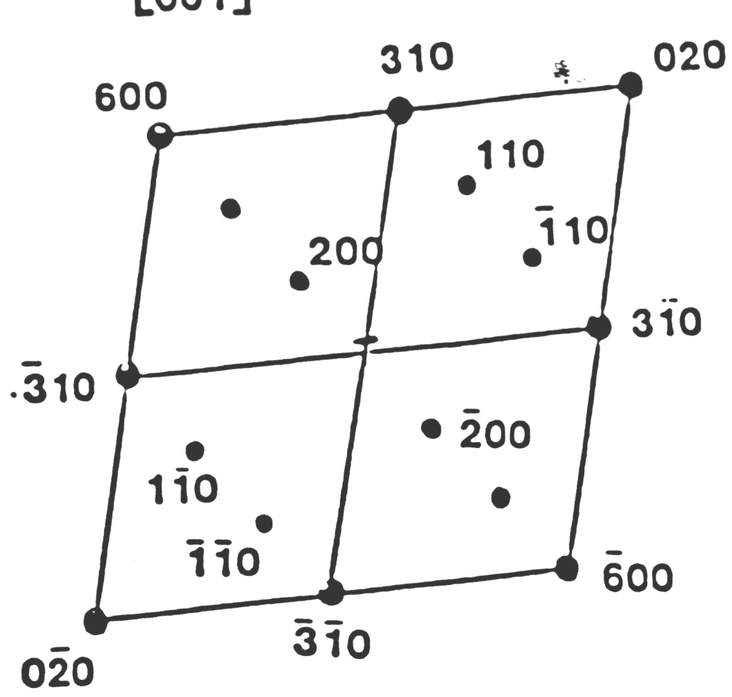

HEXAGONAL
[121]

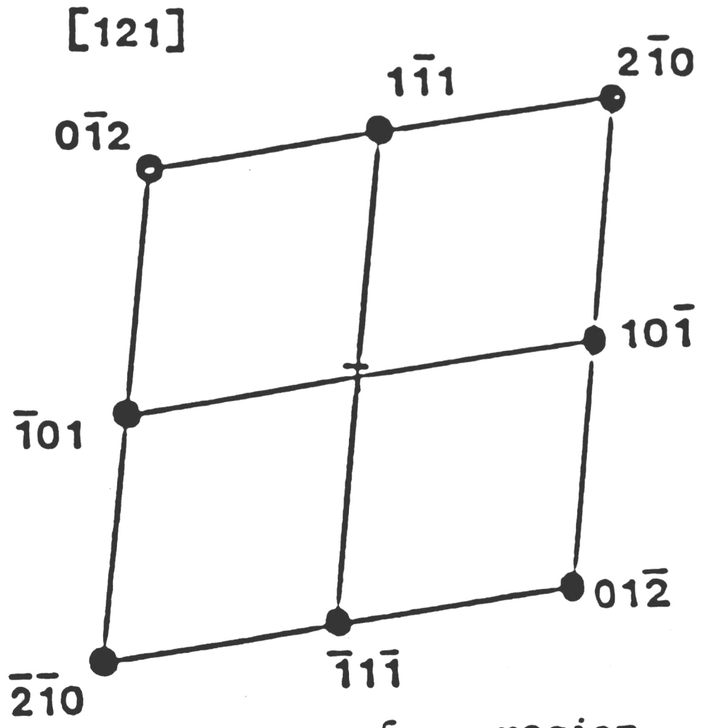

Figure 38b. Selected area diffraction pattern from region of 30 mol% La_2O_3 sample shown in 38a. Entire pattern can be indexed as [001] monoclinic. The high intensity reflections conform to the hexagonal system as well.

Figure 38c. Center dark field micrograph taken with the (600) monoclinic reflection showing the dislocation network.

pattern indexes as [001] monoclinic, the high intensity spots in the pattern can also be indexed as a [121] zone of the hexagonal system. To verify the correctness of the zone axis determinations, convergent beam electron diffraction was employed. Figure 39 shows a Kossel pattern from the region of 38a. Comparison of higher order Laue zone (HOLZ) spacings (H) as determined by measurement of HOLZ ring radii in Kossel patterns with calculated values of the reciprocal lattice layer spacings along the zone axis direction in the crystal determine the correctness of the indexed pattern. For a particular zone axis in a particular crystal system, the two values should agree or differ by an integral multiple as a result of systematic absences in the crystal structure.[64] Results of this analysis (Table 7) yielded the following:

$$H_{monoclinic}\ [001] = 0.1142$$

$$H_{hexagonal}\ [121] = 0.1114$$

$$H_{measured} = 0.1043$$

Thus, the same ambiguities arise in the indexing of the diffraction patterns possibly as a direct result of the similarity between the two crystal systems. As the monoclinic form can be derived from the hexagonal structure by slight deformations of the tetrahedral layered structure in a displacive manner, it may be expected that certain crystallographic directions within the two systems are very similar as to yield such ambiguities. The hexagonal system cannot account for the lower intensity spots while the monoclinic system can account for all. Either the systematic variation in spot intensity occurs due to a structure factor effect for the monoclinic system, or the high

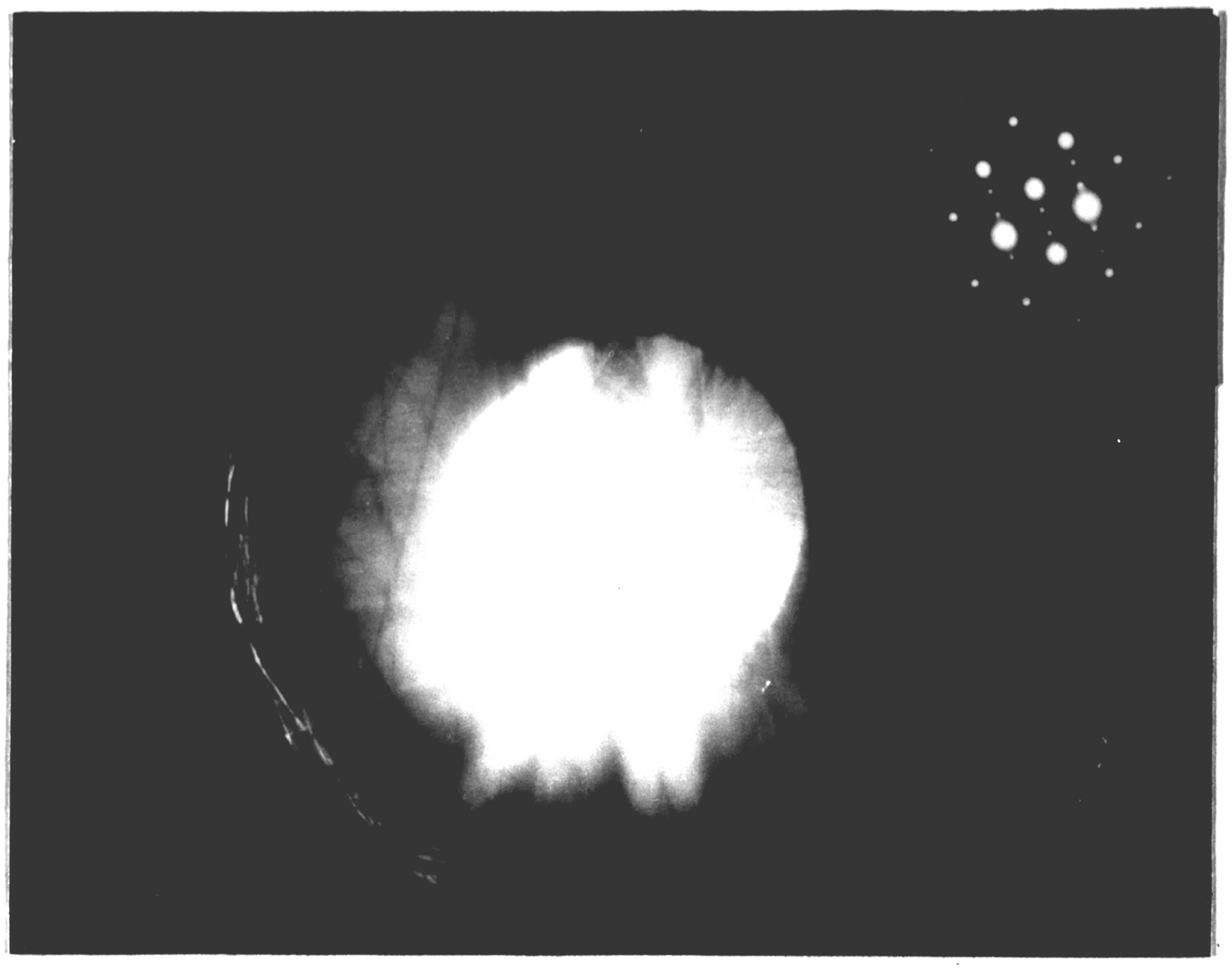

Table 7 - Comparison of Reciprocal Lattice Layer Spacing H:

$H_{monoclinic}$ [001]	=	0.1142
$H_{hexagonal}$ [121]	=	0.1114
$H_{measure}$	=	0.1043

Figure 39. Convergent beam electron diffraction Kossel pattern obtained from the region shown in 38a and used to verify zone axis determined in the diffraction pattern of Figure 38b.

intensity reflections are actually superimposed hexagonal and monoclinic reflections. Center dark field analysis on the low intensity reflections is required to verify this possible two phase existence. Since the d-spacings of the polymorphs in the rare earth oxides are somewhat of a large magnitude for these zone axes, there is a possibility that the presence of the lower intensity spots in the hexagonal structure may arise from the extension of FOLZ reciprocal lattice points into the ZOLZ due to the thinness of the crystal. However, calculations and foil thickness experimentation are necessary to prove this.

Raman Spectroscopy Analysis of Pure Y_2O_3 Sample

Figure 40 shows two Raman spectra obtained from a pressed pellet of cubic Y_2O_3 powder. Intensity is plotted on the ordinate and frequency on the abscissa. The first spectrum was obtained with the green light of an Argon ion laser (wavelength=514.5 nm) while the second was obtained with the blue light of an Argon ion laser (wavelength=488 nm). The peaks which are labeled designate the peaks which are common to both spectra and the strong lines near 380-390 cm^{-1} characterize the cubic polymorphs of Y_2O_3. The remaining lines not common to both spectra can arise from either of two phenomena:

1) differences in sample orientation with respect to the beam which has been demonstrated to give rise to polarization effects as peaks appear for some sample orientations rather than others, or

2) fluorescence phenomena, which depends on the source excitation frequency.

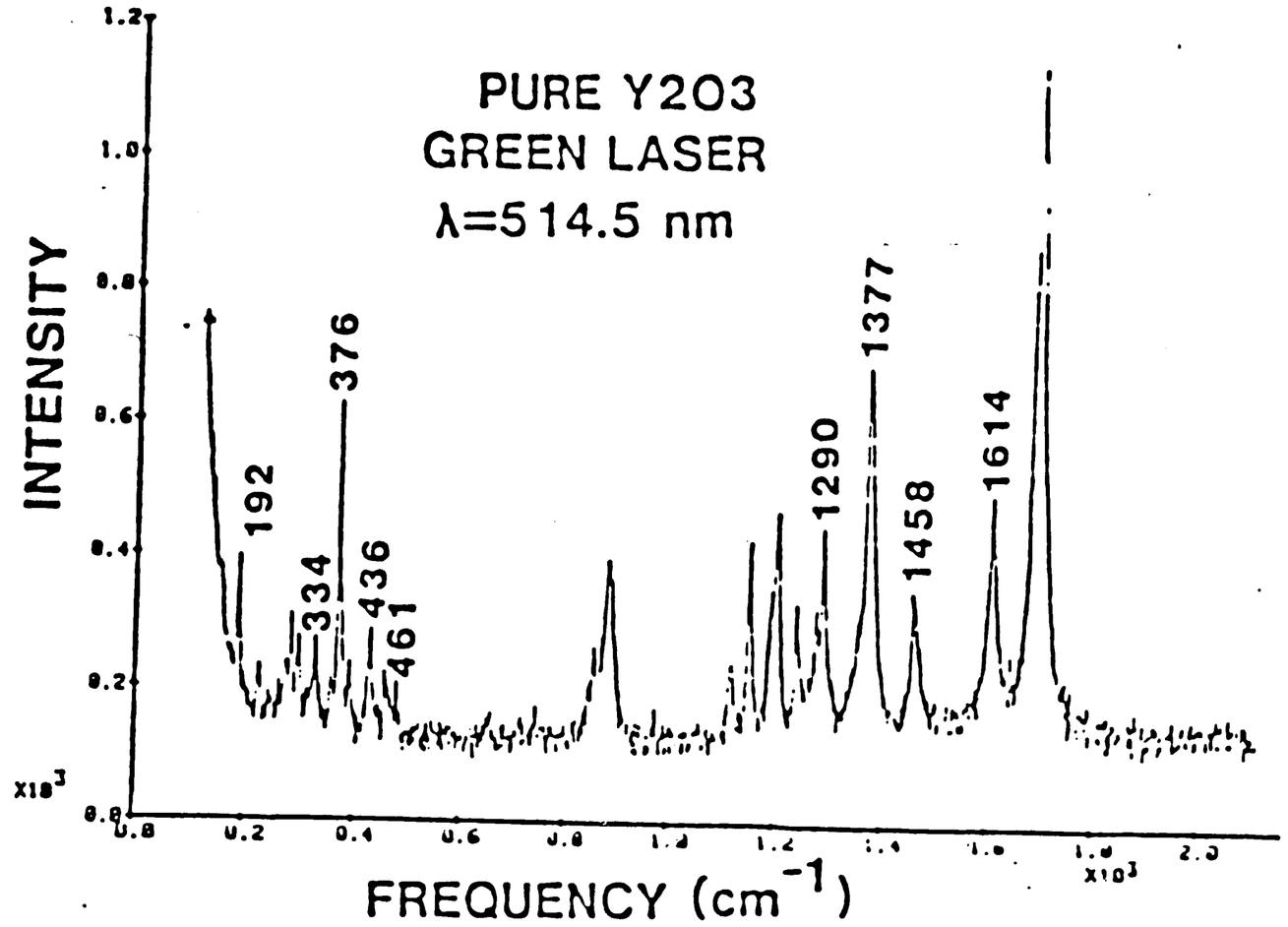

Figure 40. Raman spectra of the cubic polymorph of Y_2O_3 for two different laser excitations.

White and Keramidas[65] report that sharp line fluorescence presents a problem in analyzing rare earth oxides by the Raman technique. For the green laser, fluorescence peaks arise in the range of wave numbers of interest for the polymorphs of the rare earth oxides ($\sim$1000 cm^{-1} or less) and can be reduced or eliminated from this range by switching to the blue laser. Results show that some peaks are common to both at wave numbers near 1200 and above. However, these may still be a result of fluorescence since these numbers approach the high energy region where electronic transitions become more common.

CONCLUSIONS

1. Based on the limited investigations performed in this work on powder preparation by the oxalate co-precipitation technique, no major effects of precipitating temperature on compactibility and sinterability of the final mixed La_2O_3/Y_2O_3 constituents was evident for powders precipitated at 14°C, 25°C, and 70°C and calcined at 1000°C. Any benefits derived from low precipitating temperatures in regards to high surface area powders conducive for sinterability may be lost due to coarsening effects which may occur during the high temperature (1000°C) calcination. Similarly, low surface area oxalate precipitates usually obtained at high precipitating temperatures can break down during calcinations as a result of CO_2 cracking thereby raising the surface area of the calcined powder.

2. Measurement of the k-factor on the Philips 400T for the Y_2O_3/La_2O_3 system using the L-lines of yttrium and lanthanum yielded a value of k=0.54±2%.

3. Silicon contamination from silicon based pump oils deposited during the time the thin foil sits idly in the thinner after the beams shut off has detrimental effects for chemical microanalyses utilizing the yttrium L-line. The partial overlap of the Si^K peak with the Y^L peak and the large mass absorption coefficient of silicon for yttrium L x-rays (∿3200) causes silicon artifacts in the EDS spectrum, poor background fits, absorption of yttrium x-rays, and grossly erroneous intensity data. The problem can be overcome by ion beam cleaning the specimen prior to immediate removal from the thinner and/or by using another family of yttrium x-ray lines away from the Si^K peak and for

which the mass absorption coefficient of silicon is not as critical (Y^K, $\frac{\mu}{\rho}^K_{Si}$ = 11).

4. Nine mol percent La_2O_3/Y_2O_3 samples annealed for various amounts of time at 2100°C just inside the cubic/cubic and hexagonal solvus of the two phase field and quenched exhibit predominantly grain boundary precipitation. Small second phase precipitates approximately 1 μm in size form on the grain boundary within the first 10 minutes while for annealing times of 30 minutes and longer, the microstructure is characterized by grain boundary phases believed to be of monoclinic symmetry, containing a substructure of twins, and possessing an overall strained, facetted appearance. The facetted appearance of these second phases may be a direct result of the displacive nature of the hexagonal to monoclinic transformation as various orientations of monoclinic domains arise due to the deformation of the hexagonal cell.

The 2200°C series exhibits both intergranular and intragranular precipitation, showing small second phase dispersions on dislocations after 1 minute and long, lathlike precipitates for long time anneals (300 minutes). Other types of morphologies were noted on occasion especially for samples annealed 30 minutes or less at either temperature, however, further investigation is required to determine if these are actually a second type of precipitate or just a consequence of the coarsening phenomena after 30 minutes at temperature.

5. Chemical microanalysis on the two samples annealed at 2100°C and at 2200°C for 300 minutes revealed equilibrium matrix concentrations with second phase concentrations far in excess of that predicted by the cubic/cubic and hexagonal solvus boundary of the

phase diagram. Microprobe analyses on the bulk samples confirm STEM results for the matrix and do show regions of second phase where the La_2O_3 concentration exceeds phase diagram predictions even though the resolution capabilities of the instrument exceed typical sizes of the second phase. Either the location of the cubic/cubic and hexagonal solvus boundary is in error or the strained condition of the second phase as a result of coherency may be causing the concentration anomalies due to the precipitate being in a state of coherent equilibrium.

6. X-ray powder diffraction analysis of 30 mol% La_2O_3 samples quenched from the single phase hexagonal field show retention of the hexagonal phase, however, selected area diffraction patterns obtained from compositionally invariant twinned areas and areas showing dislocation networks reveal patterns of monoclinic symmetry. The banded structures may be twins resulting from the hexagonal to monoclinic transition or perhaps a mixture of both phases where the monoclinic bands form epitaxially in the hexagonal phase in a displacive manner. Present results do indicate that the monoclinic phase obtains from the hexagonal polymorph by a diffusionless mechanism involving twinning and slip.

REFERENCES

1. Rhodes, W. H., Trickett, E. A. and Wei, G. C., "Processing Studies for Optically Transparent La_2O_3 Doped Y_2O_3," Annual Report prepared for the Office of Naval Research, July 1980.

2. Ibid, July 1984.

3. Greskovich, C. and Chernoch, I. P., "Polycrystalline Ceramic Lasers," Journal of Applied Physics, Volume 44, No. 10, 1973, p. 4599.

4. Wickersheim, K. A. and Lefever, R. A., "Infrared Transmittance of Crystalline Yttrium Oxide and Related Compounds," Journal of the Optical Society of America, Volume 51, No. 10, 1961, p. 1147.

5. Rhodes, W. H., "Controlled Transient Solid Second Phase Sintering of Y_2O_3," Journal of the American Ceramic Society, Volume 64, No. 1, January 1981, p. 13.

6. Jorgensen, P. J. and Anderson, R. C., "Grain Boundary Segregation and Final Stage Sintering of Y_2O_3," Journal of the American Ceramic Society, Volume 50, No. 11, 1967, p. 553.

7. Ruhle, M. and Heuer, A. H., "Phase Transformations in ZrO_2 Containing Ceramics II: The Martensitic Reaction in Tetragonal ZrO_2," Volume 11 of Advances in Ceramics, 1984.

8. Bansal, G. K. and Heuer, A. H., "On a Martensitic Phase Transformation in Zirconia (ZrO_2)-I: Metallographic Evidence," Acta Metallurgical, Volume 20, 1972, p. 1281.

9. Bansal, G. K. and Heuer, A. H., "On a Martensitic Phase Transformation in Zirconia (ZrO_2)-II. Crystallographic Aspects," Acta Metallurgical, Volume 22, 1974, p. 409.

10. Kriven, W. M., Fraser, W. L. and Kennedy, S. W., "The Martensitic Crystallography of Tetragonal ZrO_2," Advances in Ceramics, Volume 3, publ. American Ceramic Socity, 1981, p. 82.

11. Garvie, R. C., Hannink, R. H., and Pascoe, R. T., "Ceramic Steel," Nature, Volume 258, 1975, p. 703.

12. Stevens, R., An Introduction to ZrO_2, published by Magnesium Elektron Ltd., June 1983.

13. Mizuno, M., Rouanet, A., Yamada, T. and Noguchi, T., "Phase Diagram of the System La_2O_3-Y_2O_3 at High Temperatures," Yogyo Kyokai Shi, Volume 84, #7, 1976, p. 342.

14. Coutoures, J. and Foex, M., "High Temperature Equilibria in the System La_2O_3-Y_2O_3," Journal of Solid State Chemistry, Volume 11, No. 4, 1974, p. 294.

15. Zachariasen, W., "The Crystal Structure of the Modification C of the Sesquioxides of the Rare Earth Metals and of Indium and Thallium," Norsk Tidsskrift Geologisk, Volume 9, 1926, p. 310.

16. Paton, M. G. and Maslen, E. N., "A Refinement of the Crystal Structure of Yttria," Acta Crystallographica, Volume 19, 1965, p. 307.

17. Caro, P. E., "OM_4 Tetrhedra Linkages and the Cationic Group $(MO)_n^{n+}$ in Rare Earth Oxides and Oxysalts," Journal of the Less Common Metals, Volume 16, 1968, p. 367.

18. Schaack, G. and Koningstein, J. A., "Phonon and Electronic Raman Spectra of Cubic Rare Earth Oxides and Isomorphous Yttrium Oxide," Journal of the Optical Society of America, Volume 60, No. 8, 1970, p. 1110.

19. Mehrota, P. N., Chandrasekhar, G. V., Rao, C. N. R. and Subbarao, E. C., "Phase Transformations of Rare Earth Sesquioxides La_2O_3, Nd_2O_3, Pr_2O_3, Y_2O_3," Transactions of the Faraday Society, Volume 62, 1966, p. 3586.

20. Hoekstra, H. R., "Phase Relationships in the Rare Earth Sesquioxides at High Pressure," Inorganic Chemistry, Volume 5, 1966, p. 754.

21. Gouteron, J., Michel, D., Le Jus, A. M. and Zarembowitch, J., "Raman Spectra of Lanthanide Sesquioxide Single Crystals: Correlation Between A and B Type Structures," Journal of Solid State Chemistry, Volume 38, 1981, p. 288.

22. Roth, R. S. and Schneider, S. J., "Phase Equilibria in Systems Involving the Rare Earth Oxides I. Polymorphism of the Oxides of the Trivalent Rare Earth Ions," Journal of Research of the National Bureau of Standards, Volume 64A, 1960, p. 309.

23. Guentert, O. J. and Mozzi, R. L., "The Monoclinic Modification of Gadolinium Sesquioxide Gd_2O_3," Acta Crystallographica, Volume 11, 1958, p. 746.

24. Boulesteix, P. C., Caro, P., Gasgnier, M. LaBlanchetais, Ch. H. and Schiffmacher, G., "Microscope et Diffraction Electroniques de Couches Minces de Sesquioxides de Neodyme la Transformation de Caractere Martensitique Phase Monoclinque--Phase Hexagonale," Acta Crystallographica A, Volume 27, 1971, p. 552.

25. Boulesteix, P. C., Pardo, B., Caro, P., Gasgnier, M., LaBlanchetais, Ch. H., "Etude de Couches Minces de Sesquioxides

de Samarium Type B par Microscope et Diffraction Electroniques," Acta Crystallographica B, Volume 27, 1971, p. 216.

26. Boulesteix, P. C., Caro, P., Gasgnier, M., LaBlanchetais, Ch. H. and Schittmacher, G., "Thin Films of Praseodymium Sesquioxide: Martensitic Character of the Monoclinic to Hexagonal Phase Transformations," Physics Letters, Volume 34A, No. 7, 1971, p. 437.

27. Salem, M. B., Dorbez, R. and Yangui, B., "Ferroelastic Character and Study by HREM of the Mechanism of the Hexagonal-Monoclinic Phase Transition of Rare Earth Sesquioxides," Philiosophical Magazine A, Volume 50, No. 5, 1984, p. 621.

28. Caro, P. E., Schiffmacher, G., Boulesteix, C. Loier, Ch., and Portier, R., "Defects and Impurities Influences on Phase Transformations in Rare Earth Oxides," Defects and Transport in Oxides, ed. S. Seltzer and R. I. Jaffee, Plenum Press, 1974, p. 519.

29. Boulesteix, C., Pardo, B., Valiergue, L., Caro, P., Gasgnier, M., and LaBlanchetais, Ch. H., "Reported Twinning and Dislocations in Gadolinium Metal Thin Films Identified as Occurring in B-type Gadolinium Sesquioxide Crystals," Physics Letters, Volume 32A, No. 5, 1970, p. 361.

30. Boulesteix, C. and Yangui, B., "Domains et Interfaces Engendree's all cours d'une Transformation Cristallographique Cooperative--Application au cas de la Transformation Hexagonale Monoclinique des Sesquioxides de Terres Rares I. De'numbrement

et Position Relative des Domaines Equivalents," Physical Status Solidi A, Volume 70, 1982, p. 597.

31. Boulesteix, C. and Yangui, B., "Domains et Interfaces Engendree's all cours d'une Transformation Cristallographique Cooperative--Application au cas de la Transformation Hexagonale Monoclinique des Sesquioxides de Terres Rares II. Position Relative et Raccordement des Variantes de Domaines de Rotation et de Translation: Raccordement en e'toile," Physical Status Solidi A, Volume 73, 1982, p. 515.

32. Cohen, M., Olson, G. B. and Clapp, P. C., "On the Classification of Displacive Phase Transformations," Proceedings of the International Conference on Martensitic Transformation, ICOMAT, 1979.

33. Evans, A. G., and Heuer, A. H., "Review--Transformation Toughening in Ceramics: Martensitic Transformations in Crack Tip Stress Fields," Journal of the American Ceramic Society, Volume 63, No. 5-6, 1980, p. 241.

34. Kaufman, L. and Cohen, M., "Thermodynamics and Kinetics of Martensitic Transformations," Chapter 3 in Progress in Metal Physics, Volume 7, ed. B. Chalmers and R. King, Pergamon Press, Inc., 1958, p. 165.

35. Subbarao, E. C., Maiti, A. S. and Srivastava, K. K., "Martensitic Transformations in Zirconia," Physical Status Solidi A, Volume 21, 1974, p. 9.

36. Rigterink, M. D., "The Chemical Preparation of Raw Materials for Electronic Ceramics," Canadian Ceramic Society Journal, Volume 37, 1968, p. 56.

37. O'Bryan, H. M., Gallagher, P. K., Monforte, F. R., and Schrey, F., "Microstructure Control in Nickel Ferrous Ferrite," Ceramic Bulletin, Volume 48, No. 2, 1969, p. 203.

38. Dragoo, A. L. and Domingues, L. P., "Preparation of High Density Ceria-Yttria Ceramics," Journal of the American Ceramic Society, Volume 65, No. 5, 1982, p. 253.

39. Reetz, T., Richter, W., Irmisch, R. and Lang, H. J., "Enfluss des Pulverherstellungsprozesses auf die Eigenschaften von ThO_2-Y_2O_3 Mischoxidkeramik," Kernenergie; Zeitschrift fur Kernforschung und Kerntechnik, Volume 24, No. 1, 1980, p. 17.

40. Overs, A. and Riess, I., "Properties of the Solid Electrolyte Gd_2O_3 Doped CeO_2 Prepared by Thermal Decomposition of Mixed Cerium-Gadolinium Oxalate," Journal of the American Ceramic Society, Volume 65, No. 12, December 1982, p. 606.

41. Subbarao, E. C., Sutter, P. H. and Hrizo, J., "Defect Structure and Electrical Conductivity of ThO_2-Y_2O_3 Solid Solutions," Journal of the American Ceramic Society, Volume 48, No. 9, 1965, p. 443.

42. Greskovich, C. and Woods, K. N., "Fabrication of Transparent ThO_2 Doped Y_2O_3," Journal of the American Ceramic Society, Volume 52, No. 5, 1973, p. 473.

43. Goldstein, J. I., Costley, J. L., Lorimer, G. W. and Reed, S. J. B., "Quantitative X-ray Analysis in the Electron Microscope," Scanning Electron Microscopy, I, 1977, p. 315.

44. Williams, D. B., "Quantitative X-ray Microanalysis in the Analytical Electron Microscope," Chapter 4 in Practical Analytical Electron Microscopy in Materials Science, Philips Electronics Publishers, Mahwah, NJ, 1984.

45. Bender, B. A., Williams, D. B. and Notis, M. R., "Absorption Effects in STEM Microanalysis of Ceramic Oxides," Journal of the American Ceramic Society, Volume 63, No. 3-4, 1980, p. 149.

46. Heinrich, K. F. J., The Electron Microprobe, ed. T. D. McKinley, K. F. J. Heinrich, and D. B. Wittry, published by J. Wiley, New York, 1966, p. 296.

47. Clarke, D. R. and Adar, F., "Raman Microprobe Spectroscopy of Polyphase Ceramics,"

48. Phillippi, C. M. and Mazdiyazni, K. S., "Infrared and Raman Spectra of ZrO_2 Polymorphs," Journal of the American Ceramic Society, Volume 54, No. 5, 1971, p. 254.

49. Keramidas, V. G., and White, W. B., "Raman Scattering Study of the Crystalline and Phase Transformations of ZrO_2," Journal of the American Ceramic Society, Volume 57, No. 1, 1973, p. 22.

50. Clarke, D. R. and Adar, F., "Measurement of the Crystallographically Transformed Zone Produced by Fracture in Ceramics Containing Tetragonal Zirconia," Journal of the American Ceramic Socity, Volume 65, No. 6, 1982, p. 284.

51. Etz, E. S., "Raman Microprobe Analysis: Principles and Applications," in Scanning Electron Microscopy, 1979, p. 67.

52. Irish, D. E. and Chen, H., "The Application of Raman Spectroscopy to Chemical Analysis," Applied Spectroscopy, Volume 25, No. 1, 1971, p. 1.

53. Walsh, P. N., Goldstein, A. W., and White, D., "Vaporiztion of Rare Earth Oxides," Journal of the American Ceramic Society, Volume 43, No. 5, 1960, p. 229,

54. Ackermann, R. J., Raub, E. G. and Walter, R. R., "Thermodynamic Study of the System Yttrium and Yttrium Sesquioxide: A Refinement of the Vapor Pressure of Yttrium," Journal of Chemical Thermodynamics, Volume 2, 1979, p. 139.

55. Ackermann, R. J. and Raub, E. G., "The Thermodynamic Properties of Substoichiometric Yttrium Sesquioxides," Journal of Chemical Thermodynamics, Volume 5, 1973, p. 331.

56. Blum, S. L. and Maguire, E. A., "Differential Thermal Analysis of Some Yttrium and Lanthanon Compounds," Ceramic Bulletin, Volume 39, No. 6, 1960, p. 310.

57. Gallagher, P. K., Schrey, F. and DiMarcello, F. V., "Preparation of Semiconducting Titanates by Chemical Methods," Journal of the American Ceramic Society, Volume 46, No. 8, August 1983, p. 359.

58. Wei, G. C., GTE Laboratories, private communication, 1985.

59. Busovne, B. J., Kotchick, D. M. and Tressler, R. E., "Deformation History Effects on the Precipitation Hardening Behavior of Ti^{+4}-Doped Sapphire," Philosophical Magazine A, Volume 39, No. 3, 1979, p. 266.

60. Williams, R. O., "Long Period Superlattices in the Copper Gold System as Two Phase Mixtures," Metallurgical Transactions, Volume 11A, February 1980, p. 247.

61. Cahn, J. W. and Larche, F., "A Simple Model for Coherent Equilibrium," Acta Metallurgica, Volume 32A, No. 11, 1984, p. 1915.

62. Cahn, J. W. and Larche, F., "Effects of Coherency Constraints on Phase Equilibrium," Materials Research Society Symposium Proceedings, Volume 19, 1983, Elsevier Science Publishing Co., Inc.

63. Rhodes, W. H., private communication, 1985.

64. Raghavan, M. Scanlon, J. C. and Steeds, S. J. B., "Use of Reciprocal Lattice Layer Spacing in Convergent Beam Electron Diffraction Analysis," Metallurgical Transactions, Volume 15A, No. 7, July 1984, p. 1299.

65. White, W. B. and Keramidas, V. G., "Vibrational Spectra of Oxides of the C-type Rare Earth Oxide Structure," Spectrochimica Acta, Volume 28A, kp. 501.

APPENDIX I

Sintered Density Determination by Archimedes Principle

The Archimedes method involves analyses of the relative weights of the sample when measured in air and when immersed in a liquid medium. A portion of the sample is weighed suspended in air to obtain a value for the suspended weight of sample and wire in air (W_A). The sample is submerged in a liquid medium and pumped in a vacuum to remove all air from within the sample and impregnate it with the liquid medium. It is then weighed suspended in the medium to determine the weight of both suspended wire and sample in the liquid (W_L). Finally, the moist weight of the impregnated specimen measured unsuspended (W_M) is obtained. The density is then calculated by the equation.

$$\text{density } (\rho) = \frac{\text{constant } (W_M - W_W)}{(W_L - W_W) - (W_A - W_W)}$$

where W_W represents the wire weight, the constant the density of the liquid medium (0.8669 g/cc for toulene used in this work) and the other terms are defined above.

APPENDIX II

Critical Thickness Determinations for Absorption of X-rays by the Thin Foil

For the Y_2O_3-La_2O_3 system, absorption of the yttrium L and the lanthanum L x-rays by yttrium, lanthanum and oxygen must be considered. The correction factor to the intensity ratios in the Cliff-Lorimer equation exp(-D), is a function of specimen density (ρ), thickness (t), x-ray take-off angle (α) and the mass absorption coefficients of the specimen for each of the elements of interest ($\mu/\rho^{Y \text{ or } La}_{specimen}$ i.e.

$$D = [(\rho t/2)((\frac{\mu}{\rho})^{La}_{specimen} - \frac{\mu}{\rho}|^{Y}_{specimen})\csc\alpha] \qquad (a)$$

The thin film criterion breaks down for $D>0.1$. $_{Y}^{L}$ The mass absorption coefficient of the specimen for Y^L x-rays $\frac{\mu}{\rho}|^{}_{specimen}$ is determined as follows:

$$\frac{\mu}{\rho}|^{Y}_{specimen} = \frac{\mu}{\rho}|^{Y^L}_{Y} C_Y + \frac{\mu}{\rho}|^{Y^L}_{La} C_{La} + \frac{\mu}{\rho}|^{Y^L}_{o} Co \qquad (b)$$

where $\frac{\mu}{\rho}|^{Y^L}_{Y}$, $\frac{\mu}{\rho}|^{Y^L}_{La}$, $\frac{\mu}{\rho}|^{Y^L}_{o}$ represent the mass absorption coefficients for Y^L x-rays by yttrium, lanthanum and oxygen, respectively and C_Y, C_{La}, C_o represent the weight fractions of the respective absorbers. A similar analysis can be done for the La^L x-rays.

Knowing the x-ray take-off angle (20-22° for the Philips 400T) and the specimen density (5.21 g/cc for 9 mol% La_2O_3/Y_2O_3) and setting D=0.1, the critical foil thickness beyond which absorption corrections

become necessary can be obtained from equation (a) above. For 9 mol% La_2O_3/Y_2O_3 samples, this becomes $t=2.1\times10^{-5}$ cm or 2100Å.

VITA

Stephen F. Horvath was born on March 9, 1961, to Mr. and Mrs. Stephen and Angela Horvath in Bethlehem, Pennsylvania. After completing his secondary education at Bethlehem Catholic High School, he gained entry to Lehigh University in the fall of 1979 where he received the Harvey M. Burkey trustee scholarship, the John Cyril Osborn Award in Metallurgy and Materials Engineering, and was elected to the Tau Beta Pi National Engineering Honor Society. He graduated with honors in 1983 with a B.S. degree in Metallurgy and Materials Engineering and accepted an IBM Fellowship for graduate study at Lehigh in the field of ceramics. He is a member of the American Society for Metals, the American Ceramic Society, and the Microbeam Analysis Society.